Late Pleistocene to Holocene transtension in the northern Cascadia forearc: Evidence from surface ruptures along the Beaufort Range fault

Emerson M Lynch[1], Christine A. Regalla[1], Kristin Diane Morell[2], Nicolas Harrichhausen[3], and Lucinda Jane Leonard[4]

[1]Northern Arizona University
[2]University of California, Santa Barbara
[3]ISTerre
[4]University of Victoria

June 7, 2023

Abstract

The active deformation field in subduction forearcs provides critical information about the stress and strain state of the upper plate and its potential for seismogenesis. However, these properties are challenging to quantify in most subduction systems, and in the northern Cascadia forearc, few faults have been identified that can be used to reconstruct the upper plate deformation field. Here we investigate the slip history of the Beaufort Range fault (BRF) on Vancouver Island. This fault was proposed to host the 1946 M7.3 Vancouver Island earthquake, but no surface rupture or evidence of Quaternary activity has been documented, and the stress and strain conditions that promoted this event are poorly understood. We provide the first evidence that the BRF is active, using newly-collected lidar to map topographic scarps along the fault system and to reconstruct slip vectors from offset geomorphic markers. Quaternary deposits and landforms that show increasing magnitude of displacement with age provide evidence for at least three M ~6.5-7.5 earthquakes since ~15 ka, with the most recent event occurring <3-4 ka. Kinematic inversions of offset geomorphic markers show that the BRF accommodates right-lateral transtension along a steeply NE-dipping fault. This fault geometry and kinematics are similar to those modeled for the 1946 earthquake, suggesting that the BRF is a candidate source fault for this event. We find that the kinematics of the BRF are consistent over decadal to millennial timescales, suggesting that this portion of the northern Cascadia forearc has accommodated transtension over multiple earthquake cycles.

Late Pleistocene to Holocene transtension in the northern Cascadia forearc: Evidence from surface ruptures along the Beaufort Range fault

Emerson M. Lynch[1,2], Christine Regalla[1], Kristin D. Morell[3], Nicolas Harrichhausen[4], and Lucinda J. Leonard[5]

[1]School of Earth and Sustainability, Northern Arizona University, Flagstaff, AZ, USA
[2]Department of Earth and Environmental Geoscience, Washington and Lee University, Lexington, VA, USA
[3]Department of Earth Science, University of California, Santa Barbara, CA, USA
[4]Univ. Grenoble Alpes, Univ. Savoie Mont Blanc, CNRS, IRD, Univ. Gustave Eiffel, ISTErre, 38000 Grenoble, France
[5]School of Earth and Ocean Sciences, University of Victoria, Victoria, BC, Canada

Key Points:

- Field mapping and surveys confirm multiple Late Pleis. to Holoc. surface ruptures along the Beaufort Range Fault (BRF).
- Kinematic inversions show the BRF has accommodated right-lateral transtension along a steeply NE dipping fault since the Late Pleis.
- BRF geometry and kinematics are similar to 1946 Vancouver Island earthquake mechanism, making it a candidate source fault for that event.

Corresponding author: Emerson M. Lynch, `emerson.lynch@gmail.com`

Abstract

The active deformation field in subduction forearcs provides critical information about the stress and strain state of the upper plate and its potential for seismogenesis. However, these properties are challenging to quantify in most subduction systems, and in the northern Cascadia forearc, few faults have been identified that can be used to reconstruct the upper plate deformation field. Here we investigate the slip history of the Beaufort Range fault (BRF) on Vancouver Island. This fault was proposed to host the 1946 M7.3 Vancouver Island earthquake, but no surface rupture or evidence of Quaternary activity has been documented, and the stress and strain conditions that promoted this event are poorly understood. We provide the first evidence that the BRF is active, using newly-collected lidar to map topographic scarps along the fault system and to reconstruct slip vectors from offset geomorphic markers. Quaternary deposits and landforms that show increasing magnitude of displacement with age provide evidence for at least three M_W ∼6.5-7.5 earthquakes since ∼15 ka, with the most recent event occurring <3-4 ka. Kinematic inversions of offset geomorphic markers show that the BRF accommodates right-lateral transtension along a steeply NE-dipping fault. This fault geometry and kinematics are similar to those modeled for the 1946 earthquake, suggesting that the BRF is a candidate source fault for this event. We find that the kinematics of the BRF are consistent over decadal to millennial timescales, suggesting that this portion of the northern Cascadia forearc has accommodated transtension over multiple earthquake cycles.

Plain Language Summary

Subduction zones, like Cascadia, contain onshore fault networks that can host earthquakes that are dangerous to communities. However in many locations, like Vancouver Island, Canada, we know little about where these faults are and what type and magnitude earthquake they can host (if any). We focus on the Beaufort Range fault (BRF) on Vancouver Island, and show for the first time that the BRF hosted recent earthquakes. Newly-available high-resolution topography data show many scarps, or vertical offsets of the ground surface produced in past earthquakes, along a >40 km zone. Surveys of landforms that have been offset by the BRF show both vertical and horizontal offsets along a near-vertical fault. The nearby 1946 Vancouver Island earthquake had similar vertical and horizontal offsets along a near-vertical fault, suggesting that this earthquake might have happened on the BRF. Our data show there have been >3 large earthquakes on the BRF in the past ∼15,000 years, the most recent $<$3,000-4,000 years ago. The offsets we observe suggest these earthquakes had magnitudes between ∼6.5 and 7.5. Future similar earthquakes could cause shaking damage to many nearby communities, including the cities of Port Alberni and Nanaimo, and nearby hydroelectric facilities.

1 Introduction

Quantifying the stress state and strain history of subduction zone forearcs is critical for understanding the energy budget of convergent margins (e.g., Huang et al., 2022), the seismic potential and hazard of forearc faults (e.g., Wang et al., 1995; Balfour et al., 2011; Thenhaus & Campbell, 2002), and the evolution of the upper plate during the megathrust seismic cycle (e.g., Regalla et al., 2017; Herman & Govers, 2020). However, stress is notoriously difficult to measure or approximate, and in the northern Cascadia forearc of Vancouver Island, there are several competing models for what controls forearc stress and upper plate deformation (e.g., Mazzotti et al., 2011; Finley et al., 2019; Delano et al., 2017). Quantifying upper plate deformation is also limited in Cascadia because the subduction zone is relatively seismically quiet, limiting our ability to infer stress field data from seismicity. Furthermore, the large locking signal on the plate interface inhibits our ability to isolate Global Navigation Satellite System (GNSS) deformation associated with upper plate faults (e.g., Mazzotti et al., 2011; S. Li et al., 2018), and few active upper plate faults have been identified regionally to date (e.g., Morell et al., 2017).

Although the northern Cascadia region exhibits relatively low rates of instrumental seismicity, this region was also host to the largest onshore historic earthquake in Canada, the M 7.3 1946 Vancouver Island earthquake (Rogers & Hasegawa, 1978; Rogers, 1979; Lamontagne et al., 2018). This earthquake is the largest to have occurred anywhere within the Cascadia subduction zone system, including the megathrust, since written historical recordkeeping began (the past ∼200 yrs). However, despite this earthquake's size and moderate damage to nearby population centers (Hodgson, 1946; Mathews, 1979; Clague, 1996), the fault that ruptured during the 1946 earthquake remains unknown. In addition, little is known about the current or past stress state and strain field of the crust surrounding this major historical rupture, what upper plate conditions could lead to future ruptures, and if similar events have occurred in the geologic past. Such data are necessary not only to evaluate the seismic potential of forearc faults, but also to determine their deformation rates, kinematics, and relationship to the regional stress field. Yet, no

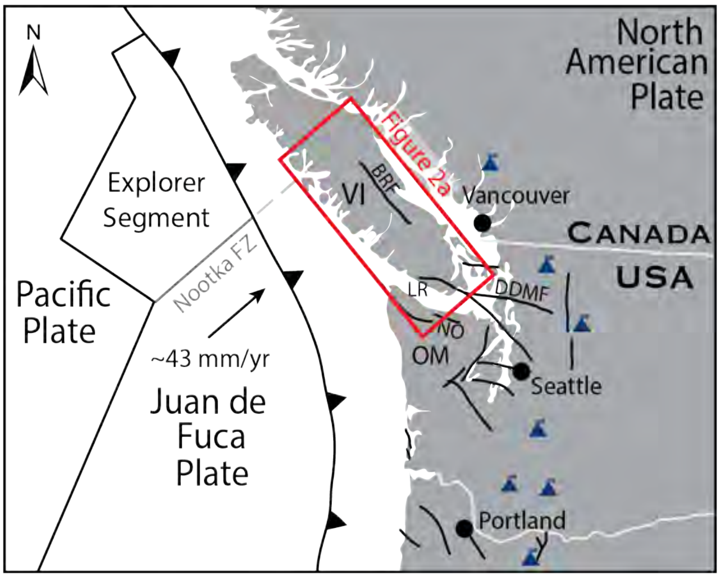

Figure 1. Regional tectonic setting showing the location of the Beaufort Range fault (BRF) and other active faults in the Cascadia forearc of Canada and the USA. Juan de Fuca – North America convergence vector after Kreemer et al. (2014). Slab depth contours from Slab2 (Hayes et al., 2018). Active faults in USA after USGS (Geological Survey, n.d.), Leech River fault after Morell et al. (2017), volcanoes after AGI (2003). Red box shows location of Figure 2a. DDMF – Darrington-Devils Mountain fault; FZ — fault zone; LR – Leech River fault; NO - North Olympic fault zone; OM - Olympic Mountains; VI - Vancouver Island.

active faults have been identified north of the greater Victoria region to date, including in the region surrounding the approximate epicenter of the 1946 earthquake.

Here, we investigate the kinematics and slip history of the Beaufort Range Fault (BRF), a major fault in the northern Cascadia forearc, to evaluate how forearc strain is accommodated on this structure over decadal to millennial timescales. The BRF is located on central Vancouver Island, near the northern terminus of the Cascadia subduction zone (Figure 1). Several researchers proposed that the Beaufort Range fault may have hosted the 1946 rupture, based on the proximity of the epicenter, coseismic slip modeled from geodetic benchmark surveys, and the similarity of the BRF strike to the NW-SE striking nodal plane for the event's focal mechanism (Rogers & Hasegawa, 1978; Slawson & Savage, 1979). However, no surface ruptures were found by researchers in the days and weeks following the rupture, and it remains unknown whether the BRF hosted the 1946 earthquake, or whether this fault is Quaternary-active or seismogenic.

In this paper, we undertake a field-based tectonogeomorphic investigation to evaluate the seismogenic potential of the BRF and to determine its slip history and kinematics with respect to historical seismicity and regional tectonics. We exploit a well-preserved set of offset paleochannels on the southwestern flank of the Beaufort Range, visible in recently acquired bare-earth lidar Digital Elevation Models (DEMs), to demonstrate that the BRF is a highly active, right-lateral transtensional fault that has hosted multiple surface-rupturing earthquakes throughout the Quaternary. We find evidence for at least three late Pleistocene to Holocene earthquakes along the BRF, with surface ruptures extending >40 km, consistent with paleo-earthquake magnitudes of ∼6.5 to 7.5. While these data do not constrain the age of the most recent surface-rupturing event, our results do suggest that the most recent event occurred in the past ∼3-4 kyr. We find that paleoseismic earthquakes along the BRF have kinematics similar to the 1946 Vancouver Island earthquake, suggesting that the BRF is a candidate host fault for this event. Finally, the similarities of the BRF deformation field and P- and T-axes derived from its slip over decadal to millennial timescales, suggest the stresses that lead to permanent deformation in this portion of the northern Cascadia forearc have been relatively consistent over multiple earthquake cycles.

2 Background

2.1 Tectonic Setting

The BRF is located in the northern forearc of the Cascadia subduction zone, where the Juan de Fuca plate subducts under the North American plate at a rate of ∼43 mm/yr (DeMets et al., 2010; Kreemer et al., 2014). The fault is positioned ∼150 km north of the Olympic Mountains, and ∼60 km south of the onshore projection of the Nootka fault zone, the northern end of the Juan de Fuca slab (Figure 1). Active faults that accommodate forearc strain have been recognized along most of the Cascadia subduction zone south of the Olympic Mountains (e.g., Figure 1; Brocher et al., 2001; Goldfinger et al., 1992; Liberty et al., 2003; Personius et al., 2003; Sherrod et al., 2004; Kelsey et al., 2008; R. E. Wells et al., 2020; Horst et al., 2021), and north of the Olympic Mountains (e.g., Figure 1; Schermer et al., 2021; Morell et al., 2017, 2018; Harrichhausen et al., 2021). However, no active faults have been identified in the northern 150-300 km of the forearc on Vancouver Island. It remains unclear if and how the slip accommodated by these southern faults is translated farther north and what role the BRF may play in accommodating forearc strain.

The BRF occurs along the southwestern flank of the Beaufort Range, near the city of Port Alberni on Vancouver Island (Figure 2a). The Beaufort Range consists of a ∼70 km long, ∼5-10 km wide set of peaks, whose elevations range from 1000 to 1600 masl. The range is asymmetric, with a gently sloping, glacially scoured northeastern flank that slopes toward the Strait of Georgia, and a steep (up to 35°) southwestern flank that slopes toward the Alberni Valley (Figure 2b). The BRF strikes NW-SE, following the southwestern topographic range front for >40 km (Figure 2b).

2.2 Eocene slip along the Beaufort Range thrust fault

The BRF has been previously mapped as an Eocene bedrock fault that places the Late Triassic Karmutsen Formation basalts that form the peaks of the Beaufort Range over the Cretaceous Nanaimo Group sediments that underlie the Alberni Valley (Figure 2a, Figure S1; Yorath, Clowes, et al., 1985; T. England & Calon, 1991). Geologic mapping, balanced cross sections, and LITHOPROBE seismic reflection profiles suggest this bedrock thrust fault dips NE, at 45° to sub-vertical (Yorath, Clowes, et al., 1985; Yorath, Green, et al., 1985; Clowes et al., 1987). Geologic maps depict the BRF as an along-strike projection of the frontal thrust fault of the Cowichan Fold and Thrust System (CFTS), located ∼40 km along strike to the southeast of the BRF (Cui et al., 2017; T. England & Calon, 1991). Low-temperature thermochronology data indicating exhumation at ∼50-40 Ma suggest the thrust faults of the CFTS, including the BRF, initially formed during the Eocene accretion of the Pacific Rim and Crescent terranes (T. D. J. England, 1990; T. England & Calon, 1991; T. D. J. England et al., 1997).

2.3 Glacial history

The Beaufort Range and Alberni Valley experienced two major phases of glaciation during the last glacial period. The region was inundated by the south-southwestward flowing Cordilleran continental ice sheet during the Fraser stage glaciation (∼25-12 ka; Fyles, 1963; Alley & Chatwin, 1979). Then, during the retreat of the ice sheet, the Alberni Valley was occupied by a southeastward flowing valley glacier that produced streamlined landforms and associated glacial deposits (Mosher & Hewitt, 2004; Easterbrook, 1992; Clague & James, 2002). Existing maps document sub-glacial till, colluvial, and al-

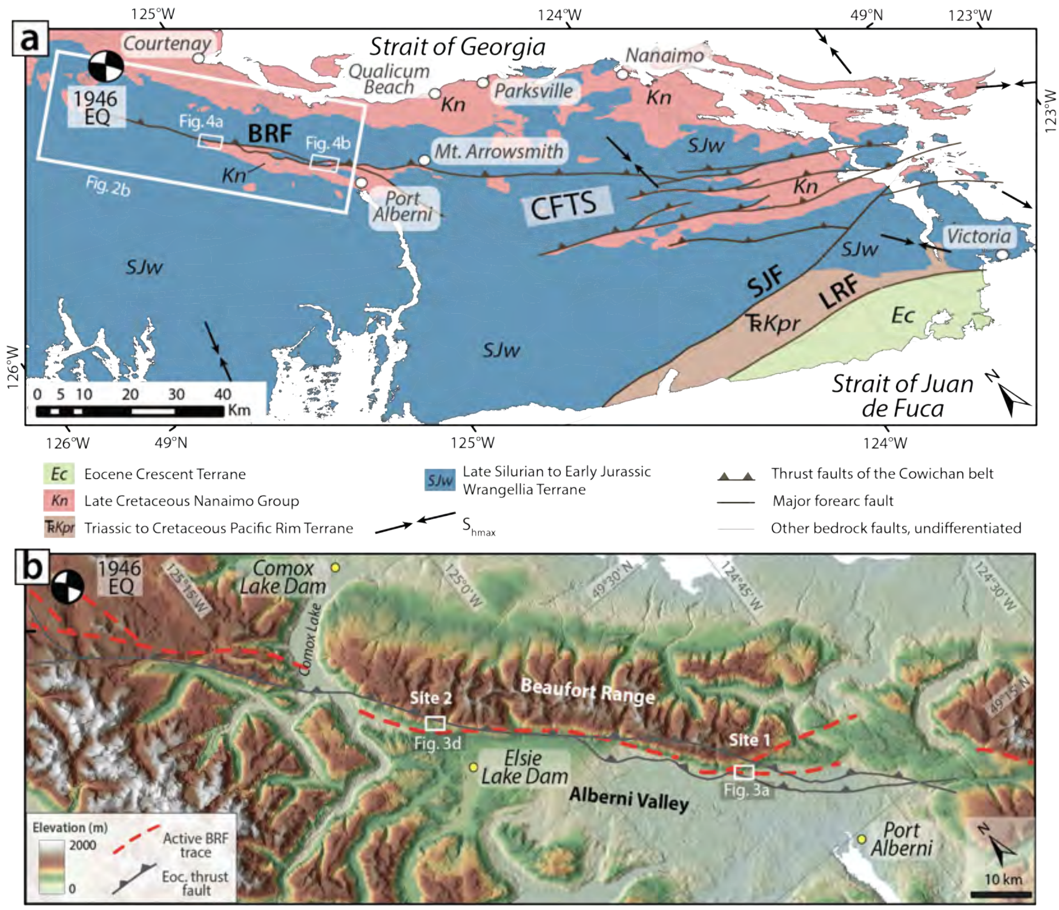

Figure 2. Geologic and geomorphic setting. **A:** Simplified geologic map of southern Vancouver Island showing major lithologic units, thrust faults of the Cowichan fold and thrust system (CFTS), and other forearc faults. The epicenter of the 1946 M 7.3 Vancouver Island earthquake is shown by the focal mechanism (Rogers & Hasegawa, 1978). Maximum horizontal stress directions after Balfour et al. (2011). Bedrock geology after the British Columbia Geological Survey compilation by Cui et al. (2017). BRF—Beaufort Range fault. LRF—Leech River fault. SJF—San Juan fault. **B:** Hillshaded SRTM DEM showing the topography of the Beaufort Range and Alberni Valley, the locations of hydroelectric dams, the trace of the Eocene bedrock Beaufort Range thrust fault (in legend), and a simplified inferred trace of the active BRF (in legend) based on the locations of mapped scarps (Supplemental Figure S1).

luvial deposits that extend to an elevation of ∼300 m along the range front (Fyles, 1963). These deposits have been correlated to the last glacial maximum at ∼13.6-11 ka, based on ages from marine shells, peat, and wood in glaciomarine deposits in the Strait of Juan de Fuca and along the eastern coast of Vancouver Island (e.g., Clague, 1980; Easterbrook, 1992). However, there has been limited surficial mapping of the Beaufort Range front, and no deposits in the Alberni Valley region have been directly dated. We expand and refine these mapping data to constrain the ages of deposits offset by scarps and evaluate the Quaternary activity of the BRF.

2.4 Possible association of the BRF with the 1946 Vancouver Island earthquake

Although post-Eocene deformation has not been previously documented along the BRF, several researchers proposed that the Beaufort Range fault may have hosted the 1946 M 7.3 Vancouver Island earthquake. The earthquake epicenter was located at the northern tip of the BRF at a depth of <30 km, and focal mechanism solutions contain a NW-SE striking nodal plane sub-parallel to the BRF (Figure 2; Rogers & Hasegawa, 1978). These data led Rogers and Hasegawa (1978) to propose that the 1946 earthquake may have been a right-lateral oblique event hosted by the BRF (Figure 2). Geodetic surveys of a triangulation network before and after the event suggest ∼1-2.5 m of right-lateral oblique slip along a steeply NE dipping (70°) fault. While multiple ground surface failures and slumps have been identified around the Beaufort Range associated with the 1946 event (Mathews, 1979; Clague, 1996), no fault-related surface ruptures associated with the 1946 event were ever discovered.

3 Methods

Our methodological approach is motivated by newly available lidar bare-earth elevation models along the surface trace of the Beaufort Range fault that reveal a series of topographic scarps that suggest the fault has accommodated Quaternary offset (Figure 2b). These scarps, clearly visible in bare-earth lidar DEMS (Figure 3), occur in en echelon arrays of 1-6 sets, each ∼100-500 m long, and spaced 10s to 100s of meters apart. The majority of well-preserved scarps are located near the base of the range—20-100 m above the valley floor, or 500-870 m below the range crest—and strike sub-parallel to the trend of the southwestern flank of the Beaufort Range front (∼290-320°; Figure 2b, Fig-

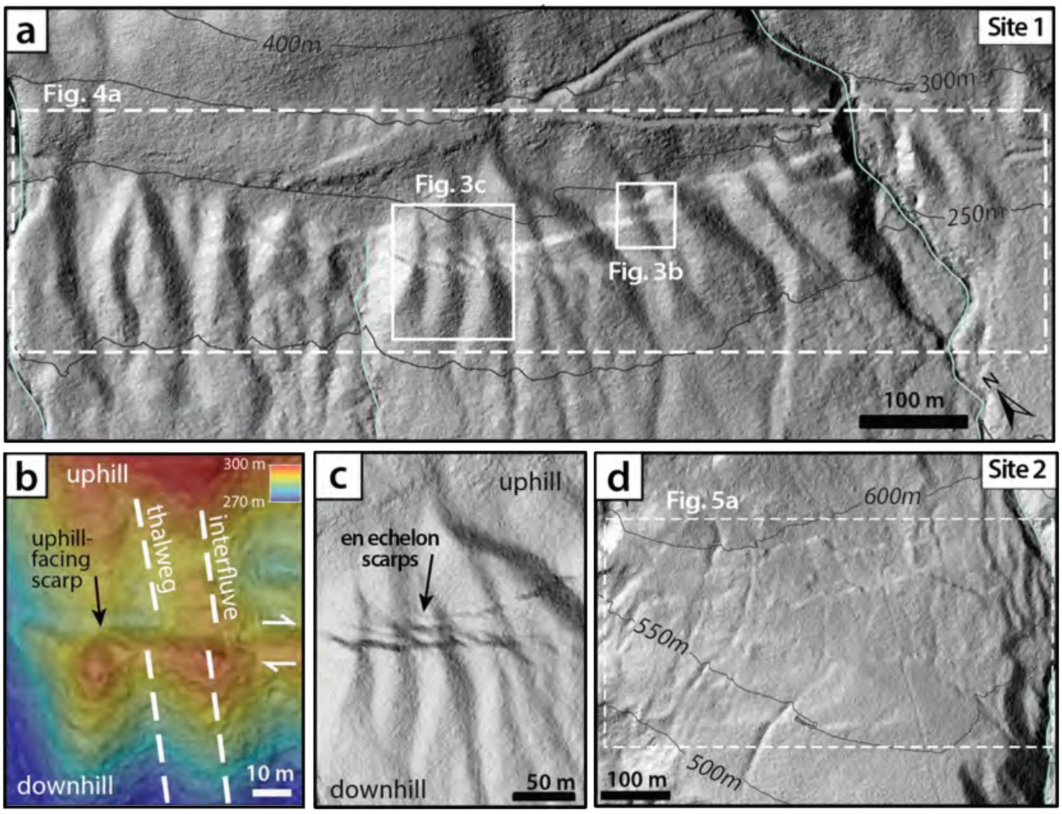

Figure 3. Examples of tectonic fault scarps visible in hillshaded bare-earth lidar DEMs. **A:** Unannotated DEM of Site 1 showing a network of en echelon fault scarps offsetting a series of abandoned channels and interfluves. **B:** Example of an uphill-facing scarp developed on a till-mantled hillside. The scarp offsets a channel thalweg and adjacent interfluve crests both vertically (downhill-side-up) and right-laterally. **C:** Example of en echelon array of scarps at Site 1. **D:** Unannotated DEM of Site 2 showing a network of right-laterally sheared channels. Examples of non-tectonic landforms are presented in Supporting Information Figure S2.

ure S1). Our initial observations of the lidar data suggested these scarps exhibit apparent right-lateral and SW-side-up 1-10-m scale displacement of a network of V-shaped paleochannels with paired offset sharp-crested interfluves. Given the glacial history of the region, we surmised that these channels may be no older than the time of ice retreat, and therefore the offset channels may record Holocene fault displacement.

Based on these initial observations, we undertook detailed field-based mapping and topographic surveying of faults and offset landforms to determine the geometry of the fault networks potentially associated with these scarps, the relative ages of offset deposits, the magnitude of potential offset, and the associated kinematics of fault slip.

3.1 Mapping

We completed surficial and bedrock mapping in order to: 1) identify earthquake-generated fault scarps along the BRF, 2) determine the relative ages of Quaternary deposits offset by surface ruptures, and 3) determine if active fault strands re-occupied inherited bedrock faults or shear zones. Identifying fault-related deformation (e.g., fault scarps) in datable Quaternary sediments is essential for characterizing the slip history of active faults (e.g., Van Der Woerd et al., 2002; Zinke et al., 2017; Hatem et al., 2017; Regalla et al., 2022), but dense temperate rainforest limits exposures and accessibility of offset Quaternary deposits in the study area. Thick soils and dense vegetative cover limit bedrock exposures to road cuts, logging roads, quarries, and stream channels, and obscure many Quaternary landforms beneath the forest canopy. However, these fault-related landforms are well-resolved in the newly available lidar point clouds collected along the BRF.

We used bare-earth lidar data, satellite imagery, and historical air photos to map potentially earthquake-generated fault surface ruptures (scarps) within a $\sim$100 km-long swath area extending from Mt. Arrowsmith to the Forbidden Plateau (Figure S1). Lidar point cloud data were collected by Terra Remote Sensing, and TimberWest and Island Timberlands logging companies provided ground returns. The lidar point clouds contained an average of $\sim$1.2-1.4 ground returns per square meter. We gridded these data into a 0.5 m DEM and generated topographic derivatives such as hillshade, standard deviation, and slope maps to aid in mapping. We additionally used satellite imagery (Google Earth Pro, 2017) and British Columbia provincial government historical air photos from

1947 and 1952 to evaluate any anthropogenic modification of key sites, including past roads, railroads, and logging trails.

We visited each accessible remotely-mapped scarp to confirm they were tectonically-generated features (i.e., not related to slumping, etc.). Criteria used to distinguish fault scarps from other features include whether the features are linear, continuous over >50-100 m length scales, are cut across topography, and if they offset hillslopes, abandoned channels, or interfluves (Figure 3b-c). We took care to distinguish potentially fault-related scarps from landforms produced by glacial deposition or scour, anthropogenic disturbance, gravitational failure, or differential erosion (see Supporting Information Text S1 and Figure S2).

We then completed highly detailed and more focused field mapping, at a scale of 1:3000, of Quaternary deposits and bedrock units in two ∼6 km by ∼2 km regions (Sites 1 and 2) that each contain a high density of fault scarps (Figures 3, 4). Surficial mapping was completed based on field and lidar-based observations of surface topography, roughness, morphology, and inset and burial relationships, accompanied by detailed lithologic descriptions of each Quaternary unit. We used these observations to create a local Quaternary stratigraphy that allowed us to determine the relative ages of units offset by faults. Bedrock mapping was completed using outcrops exposed in road cuts, streams, and quarries. We measured the structural orientations of fault planes, slickenlines, foliation fabrics, and fractures within the principal shear zones and damage zones, where exposed.

3.2 Quantifying fault slip

3.2.1 Topographic surveys of offset landforms

We collected topographic survey data across fault scarps at 64 locations at Sites 1 and 2 in order to determine the attitudes of fault planes associated with fault scarps, and to quantify the vertical and lateral offset of displaced Quaternary deposits and landforms (Figures 5 and 6). These data included 58 surveys of offset geomorphic piercing lines where the three-dimensional oblique slip vector could be calculated (Figure 7), and 6 additional "straight-line" profiles used to calculate the vertical component of displacement in locations where geomorphic piercing lines were absent (Figures 5, 6, S4, and Dryad data repository Lynch et al., 2023). Surveys were collected with a Nikon XS and Spectra Precision Focus 6 total station, which yielded more continuous topographic data than

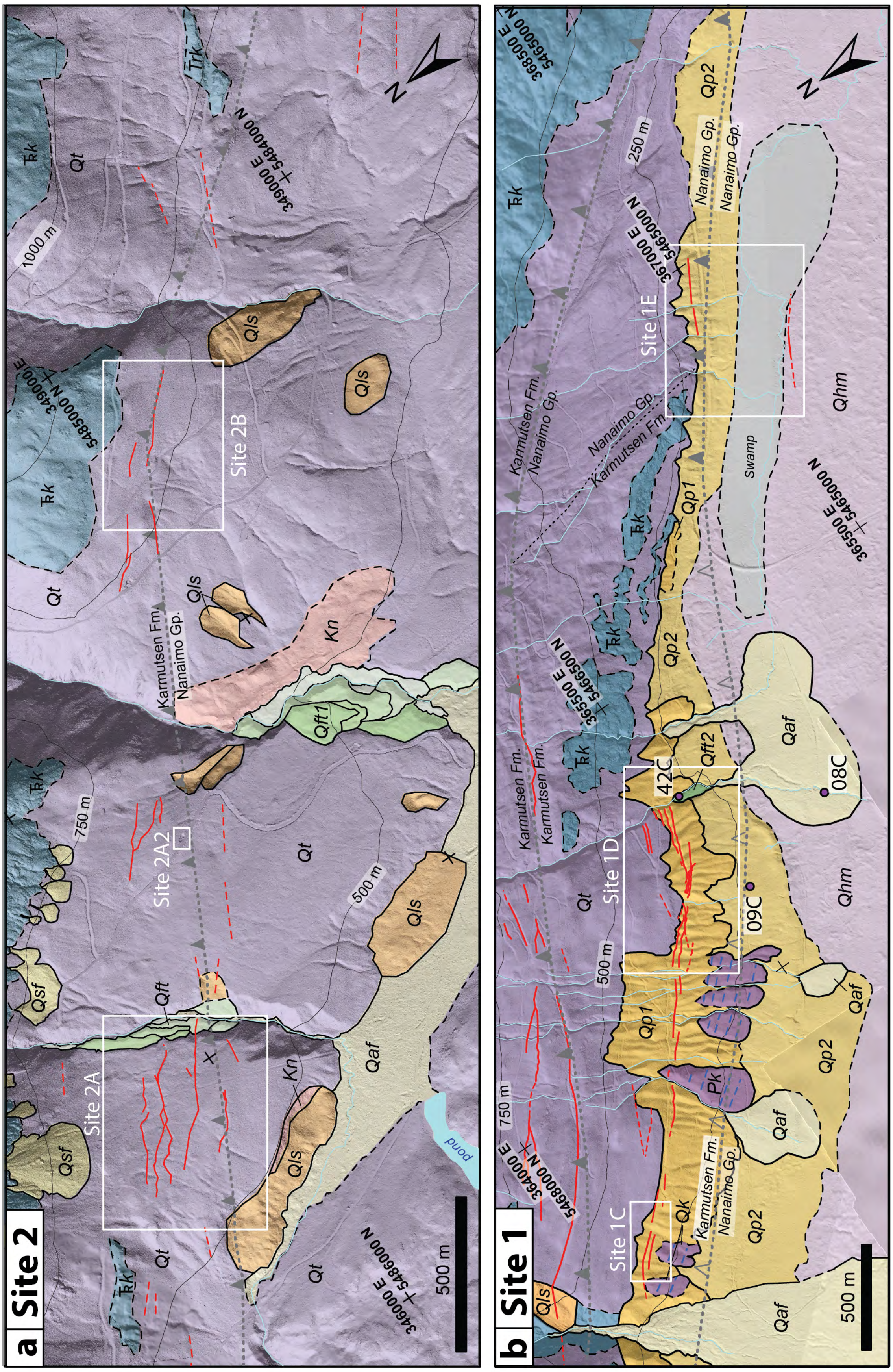

a
Site 2
Site 2A
Site 2A2
Site 2B
Karmutsen Fm.
Nanaimo Gp.
1000 m
750 m
500 m
500 m
pond
349000 E
5485000 N
349000 E
5484000 N
346000 E
5486000 N
b
Site 1
Site 1C
Site 1D
Site 1E
Karmutsen Fm.
Nanaimo Gp.
Swamp
42C
09C
08C
250 m
500 m
750 m
500 m
368500 E
5465000 N
367000 E
5465000 N
365500 E
5466500 N
365500 E
5465000 N
364000 E
5468000 N

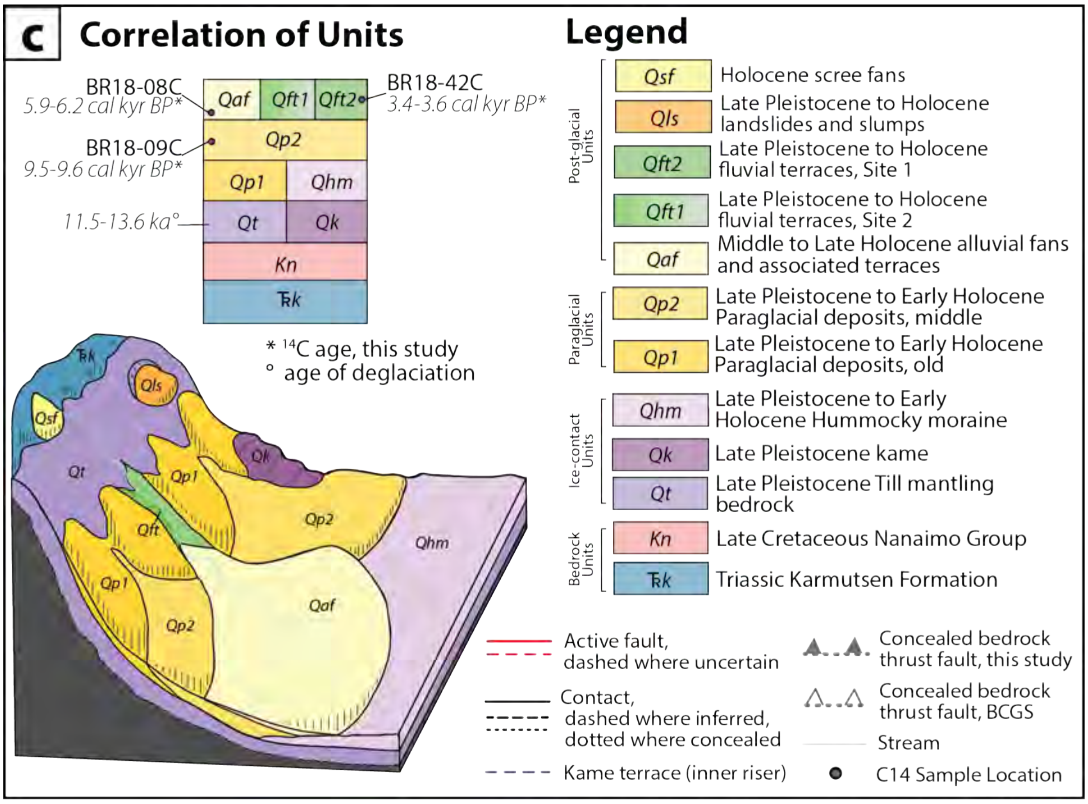

Figure 4. Bedrock and surficial geology of portions of the BRF (See locations in Figure 2a). Mapping is overlain on a composite hillshaded DEM compiled from two bare-earth lidar DEMs gridded to 0.5 m and to 2 m, and from 30 m SRTM DEM. Radiocarbon ages are reported in Table 1. Bedrock fault locations compiled from new field mapping and existing mapping by the British Columbia Geological Survey (BCGS; Cui et al., 2017). White boxes outlining Sites A-E correspond to locations shown in Figures 5 and 6. **A:** Map of Site 2 along the northern portion of the BRF. **B:** Map of Site 1, along the southern portion of the BRF. Fault scarps (red lines) occur at the base of the Beaufort Range and along the rangefront up to 1000 m above the valley floor. Mapped scarps occur in both the hanging wall and footwall of the bedrock BRF. Fault scarps offset multiple ages of glacial (Qt), paraglacial (Qp1, Qp2), and modern deposits (Qls, Qft, Qaf). Terrace generations within unit Qft1 in panel A are depicted by increasing color saturation with terrace age, delineated by thin gray lines. **C:** Correlation of units and legend for geologic maps in panels A and B. Radiocarbon ages demonstrate that these deposits are ~9600-3400 cal BP in age (Table 1).

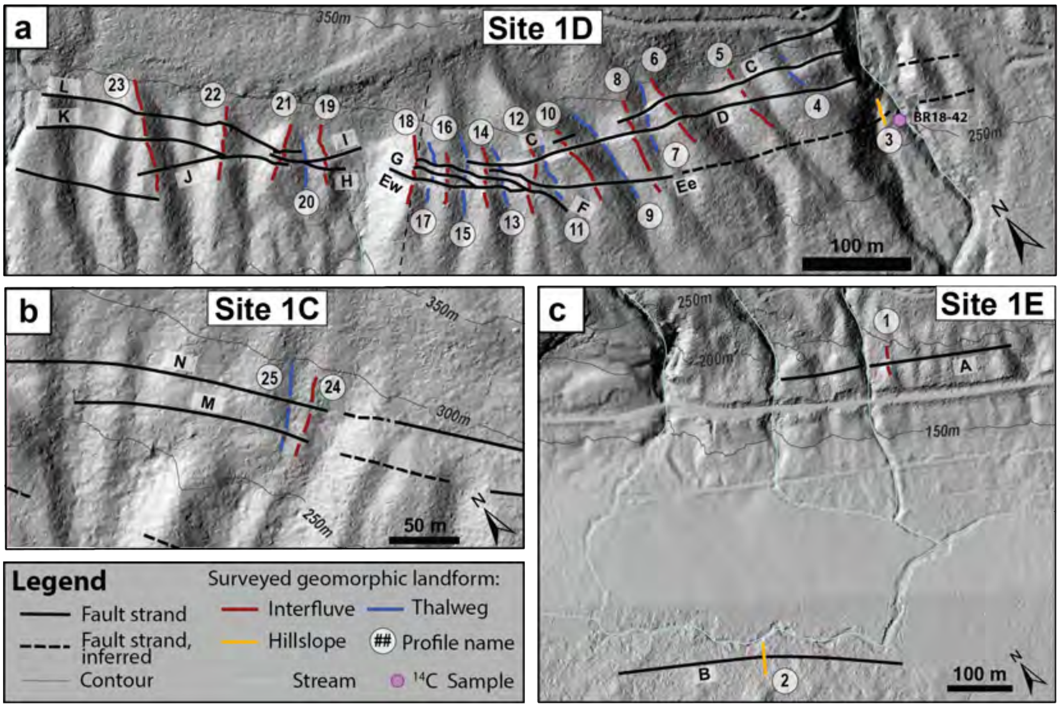

Figure 5. Hillshaded lidar DEMs of Site 1 showing mapped faults (labelled from A to N) and surveyed topographic profiles (numbered from 1 to 25). See Figure 4 for locations and Dryad data repository for topographic profile survey data (Lynch et al., 2023). **A:** Annotated hillshaded DEM showing the locations of mapped fault strands and topographic survey profiles at Site 1D. Unannotated lidar DEM is presented in Figure 3a. **B** and **C:** Annotated DEMs of Sites 1C and 1E. Unannotated versions of all DEMs are in Supporting Information Figure S3.

the lidar DEMs which had non-uniform return spacing and included some false ground returns.

Our primary survey targets were a series of abandoned channels and interfluves at Sites 1 and 2 whose axes intersect fault scarps at near-orthogonal angles, that serve as piercing lines from which fault slip vectors can be reconstructed. Topographic surveys of these landforms followed either the channel thalweg or the interfluve crest. In locations where channels and interfluves are absent, we collected linear profiles with trends perpendicular to the fault scarp. For each profile, total station survey data were collected every ~0.5-1 m, to a distance of >20 m uphill and downhill of each fault scarp (Figure 7). Along survey transects where a geomorphic piercing line extended for less than 20 m (e.g., between closely-spaced fault strands), we collected a minimum of 3 survey points, with an average of 11 points. We complemented these ground surface elevation profiles

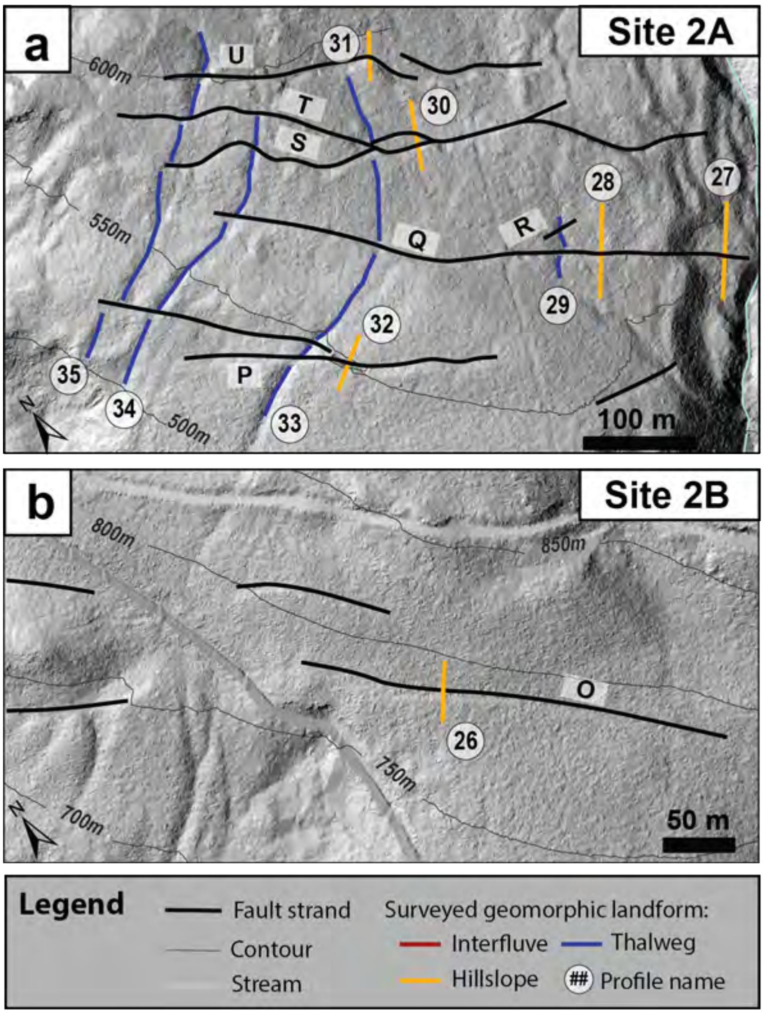

Figure 6. Hillshaded DEMs of Site 2 showing mapped faults (labelled from O to U) and surveyed topographic profiles (numbered from 26 to 35). See Figure 4 for locations and Dryad data repository for topographic profile survey data (Lynch et al., 2023). **A:** Annotated hillshaded DEM showing the locations of mapped fault strands and topographic survey profiles at Site 2A. Unannotated lidar DEM is presented in Figure 3d. **B:** Annotated DEM of Site 2B showing mapped faults and surveyed profile. Unannotated versions of all DEMs are in Supporting Information Figure S3.

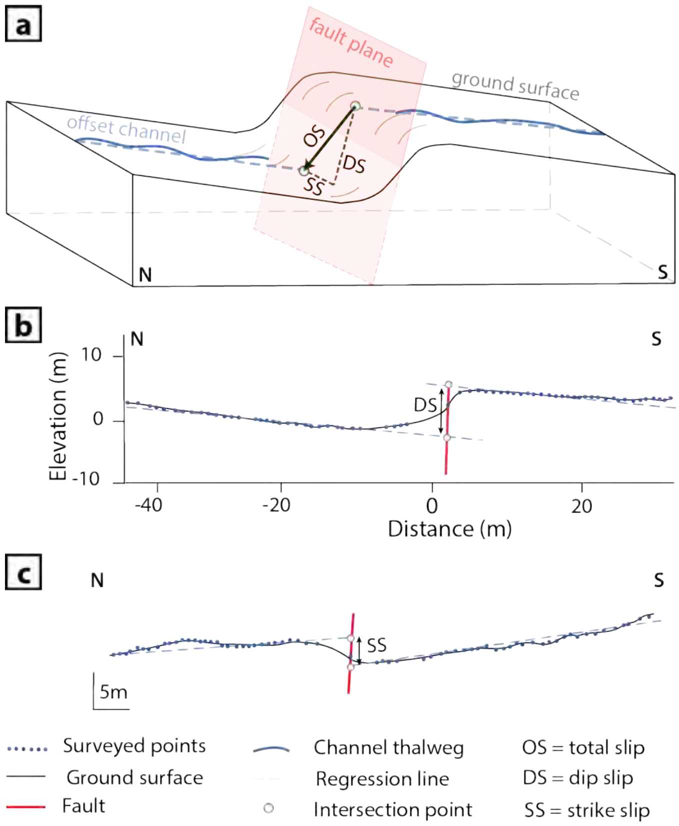

Figure 7. Schematic diagrams showing how surveyed geomorphic piercing lines were used to reconstruct 3D fault slip. **A:** Block diagram showing an oblique normal right lateral offset channel thalweg. Fault slip components (OS, DS, and SS) are calculated from the 3D positions of the intersections of the fault plane with the linear projections of the upthrown and downthrown channel segments. **B:** Example of a surveyed geomorphic piercing line profile in cross-section. **C:** Example of a surveyed geomorphic piercing line profile in plan view. In each survey, points were collected every ∼0.5-1 m at least 10-20 m beyond the fault scarp.

with six additional topographic profiles extracted from lidar DEMs in a portion of Site 2A where thick forest cover and uneven topography prevented total station surveys of offset abandoned channels.

3.2.2 Reconstructing oblique fault displacement

We used the topographic survey data to reconstruct both the magnitude and orientation of the slip vector at each surveyed location where a geomorphic piercing line intersected an individual fault plane. In order to calculate a slip vector, the local orientation of the fault plane must be known. No outcrop exposures of fault planes in Quaternary deposits were present in the field area, but we were instead able to reconstruct the local strike and dip of the fault plane associated with mapped scarps using a modified three-point problem approach. In this approach, we assumed the midpoint, or inflection point, of a fault scarp represents the most likely intersection of the fault plane with the surface. We surveyed scarp midpoints at a range of elevations ($\sim$4-12 m elevation range) and determined fault strike and dip through linear regression of a plane through the surveyed scarp midpoints using all surveyed data along a single continuous fault strand segment (3-17 points per regression). We used these data to determine a representative fault dip for each scarp segment, using the average dip from all regressions at Site 1 or Site 2, and a representative fault strike given by the local strike of each fault strand or segment. Because fault dips determined from surveys of degraded scarp faces over small elevation ranges may underestimate true fault dip, we allowed our model reconstructions to permit fault dip to be 5° steeper than that calculated from the three-point approach.

We combined our fault plane solutions and topographic survey data to calculate the 3D offset of each piercing line, specifically the magnitude and direction (trend and plunge) of the slip vector (Figure 7). Calculations were made using an R script that performed a Monte Carlo simulation to evaluate the slip vector and associated uncertainty (script available in data repository, Lynch et al., 2023). The script requires the following user-defined inputs: the strike and dip of the fault plane, the 1σ uncertainty on strike and dip, the XYZ coordinates of the topographic survey data, the location where the fault plane intersects the ground surface, and the number of survey points in the upthrown and downthrown sides of the profile used to define the 3D geometry of the piercing line segments. For each profile, we assigned a fault strike and dip as described above, and $\pm$ 1σ uncertainty (5°). We manually defined the remaining parameters—fault plane intersections, and the number of survey points used to fit linear regressions through the upthrown and downthrown surveyed piercing lines—for each topographic profile. It has been well-documented that how a user defines fault and piercing line geometry (i.e., profile regression limits) can lead to multiple admissible geologic slip reconstructions (e.g., Scharer et al., 2014). To account for this uncertainty, we performed Monte Carlo simulations for each offset profile using input defined by five different users, each trained in scarp offset analysis.

Using these inputs, we used the R script to calculate 3D linear regressions through topographic survey points on the upthrown and downthrown sides of the fault scarp and then solve for the intersection points of these lines with the fault plane (Figure 7). These two intersection points were then used to calculate the magnitudes of strike slip (SS), dip slip (DS), and oblique slip (OS) for each piercing line, as well as the trend and plunge of the slip vector (Figure 7). The Monte Carlo simulation was repeated 100 times for each of the five user-defined profile selections, yielding a total of 500 simulations of fault slip for each displaced piercing line. We report the outputs as the mean ± one standard deviation of the 500 values calculated for that profile.

3.2.3 Inversion for fault kinematics

We use the slip vector data to invert for the kinematics of the BRF using the FaultKin 7.6 program (Marrett & Allmendinger, 1990; Allmendinger et al., 2012). Data inputs included the trend and plunge of the best-fit slip vector determined from the Monte Carlo simulations, and the corresponding fault plane strike and dip determined from the modified three-point fault plane regressions. Inversions were performed using data from each of the 55 fault scarp surveys with vertically and laterally offset piercing lines. We grouped data for kinematic inversions in two ways. First, we grouped data collected at each mapping sub-site (A-E in Figure 4), to produce kinematic inversions representative of slip observed at each site location. Then, we grouped all data for the entire BRF to determine a kinematic inversion best fit to all observed data. Kinematic inversions were performed by calculating P- and T-axes from each calculated slip vector and fault plane pair, and then generating Bingham fault plane solutions from the set of P- and T-axes at each site (Marrett & Allmendinger, 1990; Allmendinger et al., 2012). These inversions assume slip occurs in the direction of maximum resolved shear stress on the fault plane, and produces mean P- and T-axes, pseudo focal mechanisms, and predicted slip vectors for each nodal plane (Marrett & Allmendinger, 1990; Allmendinger et al., 2012). These kinematic inversions and P- and T-axes provide information about paleo strain fields, and may, under certain assumptions, be used to approximate local stress axis orientations at the time of deformation (e.g., Angelier & Mechler, 1977; Riller et al., 2017).

3.3 Radiocarbon dating of Quaternary deposits

We collected charcoal samples from natural and manmade exposures of mapped Quaternary deposits to determine the chronologic ages of units offset by mapped faults. We focused our sampling on detrital charcoal as charcoal is present in many deposits on Vancouver Island, has previously been used to evaluate late Pleistocene to Holocene unit ages (e.g., Clague, 1980; Morell et al., 2018; Harrichhausen et al., 2021), and because luminescence techniques have not yielded reliable ages for late Pleistocene to Holcoene deposits due to insufficient dose rate (e.g., Graham, 2017; Morell et al., 2018). We collected samples of macroscopic (macro) charcoal (>0.5 cm) where fragments were visible in outcrops of Quaternary deposits. If no macro charcoal was readily visible in an outcrop, we collected 1-2 L of bulk sediment and sieved the samples to extract any datable macro charcoal present. For all sample sites, we completed detailed unit descriptions and noted the sample's stratigraphic position within the deposit (Figure S3). We collected three macro charcoal samples and five bulk sediment samples from Site 1 (see Figure 4b for locations). Our sampling was focused on units mapped at Site 1 (Figure 4b), where we identified multiple generations of Quaternary deposits (see Section 4.2). We were unable to date any mapped deposits at Site 2 due to a lack of exposure.

Charcoal samples were cleaned and processed at Paleotec Services, Ottawa, Ontario, Canada. Macroscopic charcoal pieces were extracted from bulk sediment samples by flotation and wet sieving in warm tap water using nested sieves of 0.85 mm and 0.425 mm. All material greater than 0.425 mm was examined using a binocular microscope, and any isolated charcoal pieces were shaved of any adhering sediment. The largest shaved fragment from each sample was further sliced into smaller fragments to look for the presence of fine modern rootlet penetration and/or fungal contamination, including mycorrhizae, and rejected if contaminants were present.

Three Quaternary units yielded datable charcoal fragments that were processed for radiocarbon analysis (Table 1, Figure 4b). These included macro charcoal samples extracted from one outcrop (BR18-06C, -07C, and -08C), and two samples extracted from sieved bulk sediment from two additional outcrops (BR18-42C and BR18-09C). Sample BR18-08C was selected as the highest quality sample of the three charcoal fragments extracted from the outcrop exposure. Bulk sediment sample BR18-09C included three mm-sized charcoal pieces that were combined to ensure adequate sample mass for AMS after acid-base-acid (ABA) treatment (Table 1, Figure 4b, Figure S3). Unfortunately, the three remaining bulk sediment samples (BR18-10C, -11C, and -12C) were barren of charcoal. Samples were analyzed at the Keck Carbon Cycle AMS Laboratory at UC Irvine. Radiocarbon ages (reported following Stuiver & Polach, 1977) were calibrated using the INTCAL20 calibration curve (Reimer et al., 2020) and OxCal v4.4 (Bronk Ramsey, 1995, 2021). We report radiocarbon ages as the two-sigma (2σ) range of calendar years before present (1950).

3.4 Estimates of fault slip

We estimate slip rates at Site 1 using the cumulative oblique displacement measurements of three different ages of offset landforms, as well as radiocarbon dates from detrital charcoal that provide estimates of unit ages. We use two approaches to estimate slip rates, following the methods of DuRoss et al. (2020). The first is an "open-ended" approach that uses the cumulative slip of the oldest offset unit and that unit's estimated age. The second is a "closed interval" approach that uses the difference in slip that has occurred during a known time interval that encompasses one or more complete recurrence periods. We report both slip rate calculations and discuss the relative applicability of each.

4 Results

Our mapping provides several lines of evidence that the BRF is Quaternary-active, and has experienced multiple slip events since the late Pleistocene. Field mapping of the morphology and spatial distribution of fault scarps (Figures 3 and 4) indicates that the mapped scarps are of tectonic origin, produced during one or more surface-rupturing earthquakes, and are not the product of glacial, gravitational, or anthropogenic processes. An active BRF is further supported by the presence of numerous right-laterally and vertically offset abandoned stream channels incised into Late Pleistocene to Holocene till and paraglacial deposits. Below we discuss the morphology of the fault scarps, the ages of offset deposits, the kinematics of fault slip derived from measured offsets of channel networks, and our interpretations of the number and relative timing of events that have occurred along the BRF since the last glacial maximum.

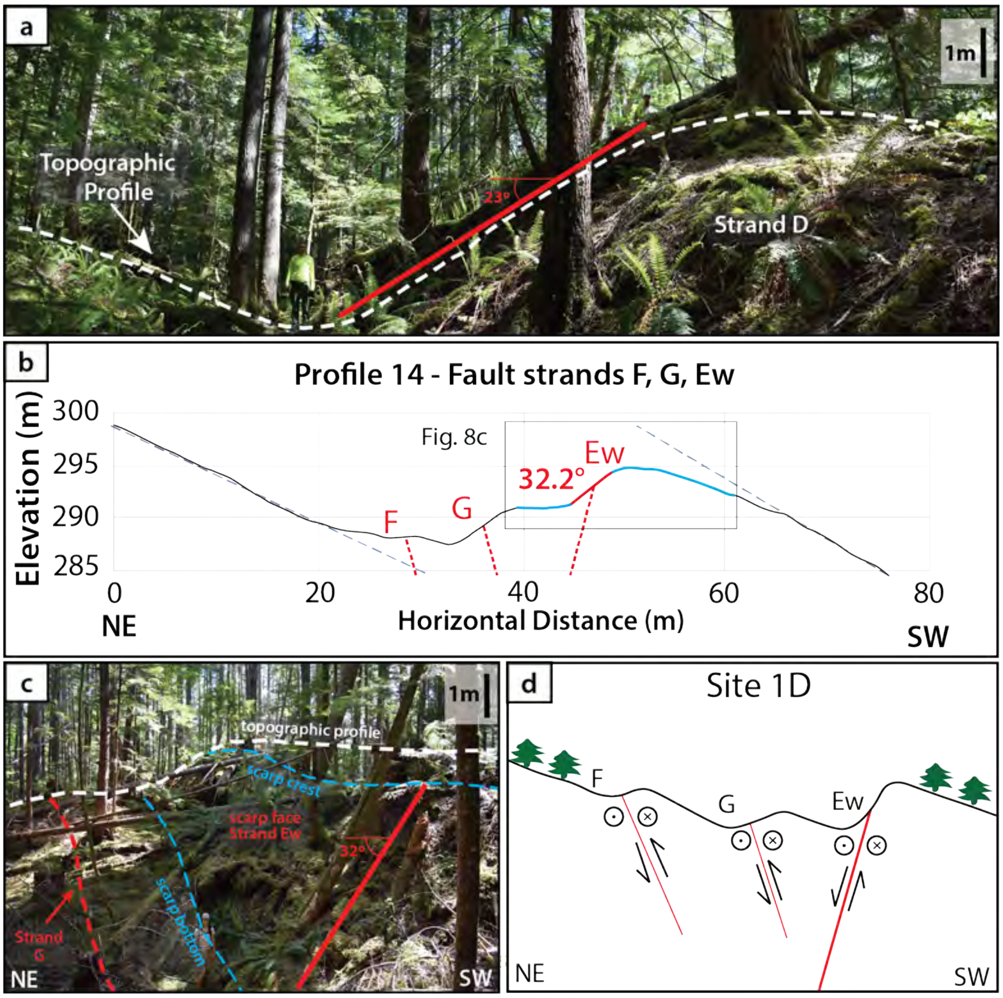

Figure 8. Examples of fault scarps identified along the Beaufort Range fault. **A:** Tall, uphill-facing, moderately steep (∼23°) fault scarp along strand D at Site 1D (Figures 4b, 5a). **B:** Topographic profile across three scarps at Site 1D associated with fault strands F, G, and Ew extracted from bare-earth lidar DEM (Profile 14, Figure 5). Dashed dark blue lines show the projection of the background hillslope toward the scarps. **C:** Photo of the tall, steep preserved face of Strand Ew shown in the topographic profile in panel b. The uphill-facing fault scarp along strand Ew is ∼32°, nearly angle of repose, much steeper than the scarp face along strand D (panel a). **D:** Cartoon cross-section showing the schematic relationships between sets of sub-parallel and en echelon fault strands, based on observations at Site 1D. These strands are interpreted to merge at depth in a flower structure consistent with strike-slip faulting.

4.1 Quaternary fault scarps

Our mapping shows that the Quaternary-active BRF is defined by a series of sub-parallel, discontinuous fault scarps (n=153) that offset multiple ages of Quaternary deposits preserved on the southwestern flank of the Beaufort Range (Figure 2a, Figure S1). The spatial distribution of preserved scarps shows they are part of an ∼500 m wide fault zone, where slip is distributed across multiple (∼1-6) sub-parallel, steeply-dipping fault strands (Figure 8, Figure S1). Individual fault scarps locally exhibit strike lengths of ∼100-1500 m, exhibit scarp heights of ∼0.5-6 m, and occur in en echelon or parallel sets with intra-fault spacings of 5-100 m. Scarp facing directions can vary locally over short distances but about two thirds of the scarps (n=101) face NE. Most (∼70%) of the mapped faults have asymmetric cross-sectional morphologies with steep uphill-facing scarps, while a smaller fraction are preserved as flat, degraded topographic features embedded in the high-gradient hillslopes (Sites A-E; Figures 3, S2, S4). Our mapping demonstrates that active fault strands generally strike NW, parallel to the range (average ∼287°, with variation of up to 20°-38°), and our topographic field surveys (see Section 3.2.2) indicate that near the surface, most strands dip steeply NE (∼60°-88°), with a few dipping steeply SW (∼70°).

The steepness and morphology of the scarp faces vary both along strike and between strands. At Site 1, the steepest and tallest scarps are 4-6 m tall and have scarp faces near the angle of repose (32° strand Ew at Site 1D; Figures 5, 8). Many of the scarps at Site 1 exhibit steep, well-preserved free faces, such as strand Ew at Site 1D (Figure 8b-c). Other scarps at Site 1 exhibit a more moderate, 24° dipping scarp face (Figure 8a), such as Strand D at Site 1D. At Site 2, the scarps are 1-3 m tall and have faces near the angle of repose (∼45° strand U at Site 2A; Figures 6 and S5), and some are large and steep enough to have effectively ponded large boulders sourced from uphill (Figure S5). Several of the individual scarps at Site 1 are part of a larger, multi-fault scarp that includes multiple emergent fault strands (Figure 8b), whereas individual scarps at Site 2 appear to occur as separate parallel or anastomosing fault sets (Figure 6).

Our mapping shows that the majority of active fault scarps are not directly co-located with known bedrock fault planes at the surface (Figures 4 and S1). At Site 2, the primary bedrock thrust fault, which places Karmutsen Fm basalts over Nanaimo Gp sediments (Figure 4a), is exposed as a 200+ m wide damage zone that juxtaposes hanging wall basalts against an upright, open, footwall syncline of Nanaimo Gp sandstones. Mapped

Quaternary fault scarps do not appear co-located with the exposed bedrock fault plane at the surface, but instead occur in sub-parallel networks spanning up to 500 m away, in both the hanging wall and footwall. Similarly, at Site 1 where the bedrock thrust branches into two strands, mapped Quaternary faults occupy a zone that is ∼500 m wide, and occur up to 500 m away from mapped bedrock thrust faults (Figure 4b).

Quaternary fault scarps also have different slip senses and attitudes than observed along the bedrock thrust faults. Slickenlines and Riedel shear geometries (Figure S7) on Eocene bedrock thrust faults indicate apparent NE-side-up, dominantly dip-slip displacement, whereas the active faults exhibit southwest-side-up and right-lateral displacements (Figure S7). Outcrop exposures of the bedrock thrust fault at both Site1 and Site 2 exhibit strike orientations that differ from Quaternary scarps by ∼15°. Our field surveys indicate that the active fault BRF strands have dips of 70°-90° NE, whereas exposures at several sites along the range suggest the inherited thrust fault has a dip of <40° NE to sub-vertical. These observations indicate that mapped active fault scarps are not produced by slip along inherited structures in the near subsurface, but instead occupy a zone that is generally sub-parallel to the inherited structure.

4.2 Quaternary mapping and stratigraphy

Quaternary fault scarps along the BRF displace a series of nine units that were deposited during the late Pleistocene to Holocene deglaciation and subsequent transition to a post-glacial environment. We develop a local Quaternary stratigraphy (Figure 4 and Table S1) that groups these deposits into three categories: ice-contact glacial units deposited during the most recent glaciation, paraglacial units deposited during ice retreat and slope readjustment, and post-glacial units deposited after ice retreat.

4.2.1 Ice-contact glacial deposits and landforms

The ice-contact glacial units are the oldest and stratigraphically lowest Quaternary units mapped in the study area and include subglacial till (Qt), kame terraces (Qk), and hummocky moraine (Qhm) (Figure 4; Table S1). The subglacial till (Qt) is a very indurated, matrix-supported diamict containing both locally-derived and exotic clasts and is up to 40 m thick. Qt mantles bedrock along the southwestern flanks of the Beaufort Range mountain front at elevations >150-400 m. Kame terraces (Qk) occur as a series of five evenly-spaced, flat-topped terrace treads with steep risers, at 150-300 masl (<150 m above the valley floor), underlain by indurated, poorly to moderately sorted, stratified sands and gravels. Hummocky moraine (Qhm) is present on the valley floor at elevations of <150 masl at Site 1.

4.2.2 Paraglacial deposits and landforms

Glacial deposits are overlain by two generations of paraglacial deposits, Qp1 and Qp2 (Figure 4c; Table S1). Qp1 consists of indurated, clast-supported, poorly-sorted, stratified sands and gravels. Qp1 deposits occur as cone-shaped landforms whose heads merge into Qt and whose toes are buried by Qp2 at the foot of the range. Qp2 has a similar composition to Qp1 and consists of thinly-bedded, clast-supported, stratified sands and gravels with occasional coarse sand lenses. Qp2 is distinguishable from Qp1 based on inset and burial relationships and its position at lower elevations on the range front.

Qp1 is incised by a series of abandoned channels. These channels are disconnected from active streams but merge into the heads of Qp2 deposits, suggesting that they were active at the time of deposition of Qp2. Abandoned channels at Site 1 are typically ∼1-4 m deep, have V-shaped cross-sectional morphologies and are separated by adjacent interfluves with linear ridges and steep flanks, or are incised into till and colluvium-mantled hillslopes (Figures 3 and 4). We interpret these abandoned channels to have formed as the result of fluvial and debris flow scouring and filling associated with the deposition of Qp2. At Site 2, offset abandoned channels have broad cross-sectional morphologies and are moderately incised into hummocky, till-mantled hillslopes (Figures 3 and 4). These channels do not clearly merge into other mapped deposits but appear to be cross-cut by younger landslides at the foot of the range.

4.2.3 Post-glacial units and landforms

The youngest units include post-glacial landslides (Qls), scree fans (Qsf), alluvial fans (Qaf), and fluvial terraces (Qft1 and Qft2) that either bury or are inset into the glacial and paraglacial deposits (Figure 4, Table S1). Mapped landslides (Qls) are hummocky deposits associated with curvilinear headscarps and oversteepened toes and have widths of 50-600 m. Scree fans (Qsf) are small (30-250 m across), fan-shaped deposits with rough surfaces that contain cobble to boulder-sized bedrock clasts. Qsf occurs at the bases of mapped bedrock exposures at elevations of ∼750 masl. Alluvial fan deposits (Qaf) are defined as a series of broad, convex, gently-sloping fans headed in active or recently-active channels (Figure 4). The fans consist of poorly to moderately sorted, clast-supported, stratified alluvial and fluvial deposits containing silt, sand, pebbles, and boulders, with occasional clast imbrication and cross-bedding (Table S1). Qaf deposits are mapped at the base of the range front and bury portions of Qp2, Qt, and Qhm.

At two locations in Site 2, and one at Site 1, Qaf fan heads merge into deeply incised (by ~1-15 m) streams that are flanked by a series of up to five fluvial terraces (Qft1 and Qft2). Fluvial terrace treads are 20-130 m wide, slope gently downstream, and have risers up to 5-10 m tall. The deposits that underlie these terraces are moderately to well-sorted, clast-supported sediments, with sub-horizontally stratified interbeds of rounded cobbles, boulders, and pebbles. We subdivide these fluvial terraces into two generations (Qft1 and Qft2) based on the inset relationships observed at Sites 1 and 2. At Site 2, Qft1 terraces are inset into till-mantled bedrock and are, in turn, incised by channels feeding Qaf alluvial fans (Figure 4b). This observation shows that at Site 2, Qft1 terraces are older than Qaf. In contrast, at Site 1, Qft2 appears to grade into the channels that feed Qaf, indicating that Qft2 terraces are younger than at Site 1 and are instead correlative to upper portions of Qaf or the channels inset into Qaf (Figure 4a).

4.2.4 Radiocarbon results and inferred unit ages

We use radiocarbon ages from detrital charcoal extracted from Quaternary deposits to place brackets on the possible ages of mapped units offset by BRF scarps. We note that the interpretation of detrital charcoal radiocarbon dates can be challenging due to vertical mixing during bioturbation or soil creep, recycling of older charcoal into younger deposits, and bias from younger carbon (e.g., roots) included in older charcoal. However, the radiocarbon ages that we obtained from Quaternary units in the map area are in broad agreement with our local relative Quaternary stratigraphy (Figure 4) and with regional constraints on the timing of deglaciation and post-glacial processes (e.g., Halsted, 1968; Alley & Chatwin, 1979; Blaise et al., 1990; Clague, 1994). We use these data, therefore, to make the following interpretations of unit ages.

The three ice-contact glacial deposits, Qt, Qk, and Qhm, were barren of charcoal and could not be directly dated (Table 1). This absence is consistent with other studies on Vancouver Island that have found ice-contact deposits to be devoid of charcoal (Morell et al., 2018; Harrichhausen et al., 2021). We interpret Qt, Qk, and Qhm to be associated with the last glacial maximum, which has been regionally dated to ~11.5-13.6

ka (Halsted, 1968; Alley & Chatwin, 1979; Blaise et al., 1990; Clague, 1994), although we recognize the possibility that deposits associated with prior glacial periods may be present in the study area.

We attempted to radiocarbon date both Qp1 and Qp2 debris-cone fan deposits, but only Qp2 yielded datable charcoal. The charcoal sample was collected from a stratified fan deposit ~30 cm below the surface of Qp2 (BR18-09C), in a roadcut exposure located ~250 m SW of the fault scarps at Site 1 (Figure 4, Figure 3). This sample yielded an age of ~9.5 cal ka (Table 1), consistent with the older estimated age of the Late Pleistocene glacial deposits (Qt, Qk, and Qhm) of ~11.5-13.6 ka, and younger radiocarbon ages of samples from Qaf and Qft2 (see below). The ~9.5 cal ka age is also broadly consistent with the timescales of paraglacial debris cone formation documented in recently deglaciated terrains that suggest these types of deposits form in the first 100s-1000s of years following deglaciation (Ryder, 1971; Ballantyne & Benn, 1996; Ballantyne, 2002).

Post-glacial units Qaf and Qft2 also yielded datable macro-charcoal fragments. Qaf yielded one macro-charcoal sample (BR18-08C). This sample was collected from a stratified, clast-supported sand lens within interbedded sands and gravels ~0.75 m below the top of the deposit located ~500 m SW of fault scarps at Site 1 (Figure 4 and 3). This sample yielded a radiocarbon age of ~6 cal ka (Table 1). Qft2 yielded a charcoal sample (BR18-42C) sieved from bulk sediment collected from a stream cut exposure of stratified pebbles and cobbles, located <10 m downhill from mapped fault strand Ee (Figure 4b, Figure 3). This sample yielded a radiocarbon age of ~3.5 cal ka (Table 1). Both ages are younger than the ages determined from a radiocarbon sample from paraglacial deposit Qp2 (~9.5 cal ka), and agree with our stratigraphic interpretation that Qaf is older than Qft2.

If we assume that these samples reflect deposit ages, and are not significantly altered by recycling, bioturbation, or inclusion of younger carbon, these data suggest the following as possible brackets on the ages of mapped deposits. Qt, Qk, and Qhm are likely ~11-14 ka, paraglacial deposits Qp1 and Qp2 are likely ~6 to ~11 ka, Qaf units are likely ~3 to ~9 ka, and Qft2 deposits are likely <4 ka. Given the uncertainties inherent with this method and with the small number of samples available for dating, we treat these as age approximations.

Table 1. Radiocarbon sample data at Site 1D (see Figures 4b and 4c for locations).

Unit[a]	**Coordinates**[b]	**Sample Name**	**Sample Type**	**Dated Material**	**UCIAMS ID**[c]	**Fraction Modern**	**D14C (‰)**	**Radiocarbon Age**[d] **(years BP, 2 σ)**	**Calibrated Age**[e] **(cal BP)**
Qft2	364944 E, 5466432 N	BR18-42C	Bulk sediment	Charcoal (single piece)	215248	0.6658 ± 0.0013	-334.2 ± 1.3	3265 ± 20	3560-3400
Qaf	364561 E, 5465854 N	BR18-06C	Macro charcoal	Not dated	–	–	–	–	–
		BR18-07C	Macro charcoal	Not dated	–	–	–	–	–
		BR18-08C	Macro charcoal	Charcoal (single piece)	215248	0.5185 ± 0.0010	-481.5 ± 1.0	5275 ± 20	6180-5940
Qp2	364400 E, 5466402 N	BR18-09C	Bulk sediment	Charcoal (composite of three pieces)	215249	0.3428 ± 0.0008	-657.2 ± 0.8	8600 ± 20	9600-9520
	0364683E, 5466207N	BR18-10C	Bulk sediment	barren	–	–	–	–	–
Qp1	0365209E, 5466352N	BR18-11C	Bulk sediment	barren	–	–	–	–	–
	0364515E, 5466653N	BR18-12C	Bulk Sediment	barren	–	–	–	–	–

[a] See Figure 4 and Table S1

[b] NAD83 UTM Zone 10

[c] Samples were prepared at PaleoTek Services. Sample preparation backgrounds have been subtracted, based on measurements of ^{14}C-free wood. These samples were treated with acid-base-acid (1N HCl and 1N NaOH, 75°C) prior to combustion. Samples were processed at the UC Irvine Keck AMS facility.

[d] All results have been corrected for isotopic fractionation according to the conventions of Stuiver and Polach (1977), with $d^{13}C$ values measured on prepared graphite using the AMS spectrometer. These can differ from $d^{13}C$ of the original material, and are not shown.

[e] Radiocarbon ages calibrated using INTCAL20 (Reimer et al., 2020) and OxCal v. 4.4 (Bronk Ramsey, 2021). Range reported represents unmodeled 95% confidence interval as calculated by OxCal.

4.3 Fault offset measurements

Results of our field mapping and topographic surveys show that the BRF has accommodated several meters of vertical and right-lateral displacement, distributed over a network of one to six fault strands that offset the mapped late Pleistocene to Holocene deposits (Figure 3). At Site 1 (Figure 5), scarp heights on individual fault strands range from 0.5 to 6 m, and channels appear in the field to be right-laterally offset by ∼0.5-2 m. These observations suggest cumulative displacements of several meters across multiple fault strands. Similarly, at Site 2, scarp heights range from 1 to 3 m, and a series of three stream channels visible in lidar appear to be systematically right laterally sheared by several meters across three to five fault strands (Figure 6). Our field observations and survey data also show that scarp heights in older deposits and landforms, including the interfluves developed in Qp1 at Site 1 and the till-mantled hillslopes at Site 2, have larger vertical displacements than the younger channels incised into these deposits, suggesting the potential for multiple events.

4.3.1 Slip vectors and fault kinematics

Estimates of slip based on our topographic survey data confirm our field observations that the BRF exhibits consistent right-lateral and dip-slip offset of the ground surface. Oblique slip magnitudes across individual fault strands range from ∼2 to 7 m at Site 1 and from ∼2 to 5 m at Site 2 (Table S2). Average dip-slip magnitudes for single faults range from ∼1 to 5 m, with the largest dip-slip magnitudes of up to ∼9 m observed at Site 1D (Table S2). Average right-lateral strike-slip magnitudes recorded in offset channels and interfluves at Sites 1 and 2 range from ∼1 to 5 m. Displacements of piercing lines across individual strands yield a ∼0.3:1 to 1.5:1 ratio of strike slip to dip slip, similar to those yielded by the cumulative displacements (Table S2). These data suggest that, while the fault system as a whole accommodates approximately equal magnitudes of strike slip and dip slip, some individual fault strands are dominated by dip slip, while others are dominated by strike slip.

Kinematic inversions of BRF slip vector data produce pseudo focal mechanisms that similarly indicate right-lateral transtension along a steeply NE-dipping fault (Table S3). Inversions performed for Sites 2A, 1C, 1D, and 1E (Figure 9 a-d) show small variations in the average strike and dip of the primary slip plane of 292-321° and 66-78°, and in the average trend (095-153°) and plunge (10-26°) of the model slip vectors. These site-specific

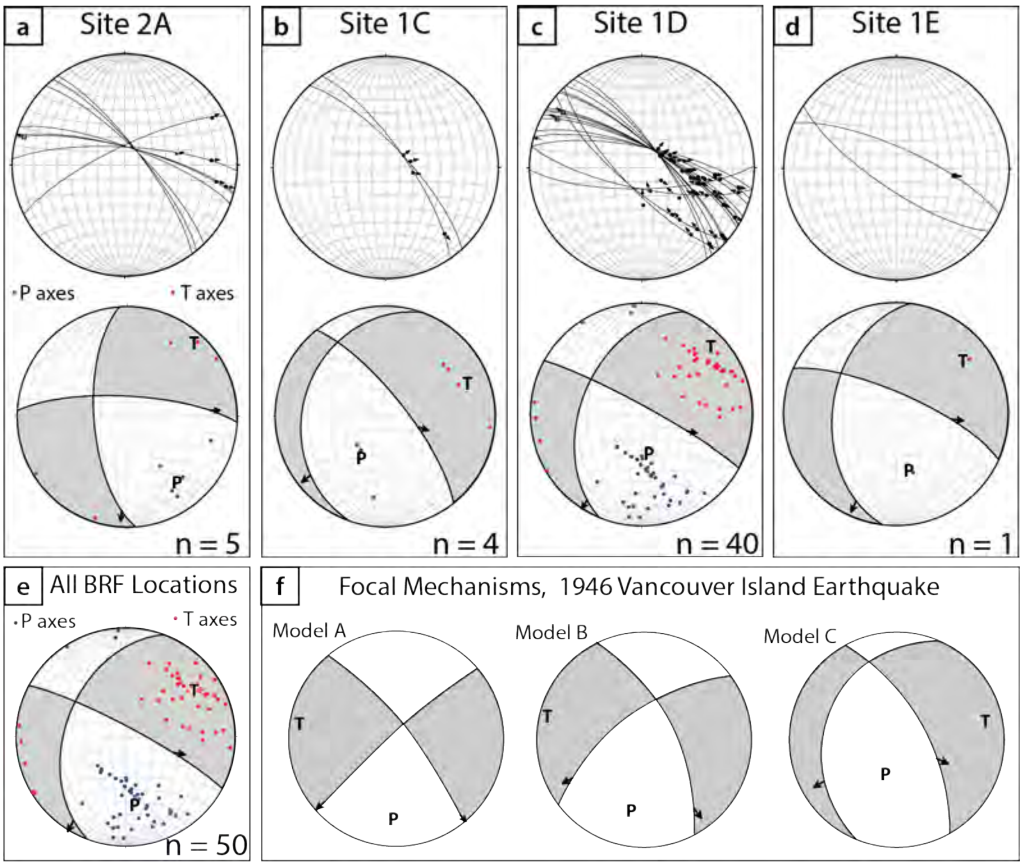

Figure 9. Right-lateral transtension along the Beaufort Range fault demonstrated by slip vectors and pseudo focal mechanisms produced from kinematic inversions. **A-D:** Kinematic data at four sub-sites along the BRF (see Figure 4 for locations). Upper panels: Lower hemisphere equal area projections showing fault planes, slip vectors, and hanging-wall motions. Lower panels: P- and T-axes and linked Bingham fault plane solutions (lower) for faults at locations 2A, 1C, 1D, and 1E. These slip vectors and kinematic inversions are consistent with right-lateral oblique motion on NE-dipping planes. **E:** Composite kinematic inversion for all surveyed sites along the BRF. Lower hemisphere equal area projection showing P- and T-axes and linked Bingham fault plane solutions. **F:** Focal mechanism solutions for the 1946 M 7.3 Vancouver Island earthquake (Rogers & Hasegawa, 1978, see Figure 2a for epicentrallocation). Model A is Rogers and Hasegawa's preferred model. Note the similarity in orientations of nodal planes and P- and T-axes for BRF fault kinematics.

inversion data are similar to full fault inversions, and indicate an approximate slip trend and plunge of ~110/45 along an ~80° NE dipping fault plane. These full-fault pseudo focal mechanisms yield local P- and T-axes with trends and plunges of 170/37 and 058/26 respectively.

4.3.2 Cumulative displacements

At Site 1, available exposures allowed us to calculate cumulative displacement across one to three strands for 14 interfluves developed in Qp1 and 9 channels incised into Qp1 (Figure 5). These data show that cumulative oblique slip at Site 1 measured in offset interfluves and channels ranges from ~4 to 21 m (Figure 6). At Site 2, cumulative displacement of channels incised into Qt was summed across two to four mapped strands showing cumulative slip magnitudes of ~4 to 13 m (Figure 6). We note that cumulative oblique slip magnitudes at Site 2 are likely underestimated, given that it was only possible to determine cumulative displacement across a portion of the mapped strands due to limited exposure and preservation.

Our calculated vertical and oblique displacement magnitudes show that older deposits typically record greater amounts of displacement than younger deposits. Examples of this relationship can be observed in the comparison of vertical separation along adjacent profiles at Sites 1 and 2 (Figure 10). At Site 1 (strand D, Figures 5, 10a) there is 5.8 m of vertical separation across an offset interfluve developed in Qp1, the oldest offset deposit at the site, whereas the adjacent, younger abandoned channel shows only 4.7 m of vertical separation. A younger Qft2 fluvial terrace, which crosses adjacent fault strand Ee, has even less vertical separation (2.3 m). Similarly, at Site 2, we find that the till-mantled hillslope typically has larger vertical separation than channels incised into till. For example, profile 28 at Site 2 in Qt shows 4.1 m of vertical separation across strand Q, whereas profile 33 along a younger channel incised into Qt shows only 2.9 m of vertical separation (Figures 6, 10b). Finally, we were able to expand this assessment of cumulative displacement to a set of 23 interfluves and channels at Site 1 for which we are able to reconstruct 3D displacement. These data show that older interfluves developed in Qp1 consistently have ~4 to 10 m more cumulative oblique displacement as compared to young channels incised into Qp1 (Figure 10c).

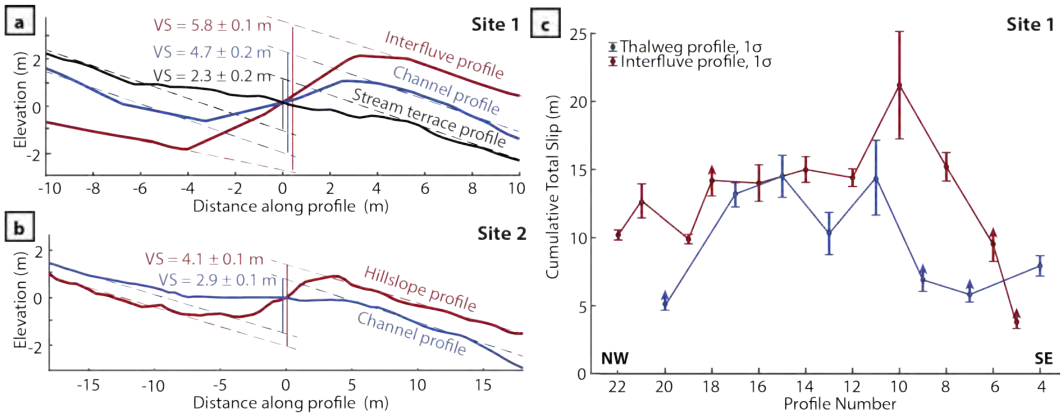

Figure 10. Topographic survey data showing differential magnitudes of fault offset in deposits of different ages. **A:** Example from Site 1D where there is the largest magnitude of vertical separation across an interfluve developed in Qp1 (profile 10, strand D), intermediate magnitudes across a channel incised into Qp1 (profile 11, strand D, channel age correlative to deposit Qp2), and minimum magnitudes across a Holocene stream terrace (profile 3, strand Ee). **B:** Example from Site 2A where there is greater vertical separation across the till mantled hillslope (profile 28, Qt,), and smaller separation across a channel incised into till (profile 33, strand Q). **C:** Cumulative slip estimates from Site 1D profiles: cumulative slip across interfluves (mean = 12.7 ± 4.4 m) is greater than for thalwegs (mean = 9.8 ± 3.9 m), suggesting interfluves have experienced at least one more event than thalwegs. Arrows indicate minimum slip estimates in locations where displacements across one or more strands could not be reconstructed.

5 Discussion

5.1 Characteristics of the Quaternary-active BRF

The field data and observations provided in this paper provide unequivocal evidence that the scarps we identify along the southwestern flank of the Beaufort Range are tectonic in origin and are associated with an active Beaufort Range fault. Mapped scarps form en echelon steps, and parallel arrays exhibit geometries common in strike-slip fault systems and pull-apart basins (e.g., Hatem et al., 2017; van Wijk et al., 2017), and occur along several tens of kilometers of strike length. The magnitudes of displacement and total fault lengths are consistent with observed displacement-length scaling relationships for active faults in Cascadia (R. H. Styron & Sherrod, 2021), and globally (D. L. Wells & Coppersmith, 1994; Wesnousky, 2008).

The scarps are inconsistent with formation processes associated with gravitational failure, glacial, or anthropogenic processes, for several reasons. First, scarps are predominantly uphill-facing, and are associated with steep NE-dipping fault planes that produce "valley-side up" displacement. This sense of displacement is opposite to that predicted for landslide-related failures. Second, the scarps are quasi-linear and extend for several km along strike, whereas headscarps associated with landslides tend to produce curvilinear and discontinuous scarps with limited strike lengths. Third, the mapped scarps are inconsistent with formation by sackungen (McCalpin et al., 1999), which typically form sets of parallel scarps at range crests, rather than the en echelon scarps we observe near the base of the range (e.g., Figure 2b as compared to Figure 3c). Finally, our field observations also confirm that these scarps are not associated with roads, logging tracks, or other anthropogenic disturbances, nor are they associated with glacial scouring or glacially-streamlined deposits (see Supplemental Text S1).

Our data indicate that the BRF consists of a set of high-angle faults, with an average 60-88° NE dip, with local fault strand strikes ranging from $\sim$270° to 320°. While individual fault strands extend for several hundred m to several km, these strands collectively define a discontinuous network of scarps that we interpret to be the surficial expression of a single fault zone at depth. Such discontinuous fault scarp networks are common in strike-slip systems, especially in immature faults with little cumulative offset (e.g., Hatem et al., 2017), and have been observed along other forearc faults in northern Cascadia (e.g., Morell et al., 2017). The mapped network of BRF fault scarps identified in this study extends for $\sim$40 km from Port Alberni to Comox Lake (Figure 2b and 1). Additional potential scarps visible in lidar DEMs occur along strike of the active BRF outside the map area, suggesting that the BRF may have a cumulative length that is >40 km (Figure 1). If all of the mapped scarps in this study are associated with a continuous subsurface fault network, then the BRF is one of the longest strike-length faults identified in northern Cascadia to date.

5.2 Kinematics of the BRF and relationship to inherited structures

Our field mapping and topographic survey data demonstrate that the active BRF is a transtensional structure that accommodates right-lateral oblique slip along a steeply NE-dipping fault zone (Figure 9). Three lines of evidence support this interpretation: 1) Field observations show consistent right-lateral offset of abandoned channels and interfluves and net NE-side-down vertical displacement. 2) Slip vectors resolved by reconstructing piercing lines similarly indicate NE-side-down hanging wall motion, consistent with right-lateral transtensional slip on a steeply NE dipping fault (Figure 9). These kinematics are consistent with mapped fault scarp geometries that suggest formation during right-lateral transtension. For example, at Site 1 (Figures 5a, 8), there is an en echelon array of faults with opposing dips that is consistent with the map patterns expected for a right-lateral transtensional negative flower structure. 3) Pseudo focal mechanism inversion of slip vectors indicate that the BRF accommodates right-lateral transtension along a steeply NE dipping fault plane.

The NE-side-down slip sense we determine for the Quaternary-active BRF produces a "range-side down" sense of motion. This result suggests that the high elevations and steep topography associated with the southwestern flank of the Beaufort Range were not formed by transtensional slip along the active BRF. Instead, the steep range front may be the product of differential erosion of the softer Cretaceous Nanaimo Gp sediments that underlie the Alberni Valley, relative to the more resistant Karmutsen Fm basalts that underlie the range crest (Muller & Carson, 1969). Or, this may imply that the net range-side-down (NE-side down) motion integrated over 100s kyr to Myr across the active BRF may be small relative to the amount of Eocene NE-side-up thrust fault displacement. The small cumulative magnitude of NE-side-down motion could indicate that transtension across the BRF is a relatively young phenomenon, and has not accrued a large magnitude of vertical displacement.

Finally, our data suggest that active BRF strands do not appear to directly reoccupy inherited thrust fault planes. The presence of active BRF scarps in both the hanging wall and footwall of inherited thrust faults (Figure 4) suggest that there is not a strong inherited lithologic or mechanical control on the position of the active BRF at the surface. Furthermore, there is an apparent difference between the near-surface dip of the Quaternary-active BRF (70-90°) and that of the inherited Eocene Beaufort Range thrust fault (∼45-70°). There are two possible explanations for this apparent dip discrepancy. First, these observations could imply that the subsurface projections of the active and Eocene faults may diverge at depth. Similar discrepancies between active and inherited fault geometries have been observed in the northern Cascadia forearc along the Leech River and North Olympic faults (Morell et al., 2017; G. Li et al., 2017; Nelson et al., 2017; Schermer et al., 2021). These data suggest that it is possible that the active BRF may reflect the formation of a new fault, more optimally oriented in the forearc stress field, rather than slip on an inherited bedrock structure. The second possibility is that the dip of the BRF is steep near the surface, but has a more gentle dip at depth, such that the active transtensional fault follows the Eocene thrust fault at depth. The geometry, kinematics, and slip history of the active BRF therefore provide critical insight into the neotectonic stress and strain fields in the northern Cascadia forearc.

5.3 Evidence for multiple surface-rupturing late Pleistocene to Holocene earthquakes

Our tectonogeomorphic mapping, topographic surveys of offset abandoned channels and interfluves, and field observations of fault scarp morphology support the hypothesis that the BRF has hosted multiple earthquakes since the deglaciation of the Alberni Valley (∼14-11 ka). The strongest evidence for multiple events comes from the differential scarp heights and cumulative slip magnitudes calculated for offset landforms of different ages at Sites 1 and 2 (Figure 10). At Site 1, interfluve crests developed in the older paraglacial unit Qp1 have greater vertical separation (∼1 m) and greater cumulative oblique slip (∼1-3 m) than abandoned channel thalwegs incised into that same unit. These abandoned channels in turn have greater vertical separation (∼2.4 m) than the displacement surveyed across a younger Qft2 fluvial terrace. The differential offset between interfluves, channels, and fluvial terraces indicates the occurrence of at least three events since the deposition of Qp1 at Site 1. At Site 2, differential scarp heights of ∼2 m between those developed in till-mantled hillslopes and younger channels incised into the hillslopes indicate at least two surface-rupturing events have occurred at this site following the deposition of Qt. Furthermore, if we make the simplifying assumption that a single event produces ∼1-3 m of oblique slip, based on the average difference in cumulative oblique displacement between interfluves and channels, these data suggest the BRF may have hosted more than three events since ∼11-14 ka.

At Site 1, we can place broad constraints on the relative timing of slip events by combining our estimates of deposit ages (Table 1; Figure 4c) with offset magnitudes (Table S2; Figure 6). The timing of the first event is constrained by the observation that older interfluves developed in Qp1 have more cumulative oblique offset than channels developed in Qp1. This observation indicates that at least one event must have occurred more recently than the deposition of Qp1, which occurred after deglaciation (∼11-14 ka), but before the abandonment of channels incised into Qp1. The timing of channel abandonment is not directly dated, but our correlation of channel incision to the deposition of Qp2 suggests channel abandonment occurred after the deposition of Qp2 (radiocarbon dated to ∼6 to 11 ka) and before the deposition of Qaf (radiocarbon dated to ∼3-6 ka). Therefore, the first event(s) likely occurred after ∼11-14 ka, but before ∼3-6 ka. The timing of the second event is constrained by the difference in offset between channels and inset Qft2 terraces. This difference requires one or more events to have occurred after channel abandonment (which we infer occurred after 6-11 ka), but before the formation of the Qft2 terrace (radiocarbon dated to <∼4 ka). The occurrence of a third event is supported by the ∼1.5 m of vertical offset of the Qft2 terrace. Therefore, the most recent event must have occurred after the deposition of the Qft2 terrace (since ∼4 ka).

These data suggest that the BRF has experienced at least three events over the late Pleistocene to late Holocene. The persistence of right-lateral transtensional deformation along the BRF for several thousand years after the retreat of glaciers from the Alberni Valley indicates that deformation cannot be attributed solely to changes in crustal loads and stresses due to glacial unloading and viscoelastic relaxation of the crust and mantle (e.g., Anderson et al., 1989; Craig et al., 2016; Davenport et al., 1989; Lagerbäck, 1990; Mörner, 1991; Muir-Wood, 2000; Jarman & Ballantyne, 2002; van Loon et al., 2016). Such “glacially-induced” earthquakes typically occur during or within a few kyr of glacial retreat, when changes in ice loads and crustal stresses from the viscoelastic rebound are greatest (Steffen et al., 2014). While our data do not constrain the precise timing of the first event(s), and cannot rule out that early events on the BRF were impacted by glacial unloading, they do indicate earthquakes have occurred in the middle to late Holocene, well after the largest stress changes due to glacial loading would have occurred. Additionally, we note that glacial unloading typically reduces vertical stress, and given that our slip data indicate the BRF accommodates transtension, such unloading would reduce the deviatoric stress making failure less likely. Overall, the persistence of right-lateral transtensional events throughout the Holocene suggests that tectonic forces are the principal drivers of deformation, and any glacial impacts are secondary.

Our estimates of displacement per event, and measurements of the total length of the active BRF from mapped or inferred fault scarps, allow us to estimate the magnitude of paleo-earthquakes at these sites using displacement scaling relationships. An estimated ~1-3 m of displacement per event suggests that the BRF could have hosted M_W 6.9 to 7.2 events (D. L. Wells & Coppersmith, 1994). These magnitudes are similar to those determined based on our total mapped fault length of 35 to >40 km, which suggests M_W 6.8 to >7.0 events (D. L. Wells & Coppersmith, 1994; Wesnousky, 2008). These earthquake magnitudes are similar in scale to the M 7.3 magnitude calculated for the 1946 Vancouver Island earthquake, which caused significant damage, including to telephone wires, underwater telegraph cables, and the hospital in Port Alberni, BC (Hodgson, 1946). An earthquake of a similar magnitude today would pose significant hazard not only to Port Alberni, but also to the nearby communities of Nanaimo, Parksville, Qualicum Beach, and Courtenay (Figure 2a). Failure of dams on Comox Lake and Elsie Lake could lead to flooding of communities downstream (Figure 2b), as well as impacts on power availability, as nearby power stations supply 11% of the electricity generated on Vancouver Island (BC Hydro, n.d.).

5.4 Estimate of Late Pleistocene to Holocene slip rates

Estimation of fault slip rates yields important information relevant to understanding how strain is partitioned among faults, and they represent primary data used in seismic hazard analyses (Morell et al., 2020). Ideally, slip rates are calculated when at least two precise earthquake ages and the displacement associated with the bracketed event are known (e.g., a closed interval slip rate, DuRoss et al., 2020) and estimated over a time period spanning more than 5 earthquakes (R. Styron, 2019). In the absence of precise earthquake ages, a geomorphic slip rate can be estimated that affords an estimate of the slip rate that has accrued since the development of the geomorphic feature, using estimates of the date of the landform and displacement data recorded in the geomorphic feature. However, such an open-interval slip rate can be biased because the age of the geomorphic feature can differ from the age of the earthquake that deformed the feature.

On the BRF, we currently do not have precise earthquake ages, and we do not know the displacement between earthquakes with precision. However, we nonetheless make broad estimates of slip rate based on the known ages and displacements between known events. The cumulative displacement of different deposits, their depositional ages, and our estimates of event timing, place bounds on fault slip rates for the active BRF. Both open-ended and closed interval approaches at Site 1 yield slip rates for the BRF that range from ∼0.5 to ∼2 mm/yr. The open-ended approach yields a rate of ∼0.7-1.3 mm/yr, based on the ∼10 to 15 m of cumulative oblique slip across all mapped fault strands and an estimated deglaciation age of ∼11.5-13.6 ka. There is only one reliable closed interval calculation that can be made given the available offset data and uncertainties in event timing. This interval calculation uses the ∼8-9 m cumulative displacement of the channels at Site 1, and the difference in age between the Qft2 terrace and the interfluves at Site 1, which could range from ∼3.5 to 13.6 kyr. This closed interval spans at least two events, and yields a slip rate estimate of 0.6-2.6 mm/yr. Given the uncertainties in the ages of events and displacement magnitudes in this closed interval calculation, we prefer the more conservative open-ended rate of 0.7-1.3 mm/yr.

These data demonstrate that, even at the lower bound of uncertainty, the Beaufort Range fault is one of the fastest-slipping Quaternary faults in the northern Cascadia forearc. Our slip rate estimates of ∼0.5 to ∼2 mm/yr indicate that the BRF has a higher slip rate than the nearby LRF (0.2-0.3 mm/yr; Morell et al., 2017, 2018) and Darrington-Devils Mountain fault zone DMF (0.14 ± 0.1 mm/yr; Personius et al., 2014), and a similar slip rate to the NOFZ (1.3-2.3 mm/yr, 3-5 post-glacial earthquakes; Schermer et al., 2021). These data suggest that the BRF is a major crustal structure that accommodates permanent deformation in the northern Cascadia forearc.

5.5 Comparison of the 1946 Vancouver Island earthquake kinematics with slip on the BRF

The field data reported here cannot constrain the timing of the most recent event along the active BRF beyond that it occurred after ∼3.5 ka, and therefore cannot directly test whether the 1946 event ruptured along the BRF within our field area. However, our data from the Holocene BRF share striking similarities to the kinematics, spatial distribution, and fault plane solutions for the 1946 event.

The pseudo-focal mechanism solutions for the BRF determined from kinematic inversions of fault slip have similar slip planes, slip vectors, and P- and T-axes as those determined for the 1946 Vancouver Island earthquake (Figure 9). Focal mechanism solutions for the 1946 earthquake (Rogers & Hasegawa, 1978) have NW-SE striking nodal planes with strikes of 319-332° and dips of 66-79°, and SW-NE striking nodal planes with strikes of 222-233° and dips of 36-85° (Figure 9f, Table S3). These nodal plane attitudes are strikingly similar to the nodal planes of the pseudo-focal mechanisms solutions derived from fault slip vectors along the active BRF (Figure 9). The NW-SE nodal plane of the focal mechanism preferred by Rogers and Hasegawa (1978) of 319/79 NE is subparallel to our calculated attitude of the active BRF of ∼270-320/∼75, and the predicted slip vectors associated with the NW-SE striking nodal planes for the 1946 earthquake have trends ranging from 114 to 143°, and plunges ranging from 05° to 55°—similar slip vector orientations to those determined from offset piercing lines along the active BRF. Finally, the stress axes determined for the 1946 focal mechanism solutions have moderately plunging, southerly trending P-axes and sub-horizontal T-axes with trends similar to those determined for the active BRF (Figure 9).

The fault slip vectors and transtensional pseudo-focal mechanisms that we determine for the BRF are also similar to fault plane inversions based on geodetic motions associated with the 1946 earthquake (Slawson & Savage, 1979). Repeat surveys of topographic benchmarks across the Beaufort Range at the latitude of the earthquake epicenter (∼49.45° N) suggest right-lateral oblique slip on a steeply (70°) NE-dipping fault plane that extended for 60 km along strike (Slawson & Savage, 1979). Our mapped Sites 1 and 2 along the BRF therefore lie within the modeled event rupture area, and the fault plane dip is similar to the 60-88° NE dip we determine for the BRF. In addition, slip inversions for the 1946 event fault planes indicate the crustal displacements are best reproduced by ∼1 m of right-lateral and ∼2 m dip slip, along 60 km fault length parallel to the BRF. Therefore, both the relative ratio of strike slip to dip slip (∼0.5:1) and the estimated slip per event (∼1-2 m) modeled for the 1946 event are similar to our slip ratios of 0.3-1.5:1 (strike slip to dip slip) and estimates of ∼1-3 m of oblique slip per BRF event.

These data collectively indicate that the Holocene slip observed along the active BRF is kinematically and spatially compatible with the slip inferred for the 1946 Vancouver Island earthquake. These correlations suggest that, if the 1946 event failed along a NW-SE striking, steeply NE-dipping plane, as suggested by Rogers and Hasegawa (1978) and Slawson and Savage (1979), the BRF is a likely candidate for hosting this event. Our estimated age of the most recent event of <3-4 ka allows for this possibility. Furthermore, our field offset data provide evidence that the active BRF has hosted at least 3 earthquakes since the late Pleistocene, each with slip that is compatible with that modelled for the NW-SE striking nodal plane for the 1946 event. These observations suggest then that the BRF hosted multiple 1946-like events over the late Pleistocene to Holocene.

5.6 Implications for forearc strain accommodation

These results have several key implications for the long-term permanent strain accumulation in the northern Cascadia forearc. First, our field data and kinematic inversions for the active BRF indicate that this portion of the Cascadia forearc has experienced right-lateral transtension over the past ∼11-14 ka. In addition, the similarity between the fault kinematics integrated over multiple paleoseismic events spanning the late Pleistocene to Holocene and the 1946 Vancouver Island earthquake suggests that these transtensional kinematics are representative of the local upper plate deformation field over decadal to millennial time scales. If true, these time scales would span multiple upper plate fault seismic cycles, which likely have recurrence intervals of 1000s of years (e.g., Morell et al., 2018; Schermer et al., 2021), and multiple subduction interface megathrust seismic cycles, which have recurrence periods of ∼390-540 years (e.g., Walton et al., 2021).

Second, the slip kinematic inversions for the active BRF suggest that the P- and T-axes inverted for long-term (late-Pleistocene to present) slip are consistent with regional stress patterns derived from historical seismicity (Figure 2a; Balfour et al., 2011). We find that the trends and plunges of P- and T-axes determined for the BRF are within ∼20-40° of the P- and T-axes determined for the 1946 Vancouver Island earthquake and from inversions determined from nearby upper plate seismicity (Balfour et al., 2011). Several studies have suggested that variations in trench-perpendicular tractions during the megathrust seismic cycle can cause inversions in principal stress orientations in the overriding plate, such that forearc fault slip sense can vary as a function of the megathrust seismic cycle (e.g., Wang et al., 1995; Loveless et al., 2010; Regalla et al., 2017). However, the consistency of P- and T-axes determined from historical earthquakes and from paleoseismic slip suggests that BRF kinematics have not changed drastically over Holocene time scales. These data suggest that there is some level of consistency in the deformation field associated with short-term (decadal) upper plate seismicity and long-term (kyr-scale) fault slip, and a potentially similar temporal consistency in the upper plate stress field.

Third, a comparison between these BRF fault kinematics to those determined for other active faults in the northern Cascadia forearc, suggests that there may be a spatial transition from a forearc deformation field promoting right-lateral transpression near the Olympic Mountains and on southernmost Vancouver Island, to one promoting right-lateral transtension in the northern Cascadia forearc on central Vancouver Island. Specifically, the North Olympic fault zone, the Darrington-Devils Mountain fault, the Southern Whidbey Island fault, the Leech River fault, and the XEOLXELE~~K~~-Elk lake fault appear to be accommodating right-lateral slip and compression, as determined by earthquake focal mechanisms and paleoseismic data (Sherrod et al., 2008; Personius et al., 2014; Schermer et al., 2021; Morell et al., 2018; Harrichhausen et al., 2021, 2023). In contrast, at the latitude of central Vancouver Island, the BRF appears to be accommodating right-lateral transtension, as determined by kinematic inversions of offset geomorphic piercing lines across the BRF.

This observation suggests that there may be a change in the upper plate strain field from one favoring transpression on faults near the Olympic Mountains to one favoring transtension on faults in northern Cascadia, around the latitude of 48.5-49° N. This change in strain field may be related to spatial variations in principal stress orientations and magnitudes in the upper plate that locally promote transtension along the BRF. While the data presented here are not sufficient to determine the causes of this potential change in the upper plate deformation field, there are several possibilities, including oroclinal bending (Johnston & Acton, 2003; Finley et al., 2019; Harrichhausen et al., 2021), spatial changes in plate tractions, convergence rate, or obliquity (R. E. Wells et al., 1998;

Wang, 2000; McCaffrey et al., 2013; S. Li et al., 2018), or the 'escape' of forearc crustal blocks related to north-directed shear from southern Cascadia (Nelson et al., 2017). The consistency of fault kinematics and P- and T-axes calculated near the BRF from both seismic and paleoseismic data suggest that a deformation field favoring local right-lateral transtension has persisted over both decadal and millennial timescales.

6 Conclusions

We provide the first geologic field evidence that the Beaufort Range fault is a seismogenic fault, and demonstrate that it actively accommodates right-lateral transtension within the northern Cascadia forearc of central Vancouver Island. Field mapping and topographic surveys document >35-40 km of northwest-striking, primarily northeast-dipping fault strands along the southwestern flank of the Beaufort Range. These scarps occur in discontinuous, en echelon and parallel sets and offset late Pleistocene to Holocene glacial, paraglacial, and post-glacial deposits. We observe an increase in scarp height and total offset with increasing unit age that provides evidence for at least three surface-rupturing earthquakes on the BRF since ∼13.6-11 ka, the most recent of which occurred in the past ∼3-4 kyr. Slip magnitudes reconstructed from offset piercing lines, total fault length, and the ages of offset deposits suggest that the BRF is capable of hosting earthquakes of M_W 6.5-7.5, and has a late Pleistocene to Holocene slip rate of 0.5 to 2 mm/yr. Thus the BRF is a major forearc fault accommodating deformation in the northern Cascadia subduction zone, and poses significant hazard to communities and infrastructure on Vancouver Island.

Notably, kinematic slip inversions of geomorphic piercing lines offset by the BRF yield transtensional pseudo-focal mechanisms, fault geometries, slip vectors, and P- and T-axes that are remarkably similar to those determined for the 1946 Vancouver Island earthquake. These data suggest that the BRF is a candidate structure to have hosted this event. The consistency of right-lateral transtensional slip kinematics between the 1946 earthquake and late Pleistocene to Holocene slip on the BRF suggests that this portion of the northern Cascadia forearc has accommodated regional transtension over decadal to millennial time scales, spanning multiple earthquake cycles.

7 Open Research

New data produced in this study:

Data collected and analyzed in this manuscript are available in a Dryad Data Repository (Lynch et al., 2023) at
`https://datadryad.org/stash/share/Ui8KejoZgz41xslOZUxfCQV2Nea3JsVwQoTz9DZ1iho`.
The repository contains the following data:

1. Text files containing raw field data (x,y,elevation) of surveyed offset landforms
2. Text files containing raw field data (x,y,elevation) of fault midpoint locations
3. R script for calculating 3D fault plane geometry
4. R script for calculating 3D offsets of linear piercing lines across a dipping fault

Previously published data and programs used in this study:

1. The USGS Quaternary faults and folds database used for Figure 1 is available at `https://www.usgs.gov/programs/earthquake-hazards/faults`.
2. The BC Geological Survey (BCGS) bedrock geology map used for Figures 2a, 4, and Figure 1 is available at `https://www2.gov.bc.ca/gov/content/industry/mineral-exploration-mining/british-columbia-geological-survey/geology/bcdigitalgeology`.
3. The OxCal program v. 4.4 by C. Bronk Ramsey used for radiocarbon calibration is available at `https://c14.arch.ox.ac.uk/oxcal/OxCal.html`.
4. The R. Allmendinger FaultKin 7.6 program used for plotting and analyzing fault plane and slip vector data in Figure 9 is available at `http://www.geo.cornell.edu/geology/faculty/RWA/programs/faultkin.html`.
5. The OSX Stereonet 9.9.4 program used for plotting bedrock fault planes and slickenlines in Figure 7 is available at `http://www.geo.cornell.edu/geology/faculty/RWA/programs/stereonet.html`.

Acknowledgments

This work was conducted on the traditional territory of the Hupačasatḥ, K'ómoks, and ćišaaʔatḥ people, and we acknowledge their historical relationships with the land that continue to this day. Funding for this project was supported by NSF EAR Tectonics 1756834/2004684 to Regalla and 1756943 to Morell, by the Boston University Department of Earth and Environmental Sciences, and the Northern Arizona University Duebendorfer-Barnes Structure Endowment. We would like to thank Todd Thompson, TimberWest, and Island Timberlands for land access, and Mosaic/Island Timberlands/TimberWest for pro-viding lidar ground return data, as well as Edwin Nissen and the University of Victoria School of Earth and Ocean Sciences for discussion of local tectonics and help with field logistics. We would also like to acknowledge the late Vic Levson for help with understanding glacial systems of Vancouver Island, and Johanna Fischi and Tatum McLeod for assistance in the field.

References

AGI. (2003). *Global GIS: Volcanoes of the world.* https://earthworks.stanford.edu/catalog/harvard-glb-volc.

Alley, N. F., & Chatwin, S. C. (1979). Late Pleistocene history and geomorphology, southwestern Vancouver Island, British Columbia. *Canadian Journal of Earth Sciences*, *16*(9), 1645–1657.

Allmendinger, R. W., Cardozo, N., & Fisher, D. M. (2012). *Structural geology algorithms: Vectors and tensors in structural geology.* Cambridge University Press.

Anderson, W. A., Borns, H. W., Kelley, J. T., & Thompson, W. B. (1989). Neotectonic Activity in Coastal Maine. *Maine Geological Survey*, 195–212.

Angelier, J., & Mechler, P. (1977, January). Sur une methode graphique de recherche des contraintes principales egalement utilisables en tectonique et en seismologie : La methode des diedres droits. *Bulletin de la Société Géologique de France*, *S7-XIX*(6), 1309–1318.

Balfour, N. J., Cassidy, J. F., Dosso, S. E., & Mazzotti, S. (2011). Mapping crustal stress and strain in southwest British Columbia. *Journal of Geophysical Research: Solid Earth*, *116*(3), 1–11.

Ballantyne, C. K. (2002). A general model of paraglacial landscape response. *The Holocene*, *12*, 371–376.

Ballantyne, C. K., & Benn, D. I. (1996). Paraglacial slope adjustment during recent deglaciation and its implications for slope evolution in formerly glaciated environments. In *Advances in Hillslope Processes* (Vol. 2, pp. 1173–1195).

BC Hydro. (n.d.). *Our facilities: Vancouver Island.* https://www.bchydro.com/energy-in-bc/operations/our-facilities/vancouver-island.html.

Blaise, B., Clague, J. J., & Mathewes, R. W. (1990, November). Time of Maximum Late Wisconsin Glaciation, West Coast of Canada. *Quaternary Research*, *34*(3), 282–295.

Brocher, T. M., Parsons, T., Blakely, R. J., Christensen, N. I., Fisher, M. A., & Wells, R. E. (2001). Upper crustal structure in Puget Lowland, Washington: Results from the 1998 Seismic Hazards Investigation in Puget Sound. *Journal of Geophysical Research: Solid Earth*, *106*(B7), 13541–13564.

Brodzikowski, K., & van Loon, A. J. (1987). A systematic classification of glacial and periglacial environments, facies and deposits. *Earth Science Reviews*, *24*(5), 297–381.

Bronk Ramsey, C. (1995). Radiocarbon Calibration and Analysis of Stratigraphy: The OxCal Program. *Radiocarbon*, *37*(2), 425–430.

Bronk Ramsey, C. (2021). *OxCal Program, Version 4.4.* Oxford Radiocarbon Accelerator Unit, University of Oxford.

Clague, J. J. (1980). Late Quaternary geology and geochronology of British Columbia: Part 1: Radiocarbon dates. *Geological Survey of Canada Paper*, *80–13*.

Clague, J. J. (1994). Quaternary stratigraphy and history of south-coastal British Columbia. *Geological Survey of Canada Bulletin*, *481*, 181–192.

Clague, J. J. (1996). Paleoseismology and seismic hazards, southwestern British Columbia. *Geological Survey of Canada Bulletin*, *494*.

Clague, J. J., & James, T. S. (2002). History and isostatic effects of the last ice sheet in southern British Columbia. *Quaternary Science Reviews*, *21*, 71–87.

Clowes, R. M., Yorath, C. J., & Hyndman, R. D. (1987). Reflection mapping across the convergent margin of western Canada. *Geophysical Journal of the Royal Astronomical Society*, *89*(1), 79–84.

Craig, T. J., Calais, E., Fleitout, L., Bollinger, L., & Scotti, O. (2016). Evidence for the release of long-term tectonic strain stored in continental interiors through intraplate earthquakes. *Geophysical Research Letters*, *43*(13), 6826–6836.

Cui, Y., Miller, D., Schiarizza, P., & Diakow, L. (2017). *British Columbia digital geology* (Tech. Rep. No. 2017-8). British Columbia Ministry of Energy, Mines and Petroleum Resources.

Davenport, C., Ringrose, P., Becker, A., Hancock, P., & Fenton, C. (1989). Geological Investigations of Late and Post Glacial Earthquake Activity in Scotland. In S. Gregersen & P. Basham (Eds.), *Earthquakes at North-Atlantic Passive Mar-*

gins: Neotectoncis and Postglacial Rebound (pp. 175–194). Kluwer Academic Publishers.

Delano, J. E., Amos, C. B., Loveless, J. P., Rittenour, T. M., Sherrod, B. L., & Lynch, E. M. (2017). Influence of the megathrust earthquake cycle on upper-plate deformation in the Cascadia forearc of Washington State, USA. *Geology*, *45*(11), 1051–1054.

DuRoss, C. B., Gold, R. D., Briggs, R. W., Delano, J. E., Ostenaa, D. A., Zellman, M. S., ... Mahan, S. A. (2020, July). Holocene earthquake history and slip rate of the southern Teton fault, Wyoming, USA. *GSA Bulletin*, *132*(7-8), 1566–1586.

Easterbrook, D. J. (1992). Advance and retreat of Cordilleran ice sheets in Washington, U.S.A. *Géographie Physique et Quaternaire*, *46*(October), 51–68.

England, T., & Calon, T. J. (1991). The Cowichan fold and thrust system, Vancouver Island, southwestern British Columbia. *Geological Society of America Bulletin*, *103*(3), 336–362.

England, T. D. J. (1990). *Late Cretaceous to Paleogene evolution of the Georgia Basin, southwestern British Columbia* (Unpublished doctoral dissertation). University of British Columbia.

England, T. D. J., Currie, L. D., Massey, N. W., Roden-Tice, M. K., & Miller, D. S. (1997). Apatite fission-track dating of the Cowichan fold and thrust system, southern Vancouver Island, British Columbia. *Canadian Journal of Earth Sciences*, *34*(5), 635–645.

Eyles, N., Boyce, J. I., & Barendregt, R. W. (1999, February). Hummocky moraine: Sedimentary record of stagnant Laurentide Ice Sheet lobes resting on soft beds. *Sedimentary Geology*, *123*(3-4), 163–174.

Finley, T., Morell, K. D., Leonard, L., Regalla, C., Johnston, S. T., & Zhang, W. (2019). Ongoing oroclinal bending on the Cascadia forearc margin and its relation to concave-outboard plate margin geometry. *Geology*, *47*(2), 155–158.

Fyles, J. G. (1963). Surficial geology of Horne Lake and Parksville map-areas, Vancouver Island, British Columbia. *Geological Survey of Canada Memoir*, *318*, 142.

Geological Survey, U. (n.d.). *Quaternary fault and fold database for the United States.*

Goldfinger, C., Kulm, L. D., Yeats, R. S., Appelgate, B., Mackay, M. E., & Moore, G. F. (1992). Transverse structural trends along the Oregon convergent margin: Implications for Cascadia earthquake potential and crustal rotations. *Geology*, *20*(2), 141–144.

Graham, A. (2017). *Geometry, kinematics, and Quaternary activity of the Leech River fault zone, southern Vancouver Island, British Columbia, Canada* (MSc Thesis). University of Victoria.

Halsted, E. C. (1968). The Cowichan Ice tongue, Vancouver Island. *Canadian Journal of Earth Sciences*, *5*, 1409–1415.

Harrichhausen, N., Finley, T., Morell, K. D., Regalla, C. A., Bennett, S. E. K., Leonard, L. J., ... Sethanant, I. (2023). Paleoseismic study of the XEOLX-ELEK–Elk Lake fault: A newly identified Holocene fault in the northern Cascadia forearc near Victoria, British Columbia, Canada. In *11th International INQUA Meeting on Paleoseismology, Active Tectonics and Archeoseismology* (Vols. 90–93, p. 4). France.

Harrichhausen, N., Morell, K. D., Regalla, C., Bennett, S. E. K., Leonard, L. J., Lynch, E. M., & Nissen, E. (2021, April). Paleoseismic Trenching Reveals Late Quaternary Kinematics of the Leech River Fault: Implications for Forearc Strain Accumulation in Northern Cascadia. *Bulletin of the Seismological Society of America*, *111*(2), 1110–1138.

Hatem, A. E., Cooke, M. L., & Toeneboehn, K. (2017). Strain localization and evolving kinematic efficiency of initiating strike-slip faults within wet kaolin experiments. *Journal of Structural Geology*, *101*, 96–108.

Hayes, G. P., Moore, G. L., Portner, D. E., Hearne, M., Flamme, H., Furtney, M., & Smoczyk, G. M. (2018). Slab2, a comprehensive subduction zone geometry model. *Science*, *362*(October), 58–61.

Herman, M. W., & Govers, R. (2020). Stress evolution during the megathrust earthquake cycle and its role in triggering extensional deformation in subduction zones. *Earth and Planetary Science Letters*, *544*.

Hodgson, E. (1946). British Columbia Earthquake June 23rd, 1946. *The Journal of The Royal Astronomical Society of Canada*, *40*(8), 285–319.

Horst, A. E., Streig, A. R., Wells, R. E., & Bershaw, J. (2021). Multiple Holocene earthquakes on the Gales Creek fault, northwest Oregon fore-arc. *Bulletin of* *the Seismological Society of America*, *111*(1), 476–489.

Huang, M.-H., Morell, K. D., Duvall, A., Gallen, S. F., & Hilley, G. E. (2022). *Exploring Subduction Zone Geohazards on Land and at Sea.* http://eos.org/features/exploring-subduction-zone-geohazards-on-land-and-at-sea.

Jarman, D., & Ballantyne, C. K. (2002, March). Beinn Fhada, Kintail: An Example of Large-scale Paraglacial Rock Slope Deformation. *Scottish Geographical Journal*, *118*(1), 59.

Johnston, S. T., & Acton, S. (2003). The Eocene Southern Vancouver Island Orocline-a response to seamount accretion and the cause of fold-and-thrust belt and extensional basin formation. *Tectonophysics*, *365*(1-4), 165–183.

Kelsey, H. M., Sherrod, B. L., Nelson, A. R., & Brocher, T. M. (2008). Earthquakes generated from bedding plane-parallel reverse faults above an active wedge thrust, Seattle fault zone. *Bulletin of the Geological Society of America*, *120*(11-12), 1581–1597.

Kreemer, C., Blewitt, G., & Klein, E. C. (2014, August). A geodetic plate motion and Global Strain Rate Model. *Geochemistry, Geophysics, Geosystems*, *15*(10), 3849–3889.

Lagerbäck, R. (1990, December). Late Quaternary faulting and-paleoseismicity in northern Fennoscandia, with particular reference to the Lansjärv area, northern Sweden. *Geologiska Föreningen i Stockholm Förhandlingar*, *112*(4), 333–354.

Lamontagne, M., Halchuk, S., Cassidy, J. F., & Rogers, G. C. (2018). *Significant Canadian earthquakes 1600-2017* (Tech. Rep. No. 8285).

Lane, E. (1947). Report of the subcommittee on sediment terminology. *Transactions, American Geophysical Union*, *28*, 936-938.

Li, G., Liu, Y., Regalla, C., & Morell, K. D. (2017). Seismicity relocation and fault structure near the Leech River Fault Zone, southern Vancouver Island. , 4–8.

Li, S., Wang, K., Wang, Y., Jiang, Y., & Dosso, S. E. (2018). Geodetically Inferred Locking State of the Cascadia Megathrust Based on a Viscoelastic Earth Model. *Journal of Geophysical Research: Solid Earth*, *123*(9), 8056–8072.

Li, Z., Bruhn, R. L., Pavlis, T. L., Vorkink, M., & Zeng, Z. (2010). Origin of sackung uphill-facing scarps in the Saint Elias orogen, Alaska: LIDAR data vi-sualization and stress modeling. *Bulletin of the Geological Society of America*, *122*(9-10), 1585–1589.

Liberty, L. M., Hemphill-Haley, M. A., & Madin, I. P. (2003, June). The Portland Hills Fault: Uncovering a hidden fault in Portland, Oregon using high-resolution geophysical methods. *Tectonophysics*, *368*(1-4), 89–103.

Loveless, J. P., Allmendinger, R. W., Pritchard, M. E., & González, G. (2010). Normal and reverse faulting driven by the subduction zone earthquake cycle in the northern Chilean fore arc. *Tectonics*, *29*(2), 1–16.

Lynch, E. M., Regalla, C., Morell, K. D., Harrichhausen, N., & Leonard, L. J. (2023). *Three-dimensional offsets of geomorphic piercing lines displaced by the Quaternary-active Beaufort Range fault, northern Cascadia forearc, BC, Canada* [Data set].

Marrett, R., & Allmendinger, R. W. (1990). Kinematic analysis of fault-slip data. *Journal of Structural Geology*, *12*, 973–986.

Mathews, W. H. (1979). Landslides of central Vancouver Island and the 1946 earthquake. *Bulletin of the Seismological Society of America*, *69*(2), 445–450.

Mazzotti, S., Leonard, L. J., Cassidy, J. F., Rogers, G. C., & Halchuk, S. (2011). Seismic hazard in western Canada from GPS strain rates versus earthquake catalog. *Journal of Geophysical Research: Solid Earth*, *116*(B12).

McCaffrey, R., King, R. W., Payne, S. J., & Lancaster, M. (2013). Active tectonics of northwestern U.S. inferred from GPS-derived surface velocities. *Journal of Geophysical Research: Solid Earth*, *118*(2), 709–723.

McCalpin, J. P., Consulting, G.-H., & Box, P. O. (1999). Criteria for Determining the Seismic Significance of Sackungen and Other Scarplike Landforms in Mountainous Regions.

Morell, K. D., Regalla, C., Amos, C. B., Bennett, S. E., Leonard, L. J., Graham, A., … Telka, A. (2018). Holocene Surface Rupture History of an Active Forearc Fault Redefines Seismic Hazard in Southwestern British Columbia, Canada. *Geophysical Research Letters*, *45*(21), 11,605–11,611.

Morell, K. D., Regalla, C., Leonard, L. J., Amos, C. B., & Levson, V. (2017). Quaternary Rupture of a Crustal Fault beneath Victoria, British Columbia, Canada. *GSA Today*, *27*(3-4), 4–10.

Morell, K. D., Styron, R., Stirling, M., Griffin, J., Archuleta, R., & Onur, T. (2020).

Seismic Hazard Analyses From Geologic and Geomorphic Data: Current and Future Challenges. *Tectonics*, *39*(10), e2018TC005365.

Mörner, N.-A. (1991, March). Intense earthquakes and seismotectonics as a function of glacial isostasy. *Tectonophysics*, *188*(3), 407–410.

Mosher, D. C., & Hewitt, A. T. (2004). Late Quaternary deglaciation and sea-level history of eastern Juan de Fuca Strait, Cascadia. *Quaternary International*, *121*(1), 23–39.

Muir-Wood, R. (2000, October). Deglaciation Seismotectonics: A principal influence on intraplate seismogenesis at high latitudes. *Quaternary Science Reviews*, *19*(14), 1399–1411.

Muller, J. E., & Carson, D. J. T. (1969). Geology and Mineral Deposits of Alberni map area, British Columbia (92F). *Geological Survey of Canada Paper*.

Nelson, A. R., Personius, S. F., Wells, R. E., Schermer, E. R., Bradley, L. A., Buck, J., & Reitman, N. (2017). Holocene earthquakes of magnitude 7 during westward escape of the Olympic Mountains, Washington. *Bulletin of the Seismological Society of America*, *107*(5), 2394–2415.

Personius, S. F., Briggs, R. W., Nelson, A. R., Schermer, E. R., Zebulon Maharrey, J., Sherrod, B. L., … Bradley, L. A. (2014). Holocene earthquakes and right-lateral slip on the left-lateral Darrington-Devils Mountain fault zone, northern Puget Sound, Washington. *Geosphere*, *10*(6), 1482–1500.

Personius, S. F., Dart, R. L., Bradley, L. A., & Haller, K. M. (2003). Map and data for Quaternary faults and folds in Oregon. *US Geological Survey Open-File Report*, *03–095*, 1–550.

Regalla, C., Fisher, D. M., Kirby, E., Oakley, D., & Taylor, S. (2017). Slip Inversion Along Inner Fore-Arc Faults, Eastern Tohoku, Japan. *Tectonics*, *36*(11), 2647–2668.

Regalla, C., Kirby, E., Mahan, S. A., McDonald, E., Pangrcic, H., Binkley, A., … Lynch, E. M. (2022). Late Holocene rupture history of the Ash Hill fault, Eastern California Shear Zone, and the potential for seismogenic strain transfer between nearby faults.pdf. *Earth Surface Processes and Landforms*, *47*, 2897–2925.

Reimer, P. J., Austin, W. E., Bard, E., Bayliss, A., Blackwell, P. G., Bronk Ramsey, C., … Talamo, S. (2020). The IntCal20 Northern Hemisphere Radiocarbon

Age Calibration Curve (0-55 cal kBP). *Radiocarbon*, *62*(4), 725–757.

Riller, U., Clark, M. D., Daxberger, H., Doman, D., Lenauer, I., Plath, S., & Santimano, T. (2017, August). Fault-slip inversions: Their importance in terms of strain, heterogeneity, and kinematics of brittle deformation. *Journal of Structural Geology*, *101*, 80–95.

Rogers, G. C. (1979, March). Earthquake fault plane solutions near Vancouver Island. *Canadian Journal of Earth Sciences*, *16*(3), 523–531.

Rogers, G. C., & Hasegawa, H. S. (1978). A second look at the British Columbia earthquake of June 23, 1946. *Bulletin of the Seismological Society of America*, *68*(3), 653–676.

Ryder, J. M. (1971, February). The Stratigraphy and Morphology of Para-glacial Alluvial Fans in South-central British Columbia. *Canadian Journal of Earth Sciences*, *8*(2), 279–298.

Scharer, K., Salisbury, J., Arrowsmith, R., & Rockwell, T. (2014, January). Southern San Andreas Fault Evaluation Field Activity: Approaches to Measuring Small Geomorphic Offsets–Challenges and Recommendations for Active Fault Studies. *Seismological Research Letters*, *85*, 68–76.

Schermer, E. R., Amos, C. B., Duckworth, W. C., Nelson, A. R., Angster, S., Delano, J., & Sherrod, B. L. (2021). Postglacial mw 7.0–7.5 earthquakes on the north olympic fault zone, Washington. *Bulletin of the Seismological Society of America*, *111*(1), 490–513.

Sherrod, B. L., Blakely, R. J., Weaver, C. S., Kelsey, H. M., Barnett, E., Liberty, L., ... Pape, K. (2008). Finding concealed active faults: Extending the southern Whidbey Island fault across the Puget Lowland, Washington. *Journal of Geophysical Research: Solid Earth*, *113*(5), 1–25.

Sherrod, B. L., Brocher, T. M., Weaver, C. S., Bucknam, R. C., Blakely, R. J., Kelsey, H. M., ... Haugerud, R. (2004). Holocene fault scarps near Tacoma, Washington, USA. *Geology*, *32*(1), 9.

Slawson, W. F., & Savage, J. C. (1979). Geodetic Deformation Associated with the 1946 Vancouver Island, Canada, Earthquake. *Bulletin of the Seismological Society of America*, *69*(5), 1487–1496.

Steffen, R., Steffen, H., Wu, P., & Eaton, D. W. (2014). Stress and fault parameters affecting fault slip magnitude and activation time during a glacial cycle. *Tec-*

tonics, *33*(7), 1461–1476.

Stuiver, M., & Polach, H. A. (1977). Reporting of 14C data. *Radiocarbon*, *19*(3), 355–363.

Styron, R. (2019, January). The impact of earthquake cycle variability on neotectonic and paleoseismic slip rate estimates. *Solid Earth*, *10*(1), 15–25.

Styron, R. H., & Sherrod, B. (2021, April). Improving Paleoseismic Earthquake Magnitude Estimates with Rupture Length Information: Application to the Puget Lowland, Washington State, U.S.A. *Bulletin of the Seismological Society of America*, *111*(2), 1139–1153.

Thenhaus, P., & Campbell, K. (2002, January). Seismic hazard analysis. In *Earthquake Engineering Handbook* (pp. 8–1).

van Loon, A. J. T., Pisarska-Jamroży, M., Nartišs, M., Krievāns, M., & Soms, J. (2016, September). Seismites resulting from high-frequency, high-magnitude earthquakes in Latvia caused by Late Glacial glacio-isostatic uplift. *Journal of Palaeogeography*, *5*(4), 363–380.

van Wijk, J., Axen, G., & Abera, R. (2017). Initiation, evolution and extinction of pull-apart basins: Implications for opening of the Gulf of California. *Tectonophysics*, *719–720*, 37–50.

Van Der Woerd, J., Tapponnier, P., Ryerson, F. J., Meriaux, A.-S., Meyer, B., Gaudemer, Y., . . . Zhiqin, X. (2002, March). Uniform postglacial slip-rate along the central 600 km of the Kunlun Fault (Tibet), from 26Al, 10Be, and 14C dating of riser offsets, and climatic origin of the regional morphology: Uniform slip-rate along the Kunlun Fault. *Geophysical Journal International*, *148*(3), 356–388.

Walton, M. A., Staisch, L. M., Dura, T., Pearl, J. K., Sherrod, B., Gomberg, J., . . . Wirth, E. (2021, May). Toward an Integrative Geological and Geophysical View of Cascadia Subduction Zone Earthquakes. *Annual Review of Earth and Planetary Sciences*, *49*(1), 367–398.

Wang, K. (2000). Stress-strain 'paradox', plate coupling, and forearc seismicity at the Cascadia and Nankai subduction zones. *Tectonophysics*, *319*(4), 321–338.

Wang, K., Mulder, T., Rogers, G., & Hyndman, R. (1995, July). Case for very low coupling stress on the Cascadia Ssubduction Fault. *Journal of Geophysical Research*, *100*.

Wells, D. L., & Coppersmith, K. J. (1994). Empirical relationships among magnitude, rupture length, rupture width, rupture area and surface displacements. *Bulletin of the Seismological Society of America*, *84*(4), 974–1002.

Wells, R. E., Blakely, R. J., & Bemis, S. (2020). Northward migration of the Oregon forearc on the Gales Creek fault. *Geosphere*, *16*(2), 660–684.

Wells, R. E., Weaver, C. S., & Blakely, R. J. (1998). Fore-arc migration in Cascadia and its neotectonic significance. *Geology*, *26*(8), 759–762.

Wesnousky, S. G. (2008, August). Displacement and Geometrical Characteristics of Earthquake Surface Ruptures: Issues and Implications for Seismic-Hazard Analysis and the Process of Earthquake Rupture. *Bulletin of the Seismological Society of America*, *98*(4), 1609–1632.

Yorath, C. J., Clowes, R. M., Green, A. G., Sutherland-Brown, A., Brandon, M. T., Massey, N. W., … Hyndman, R. D. (1985). Lithoprobe - Phase 1: Southern Vancouver Island: Preliminary Analyses of Reflection Seismic Profiles and Surface Geological Studies. *Paper - Geological Survey of Canada*(pt A), 543–554.

Yorath, C. J., Green, A. G., Clowes, R. M., Brown, A. S., Brandon, M. T., Kanasewich, E. R., & Spencer, C. (1985). Lithoprobe , southern Vancouver Island: Seismic reflection sees through Wrangellia to the Juan de Fuca plate. *Geology*, *13*(13), 759–762.

Zinke, R., Dolan, J. F., Rhodes, E. J., Van Dissen, R., & McGuire, C. P. (2017). Highly Variable Latest Pleistocene-Holocene Incremental Slip Rates on the Awatere Fault at Saxton River, South Island, New Zealand, Revealed by Lidar Mapping and Luminescence Dating. *Geophysical Research Letters*, *44*(22), 11,301–11,310.

Late Pleistocene to Holocene transtension in the northern Cascadia forearc: Evidence from surface ruptures along the Beaufort Range fault

Emerson M. Lynch[1,2], Christine Regalla[1], Kristin D. Morell[3], Nicolas Harrichhausen[4], and Lucinda J. Leonard[5]

[1]School of Earth and Sustainability, Northern Arizona University, Flagstaff, AZ, USA
[2]Department of Earth and Environmental Geoscience, Washington and Lee University, Lexington, VA, USA
[3]Department of Earth Science, University of California, Santa Barbara, CA, USA
[4]Univ. Grenoble Alpes, Univ. Savoie Mont Blanc, CNRS, IRD, Univ. Gustave Eiffel, ISTErre, 38000 Grenoble, France
[5]School of Earth and Ocean Sciences, University of Victoria, Victoria, BC, Canada

Key Points:

- Field mapping and surveys confirm multiple Late Pleis. to Holoc. surface ruptures along the Beaufort Range Fault (BRF).
- Kinematic inversions show the BRF has accommodated right-lateral transtension along a steeply NE dipping fault since the Late Pleis.
- BRF geometry and kinematics are similar to 1946 Vancouver Island earthquake mechanism, making it a candidate source fault for that event.

Corresponding author: Emerson M. Lynch, `emerson.lynch@gmail.com`

Abstract

The active deformation field in subduction forearcs provides critical information about the stress and strain state of the upper plate and its potential for seismogenesis. However, these properties are challenging to quantify in most subduction systems, and in the northern Cascadia forearc, few faults have been identified that can be used to reconstruct the upper plate deformation field. Here we investigate the slip history of the Beaufort Range fault (BRF) on Vancouver Island. This fault was proposed to host the 1946 M7.3 Vancouver Island earthquake, but no surface rupture or evidence of Quaternary activity has been documented, and the stress and strain conditions that promoted this event are poorly understood. We provide the first evidence that the BRF is active, using newly-collected lidar to map topographic scarps along the fault system and to reconstruct slip vectors from offset geomorphic markers. Quaternary deposits and landforms that show increasing magnitude of displacement with age provide evidence for at least three M_W ~6.5-7.5 earthquakes since ~15 ka, with the most recent event occurring <3-4 ka. Kinematic inversions of offset geomorphic markers show that the BRF accommodates right-lateral transtension along a steeply NE-dipping fault. This fault geometry and kinematics are similar to those modeled for the 1946 earthquake, suggesting that the BRF is a candidate source fault for this event. We find that the kinematics of the BRF are consistent over decadal to millennial timescales, suggesting that this portion of the northern Cascadia forearc has accommodated transtension over multiple earthquake cycles.

Plain Language Summary

Subduction zones, like Cascadia, contain onshore fault networks that can host earthquakes that are dangerous to communities. However in many locations, like Vancouver Island, Canada, we know little about where these faults are and what type and magnitude earthquake they can host (if any). We focus on the Beaufort Range fault (BRF) on Vancouver Island, and show for the first time that the BRF hosted recent earthquakes. Newly-available high-resolution topography data show many scarps, or vertical offsets of the ground surface produced in past earthquakes, along a >40 km zone. Surveys of landforms that have been offset by the BRF show both vertical and horizontal offsets along a near-vertical fault. The nearby 1946 Vancouver Island earthquake had similar vertical and horizontal offsets along a near-vertical fault, suggesting that this earthquake might have happened on the BRF. Our data show there have been >3 large earthquakes on the BRF in the past ∼15,000 years, the most recent <3,000-4,000 years ago. The offsets we observe suggest these earthquakes had magnitudes between ∼6.5 and 7.5. Future similar earthquakes could cause shaking damage to many nearby communities, including the cities of Port Alberni and Nanaimo, and nearby hydroelectric facilities.

1 Introduction

Quantifying the stress state and strain history of subduction zone forearcs is critical for understanding the energy budget of convergent margins (e.g., Huang et al., 2022), the seismic potential and hazard of forearc faults (e.g., Wang et al., 1995; Balfour et al., 2011; Thenhaus & Campbell, 2002), and the evolution of the upper plate during the megathrust seismic cycle (e.g., Regalla et al., 2017; Herman & Govers, 2020). However, stress is notoriously difficult to measure or approximate, and in the northern Cascadia forearc of Vancouver Island, there are several competing models for what controls forearc stress and upper plate deformation (e.g., Mazzotti et al., 2011; Finley et al., 2019; Delano et al., 2017). Quantifying upper plate deformation is also limited in Cascadia because the subduction zone is relatively seismically quiet, limiting our ability to infer stress field data from seismicity. Furthermore, the large locking signal on the plate interface inhibits our ability to isolate Global Navigation Satellite System (GNSS) deformation associated with upper plate faults (e.g., Mazzotti et al., 2011; S. Li et al., 2018), and few active upper plate faults have been identified regionally to date (e.g., Morell et al., 2017).

Although the northern Cascadia region exhibits relatively low rates of instrumental seismicity, this region was also host to the largest onshore historic earthquake in Canada, the M 7.3 1946 Vancouver Island earthquake (Rogers & Hasegawa, 1978; Rogers, 1979; Lamontagne et al., 2018). This earthquake is the largest to have occurred anywhere within the Cascadia subduction zone system, including the megathrust, since written historical recordkeeping began (the past ∼200 yrs). However, despite this earthquake's size and moderate damage to nearby population centers (Hodgson, 1946; Mathews, 1979; Clague, 1996), the fault that ruptured during the 1946 earthquake remains unknown. In addition, little is known about the current or past stress state and strain field of the crust surrounding this major historical rupture, what upper plate conditions could lead to future ruptures, and if similar events have occurred in the geologic past. Such data are necessary not only to evaluate the seismic potential of forearc faults, but also to determine their deformation rates, kinematics, and relationship to the regional stress field. Yet, no

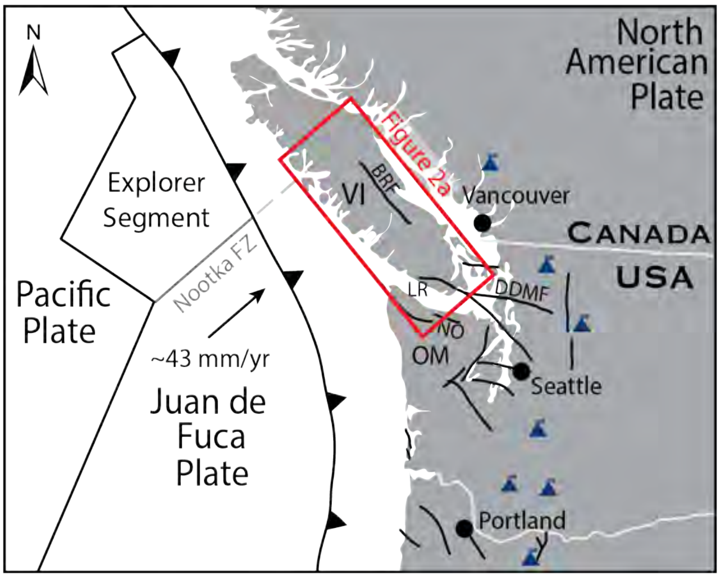

Figure 1. Regional tectonic setting showing the location of the Beaufort Range fault (BRF) and other active faults in the Cascadia forearc of Canada and the USA. Juan de Fuca – North America convergence vector after Kreemer et al. (2014). Slab depth contours from Slab2 (Hayes et al., 2018). Active faults in USA after USGS (Geological Survey, n.d.), Leech River fault after Morell et al. (2017), volcanoes after AGI (2003). Red box shows location of Figure 2a. DDMF – Darrington-Devils Mountain fault; FZ — fault zone; LR – Leech River fault; NO - North Olympic fault zone; OM - Olympic Mountains; VI - Vancouver Island.

active faults have been identified north of the greater Victoria region to date, including in the region surrounding the approximate epicenter of the 1946 earthquake.

Here, we investigate the kinematics and slip history of the Beaufort Range Fault (BRF), a major fault in the northern Cascadia forearc, to evaluate how forearc strain is accommodated on this structure over decadal to millennial timescales. The BRF is located on central Vancouver Island, near the northern terminus of the Cascadia subduction zone (Figure 1). Several researchers proposed that the Beaufort Range fault may have hosted the 1946 rupture, based on the proximity of the epicenter, coseismic slip modeled from geodetic benchmark surveys, and the similarity of the BRF strike to the NW-SE striking nodal plane for the event's focal mechanism (Rogers & Hasegawa, 1978; Slawson & Savage, 1979). However, no surface ruptures were found by researchers in the days and weeks following the rupture, and it remains unknown whether the BRF hosted the 1946 earthquake, or whether this fault is Quaternary-active or seismogenic.

In this paper, we undertake a field-based tectonogeomorphic investigation to evaluate the seismogenic potential of the BRF and to determine its slip history and kinematics with respect to historical seismicity and regional tectonics. We exploit a well-preserved set of offset paleochannels on the southwestern flank of the Beaufort Range, visible in recently acquired bare-earth lidar Digital Elevation Models (DEMs), to demonstrate that the BRF is a highly active, right-lateral transtensional fault that has hosted multiple surface-rupturing earthquakes throughout the Quaternary. We find evidence for at least three late Pleistocene to Holocene earthquakes along the BRF, with surface ruptures extending >40 km, consistent with paleo-earthquake magnitudes of ∼6.5 to 7.5. While these data do not constrain the age of the most recent surface-rupturing event, our results do suggest that the most recent event occurred in the past ∼3-4 kyr. We find that paleoseismic earthquakes along the BRF have kinematics similar to the 1946 Vancouver Island earthquake, suggesting that the BRF is a candidate host fault for this event. Finally, the similarities of the BRF deformation field and P- and T-axes derived from its slip over decadal to millennial timescales, suggest the stresses that lead to permanent deformation in this portion of the northern Cascadia forearc have been relatively consistent over multiple earthquake cycles.

2 Background

2.1 Tectonic Setting

The BRF is located in the northern forearc of the Cascadia subduction zone, where the Juan de Fuca plate subducts under the North American plate at a rate of ∼43 mm/yr (DeMets et al., 2010; Kreemer et al., 2014). The fault is positioned ∼150 km north of the Olympic Mountains, and ∼60 km south of the onshore projection of the Nootka fault zone, the northern end of the Juan de Fuca slab (Figure 1). Active faults that accommodate forearc strain have been recognized along most of the Cascadia subduction zone south of the Olympic Mountains (e.g., Figure 1; Brocher et al., 2001; Goldfinger et al., 1992; Liberty et al., 2003; Personius et al., 2003; Sherrod et al., 2004; Kelsey et al., 2008; R. E. Wells et al., 2020; Horst et al., 2021), and north of the Olympic Mountains (e.g., Figure 1; Schermer et al., 2021; Morell et al., 2017, 2018; Harrichhausen et al., 2021). However, no active faults have been identified in the northern 150-300 km of the forearc on Vancouver Island. It remains unclear if and how the slip accommodated by these southern faults is translated farther north and what role the BRF may play in accommodating forearc strain.

The BRF occurs along the southwestern flank of the Beaufort Range, near the city of Port Alberni on Vancouver Island (Figure 2a). The Beaufort Range consists of a ~70 km long, ~5-10 km wide set of peaks, whose elevations range from 1000 to 1600 masl. The range is asymmetric, with a gently sloping, glacially scoured northeastern flank that slopes toward the Strait of Georgia, and a steep (up to 35°) southwestern flank that slopes toward the Alberni Valley (Figure 2b). The BRF strikes NW-SE, following the southwestern topographic range front for >40 km (Figure 2b).

2.2 Eocene slip along the Beaufort Range thrust fault

The BRF has been previously mapped as an Eocene bedrock fault that places the Late Triassic Karmutsen Formation basalts that form the peaks of the Beaufort Range over the Cretaceous Nanaimo Group sediments that underlie the Alberni Valley (Figure 2a, Figure S1; Yorath, Clowes, et al., 1985; T. England & Calon, 1991). Geologic mapping, balanced cross sections, and LITHOPROBE seismic reflection profiles suggest this bedrock thrust fault dips NE, at 45° to sub-vertical (Yorath, Clowes, et al., 1985; Yorath, Green, et al., 1985; Clowes et al., 1987). Geologic maps depict the BRF as an along-strike projection of the frontal thrust fault of the Cowichan Fold and Thrust System (CFTS), located ~40 km along strike to the southeast of the BRF (Cui et al., 2017; T. England & Calon, 1991). Low-temperature thermochronology data indicating exhumation at ~50-40 Ma suggest the thrust faults of the CFTS, including the BRF, initially formed during the Eocene accretion of the Pacific Rim and Crescent terranes (T. D. J. England, 1990; T. England & Calon, 1991; T. D. J. England et al., 1997).

2.3 Glacial history

The Beaufort Range and Alberni Valley experienced two major phases of glaciation during the last glacial period. The region was inundated by the south-southwestward flowing Cordilleran continental ice sheet during the Fraser stage glaciation (~25-12 ka; Fyles, 1963; Alley & Chatwin, 1979). Then, during the retreat of the ice sheet, the Alberni Valley was occupied by a southeastward flowing valley glacier that produced streamlined landforms and associated glacial deposits (Mosher & Hewitt, 2004; Easterbrook, 1992; Clague & James, 2002). Existing maps document sub-glacial till, colluvial, and al-

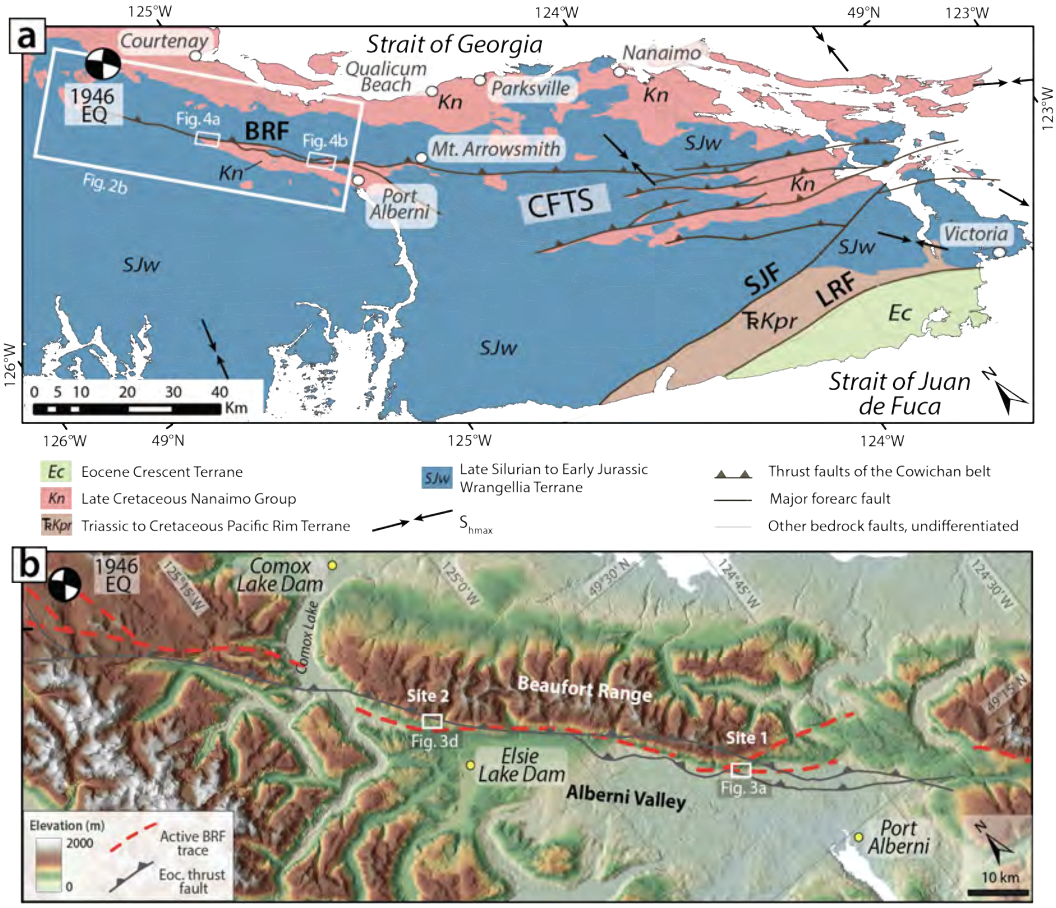

Figure 2. Geologic and geomorphic setting. **A:** Simplified geologic map of southern Vancouver Island showing major lithologic units, thrust faults of the Cowichan fold and thrust system (CFTS), and other forearc faults. The epicenter of the 1946 M 7.3 Vancouver Island earthquake is shown by the focal mechanism (Rogers & Hasegawa, 1978). Maximum horizontal stress directions after Balfour et al. (2011). Bedrock geology after the British Columbia Geological Survey compilation by Cui et al. (2017). BRF—Beaufort Range fault. LRF—Leech River fault. SJF—San Juan fault. **B:** Hillshaded SRTM DEM showing the topography of the Beaufort Range and Alberni Valley, the locations of hydroelectric dams, the trace of the Eocene bedrock Beaufort Range thrust fault (in legend), and a simplified inferred trace of the active BRF (in legend) based on the locations of mapped scarps (Supplemental Figure S1).

luvial deposits that extend to an elevation of ∼300 m along the range front (Fyles, 1963). These deposits have been correlated to the last glacial maximum at ∼13.6-11 ka, based on ages from marine shells, peat, and wood in glaciomarine deposits in the Strait of Juan de Fuca and along the eastern coast of Vancouver Island (e.g., Clague, 1980; Easterbrook, 1992). However, there has been limited surficial mapping of the Beaufort Range front, and no deposits in the Alberni Valley region have been directly dated. We expand and refine these mapping data to constrain the ages of deposits offset by scarps and evaluate the Quaternary activity of the BRF.

2.4 Possible association of the BRF with the 1946 Vancouver Island earthquake

Although post-Eocene deformation has not been previously documented along the BRF, several researchers proposed that the Beaufort Range fault may have hosted the 1946 M 7.3 Vancouver Island earthquake. The earthquake epicenter was located at the northern tip of the BRF at a depth of <30 km, and focal mechanism solutions contain a NW-SE striking nodal plane sub-parallel to the BRF (Figure 2; Rogers & Hasegawa, 1978). These data led Rogers and Hasegawa (1978) to propose that the 1946 earthquake may have been a right-lateral oblique event hosted by the BRF (Figure 2). Geodetic surveys of a triangulation network before and after the event suggest ∼1-2.5 m of right-lateral oblique slip along a steeply NE dipping (70°) fault. While multiple ground surface failures and slumps have been identified around the Beaufort Range associated with the 1946 event (Mathews, 1979; Clague, 1996), no fault-related surface ruptures associated with the 1946 event were ever discovered.

3 Methods

Our methodological approach is motivated by newly available lidar bare-earth elevation models along the surface trace of the Beaufort Range fault that reveal a series of topographic scarps that suggest the fault has accommodated Quaternary offset (Figure 2b). These scarps, clearly visible in bare-earth lidar DEMS (Figure 3), occur in en echelon arrays of 1-6 sets, each ∼100-500 m long, and spaced 10s to 100s of meters apart. The majority of well-preserved scarps are located near the base of the range—20-100 m above the valley floor, or 500-870 m below the range crest—and strike sub-parallel to the trend of the southwestern flank of the Beaufort Range front (∼290-320°; Figure 2b, Fig-

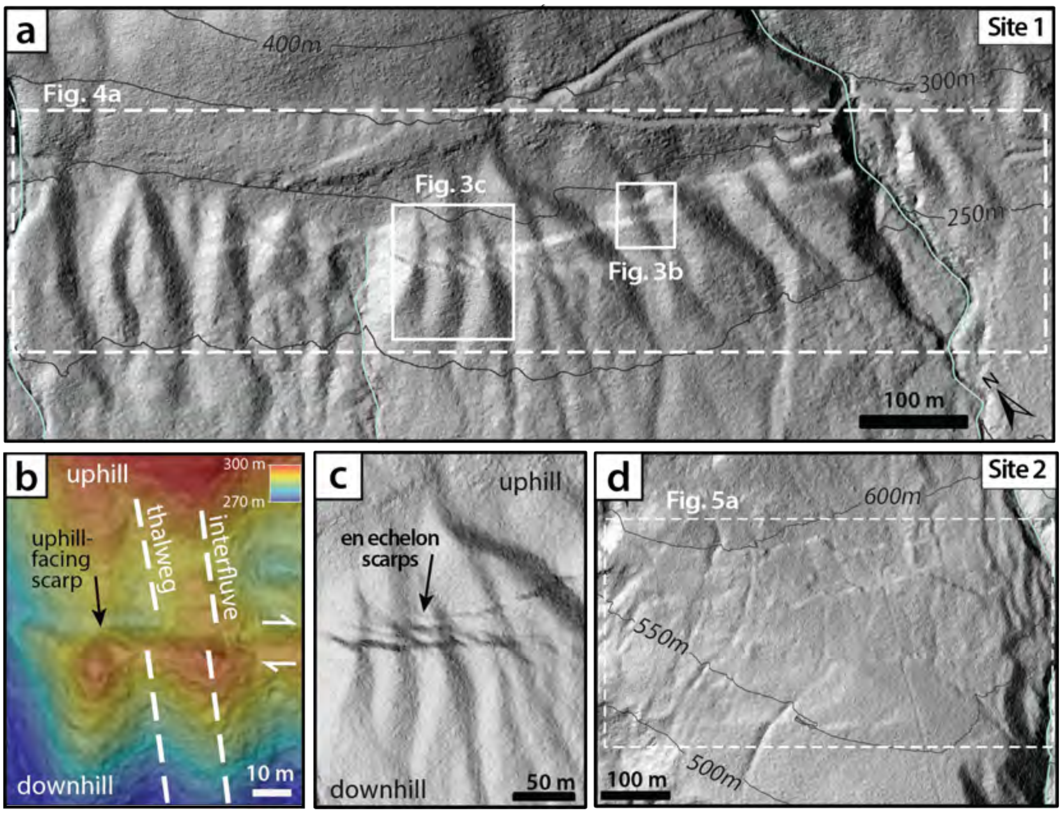

Figure 3. Examples of tectonic fault scarps visible in hillshaded bare-earth lidar DEMs. **A:** Unannotated DEM of Site 1 showing a network of en echelon fault scarps offsetting a series of abandoned channels and interfluves. **B:** Example of an uphill-facing scarp developed on a till-mantled hillside. The scarp offsets a channel thalweg and adjacent interfluve crests both vertically (downhill-side-up) and right-laterally. **C:** Example of en echelon array of scarps at Site 1. **D:** Unannotated DEM of Site 2 showing a network of right-laterally sheared channels. Examples of non-tectonic landforms are presented in Supporting Information Figure S2.

ure S1). Our initial observations of the lidar data suggested these scarps exhibit apparent right-lateral and SW-side-up 1-10-m scale displacement of a network of V-shaped paleochannels with paired offset sharp-crested interfluves. Given the glacial history of the region, we surmised that these channels may be no older than the time of ice retreat, and therefore the offset channels may record Holocene fault displacement.

Based on these initial observations, we undertook detailed field-based mapping and topographic surveying of faults and offset landforms to determine the geometry of the fault networks potentially associated with these scarps, the relative ages of offset deposits, the magnitude of potential offset, and the associated kinematics of fault slip.

3.1 Mapping

We completed surficial and bedrock mapping in order to: 1) identify earthquake-generated fault scarps along the BRF, 2) determine the relative ages of Quaternary deposits offset by surface ruptures, and 3) determine if active fault strands re-occupied inherited bedrock faults or shear zones. Identifying fault-related deformation (e.g., fault scarps) in datable Quaternary sediments is essential for characterizing the slip history of active faults (e.g., Van Der Woerd et al., 2002; Zinke et al., 2017; Hatem et al., 2017; Regalla et al., 2022), but dense temperate rainforest limits exposures and accessibility of offset Quaternary deposits in the study area. Thick soils and dense vegetative cover limit bedrock exposures to road cuts, logging roads, quarries, and stream channels, and obscure many Quaternary landforms beneath the forest canopy. However, these fault-related landforms are well-resolved in the newly available lidar point clouds collected along the BRF.

We used bare-earth lidar data, satellite imagery, and historical air photos to map potentially earthquake-generated fault surface ruptures (scarps) within a ∼100 km-long swath area extending from Mt. Arrowsmith to the Forbidden Plateau (Figure S1). Lidar point cloud data were collected by Terra Remote Sensing, and TimberWest and Island Timberlands logging companies provided ground returns. The lidar point clouds contained an average of ∼1.2-1.4 ground returns per square meter. We gridded these data into a 0.5 m DEM and generated topographic derivatives such as hillshade, standard deviation, and slope maps to aid in mapping. We additionally used satellite imagery (Google Earth Pro, 2017) and British Columbia provincial government historical air photos from

1947 and 1952 to evaluate any anthropogenic modification of key sites, including past roads, railroads, and logging trails.

We visited each accessible remotely-mapped scarp to confirm they were tectonically-generated features (i.e., not related to slumping, etc.). Criteria used to distinguish fault scarps from other features include whether the features are linear, continuous over >50-100 m length scales, are cut across topography, and if they offset hillslopes, abandoned channels, or interfluves (Figure 3b-c). We took care to distinguish potentially fault-related scarps from landforms produced by glacial deposition or scour, anthropogenic disturbance, gravitational failure, or differential erosion (see Supporting Information Text S1 and Figure S2).

We then completed highly detailed and more focused field mapping, at a scale of 1:3000, of Quaternary deposits and bedrock units in two ∼6 km by ∼2 km regions (Sites 1 and 2) that each contain a high density of fault scarps (Figures 3, 4). Surficial mapping was completed based on field and lidar-based observations of surface topography, roughness, morphology, and inset and burial relationships, accompanied by detailed lithologic descriptions of each Quaternary unit. We used these observations to create a local Quaternary stratigraphy that allowed us to determine the relative ages of units offset by faults. Bedrock mapping was completed using outcrops exposed in road cuts, streams, and quarries. We measured the structural orientations of fault planes, slickenlines, foliation fabrics, and fractures within the principal shear zones and damage zones, where exposed.

3.2 Quantifying fault slip

3.2.1 Topographic surveys of offset landforms

We collected topographic survey data across fault scarps at 64 locations at Sites 1 and 2 in order to determine the attitudes of fault planes associated with fault scarps, and to quantify the vertical and lateral offset of displaced Quaternary deposits and landforms (Figures 5 and 6). These data included 58 surveys of offset geomorphic piercing lines where the three-dimensional oblique slip vector could be calculated (Figure 7), and 6 additional "straight-line" profiles used to calculate the vertical component of displacement in locations where geomorphic piercing lines were absent (Figures 5, 6, S4, and Dryad data repository Lynch et al., 2023). Surveys were collected with a Nikon XS and Spectra Precision Focus 6 total station, which yielded more continuous topographic data than

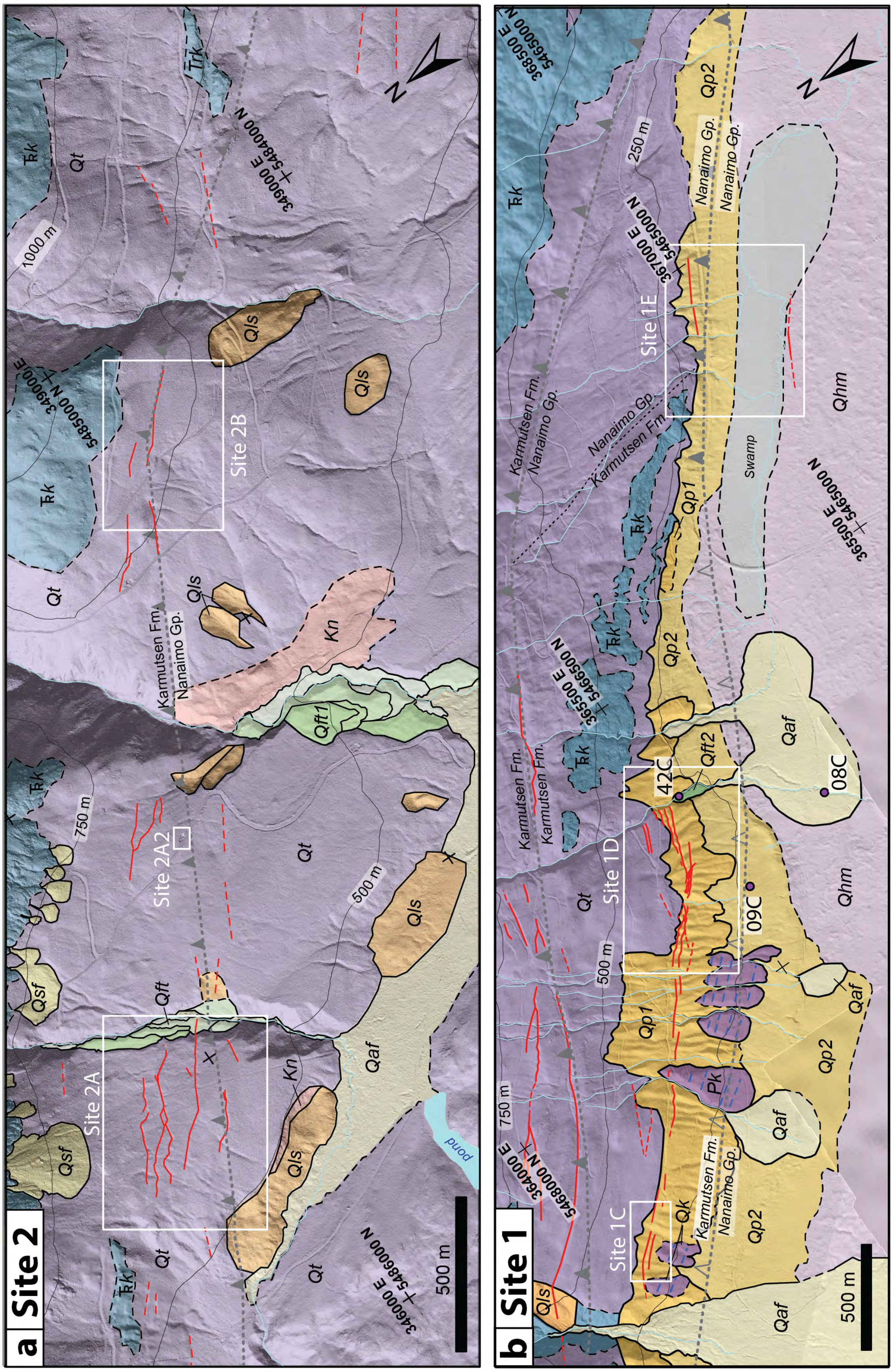
a Site 2
b Site 1
Site 2A
Site 2A2
Site 2B
Site 1C
Site 1D
Site 1E
Karmutsen Fm.
Nanaimo Gp.
Swamp
pond
500 m
750 m
1000 m
250 m
08C
09C
42C

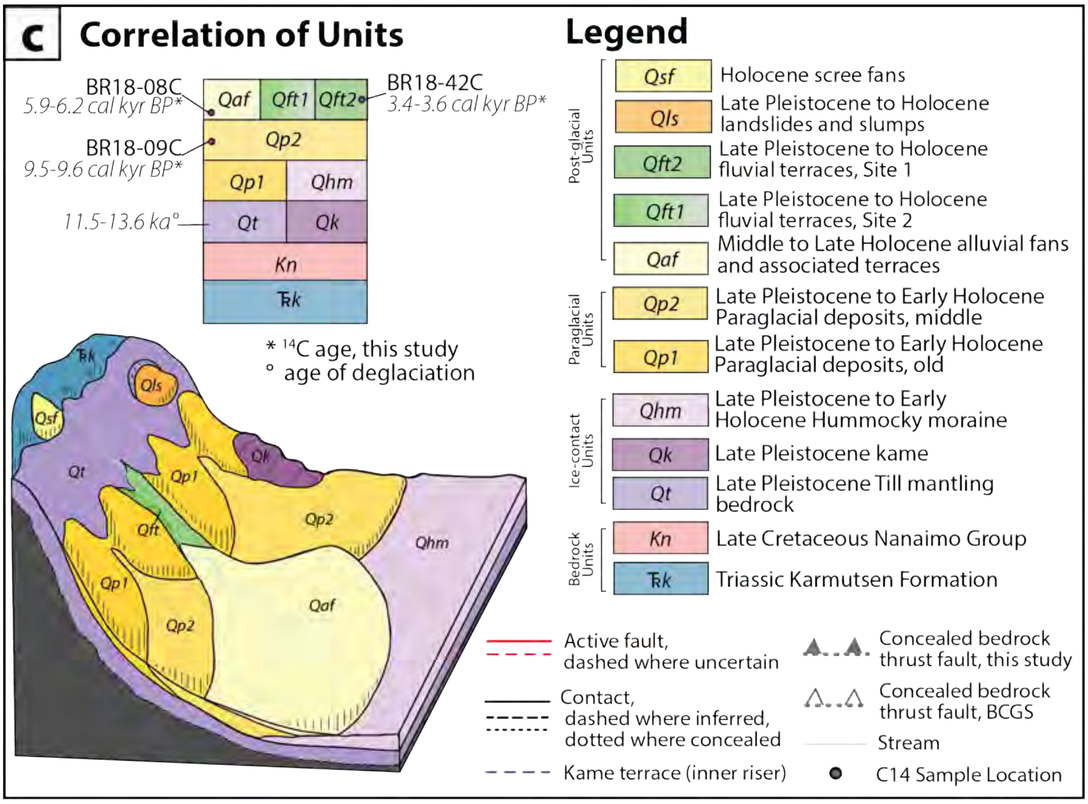

Figure 4. Bedrock and surficial geology of portions of the BRF (See locations in Figure 2a). Mapping is overlain on a composite hillshaded DEM compiled from two bare-earth lidar DEMs gridded to 0.5 m and to 2 m, and from 30 m SRTM DEM. Radiocarbon ages are reported in Table 1. Bedrock fault locations compiled from new field mapping and existing mapping by the British Columbia Geological Survey (BCGS; Cui et al., 2017). White boxes outlining Sites A-E correspond to locations shown in Figures 5 and 6. **A:** Map of Site 2 along the northern portion of the BRF. **B:** Map of Site 1, along the southern portion of the BRF. Fault scarps (red lines) occur at the base of the Beaufort Range and along the rangefront up to 1000 m above the valley floor. Mapped scarps occur in both the hanging wall and footwall of the bedrock BRF. Fault scarps offset multiple ages of glacial (Qt), paraglacial (Qp1, Qp2), and modern deposits (Qls, Qft, Qaf). Terrace generations within unit Qft1 in panel A are depicted by increasing color saturation with terrace age, delineated by thin gray lines. **C:** Correlation of units and legend for geologic maps in panels A and B. Radiocarbon ages demonstrate that these deposits are ~9600-3400 cal BP in age (Table 1).

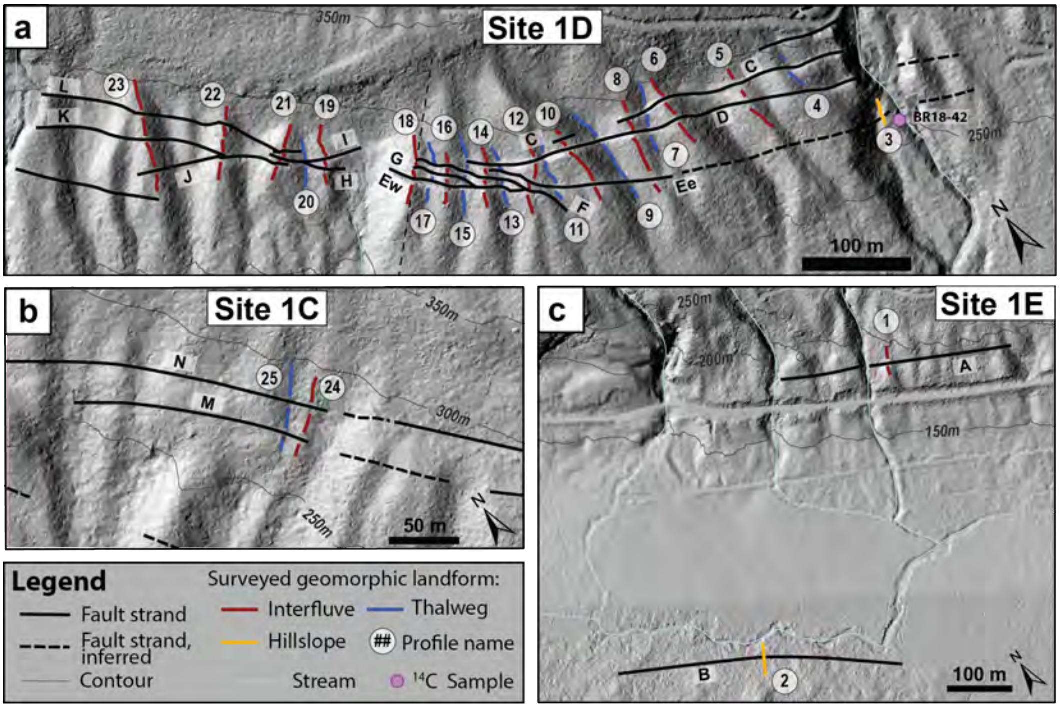

Figure 5. Hillshaded lidar DEMs of Site 1 showing mapped faults (labelled from A to N) and surveyed topographic profiles (numbered from 1 to 25). See Figure 4 for locations and Dryad data repository for topographic profile survey data (Lynch et al., 2023). **A:** Annotated hillshaded DEM showing the locations of mapped fault strands and topographic survey profiles at Site 1D. Unannotated lidar DEM is presented in Figure 3a. **B** and **C:** Annotated DEMs of Sites 1C and 1E. Unannotated versions of all DEMs are in Supporting Information Figure S3.

the lidar DEMs which had non-uniform return spacing and included some false ground returns.

Our primary survey targets were a series of abandoned channels and interfluves at Sites 1 and 2 whose axes intersect fault scarps at near-orthogonal angles, that serve as piercing lines from which fault slip vectors can be reconstructed. Topographic surveys of these landforms followed either the channel thalweg or the interfluve crest. In locations where channels and interfluves are absent, we collected linear profiles with trends perpendicular to the fault scarp. For each profile, total station survey data were collected every ~0.5-1 m, to a distance of >20 m uphill and downhill of each fault scarp (Figure 7). Along survey transects where a geomorphic piercing line extended for less than 20 m (e.g., between closely-spaced fault strands), we collected a minimum of 3 survey points, with an average of 11 points. We complemented these ground surface elevation profiles

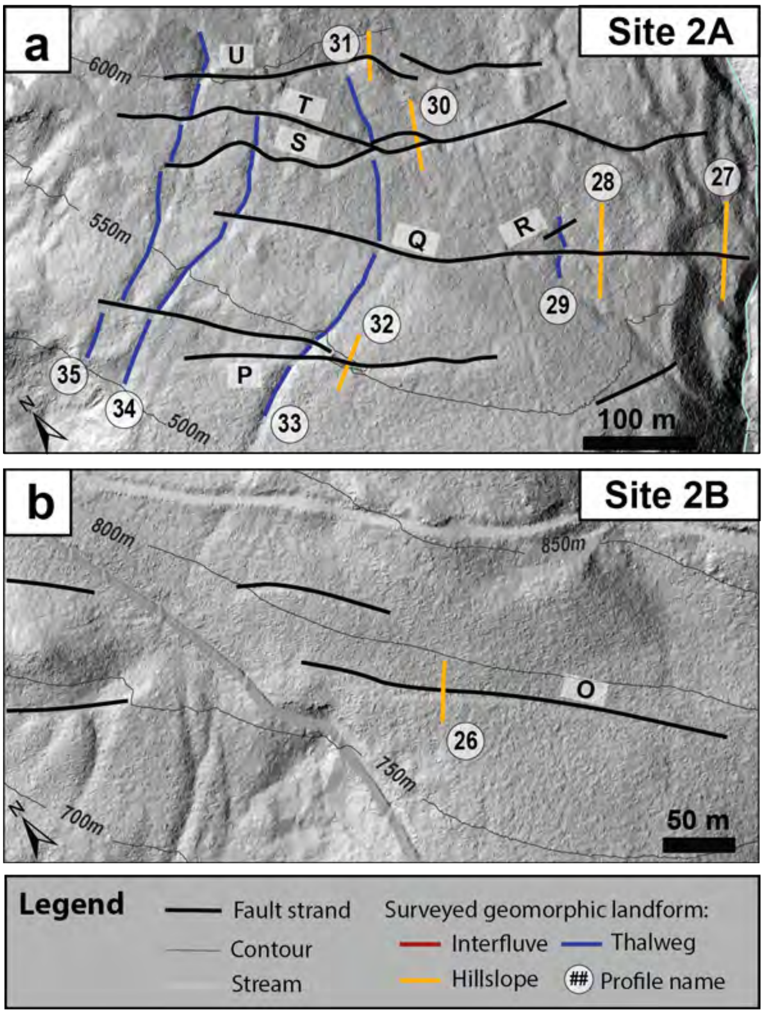

Figure 6. Hillshaded DEMs of Site 2 showing mapped faults (labelled from O to U) and surveyed topographic profiles (numbered from 26 to 35). See Figure 4 for locations and Dryad data repository for topographic profile survey data (Lynch et al., 2023). **A:** Annotated hillshaded DEM showing the locations of mapped fault strands and topographic survey profiles at Site 2A. Unannotated lidar DEM is presented in Figure 3d. **B:** Annotated DEM of Site 2B showing mapped faults and surveyed profile. Unannotated versions of all DEMs are in Supporting Information Figure S3.

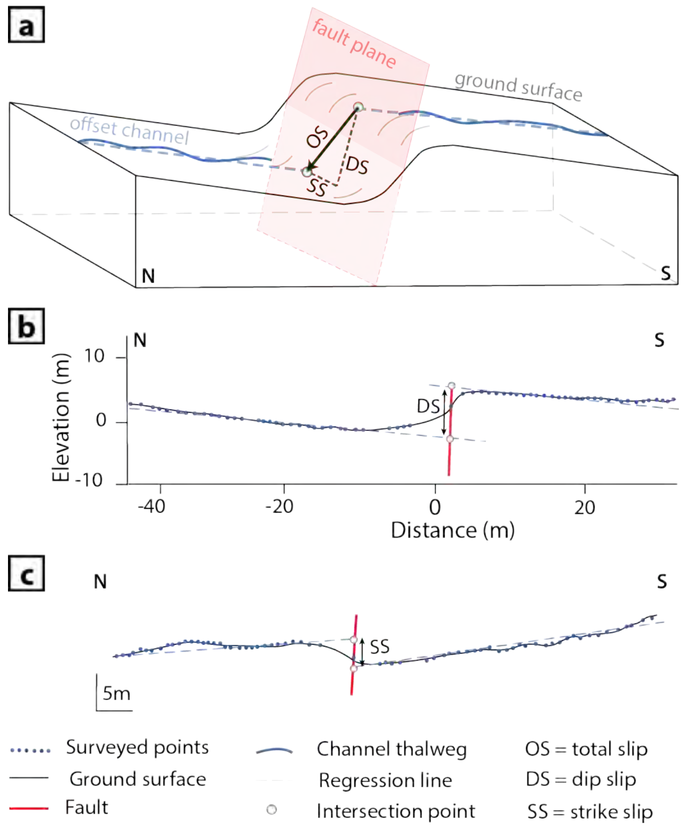

Figure 7. Schematic diagrams showing how surveyed geomorphic piercing lines were used to reconstruct 3D fault slip. **A:** Block diagram showing an oblique normal right lateral offset channel thalweg. Fault slip components (OS, DS, and SS) are calculated from the 3D positions of the intersections of the fault plane with the linear projections of the upthrown and downthrown channel segments. **B:** Example of a surveyed geomorphic piercing line profile in cross-section. **C:** Example of a surveyed geomorphic piercing line profile in plan view. In each survey, points were collected every ~0.5-1 m at least 10-20 m beyond the fault scarp.

with six additional topographic profiles extracted from lidar DEMs in a portion of Site 2A where thick forest cover and uneven topography prevented total station surveys of offset abandoned channels.

3.2.2 Reconstructing oblique fault displacement

We used the topographic survey data to reconstruct both the magnitude and orientation of the slip vector at each surveyed location where a geomorphic piercing line intersected an individual fault plane. In order to calculate a slip vector, the local orientation of the fault plane must be known. No outcrop exposures of fault planes in Quaternary deposits were present in the field area, but we were instead able to reconstruct the local strike and dip of the fault plane associated with mapped scarps using a modified three-point problem approach. In this approach, we assumed the midpoint, or inflection point, of a fault scarp represents the most likely intersection of the fault plane with the surface. We surveyed scarp midpoints at a range of elevations ($\sim$4-12 m elevation range) and determined fault strike and dip through linear regression of a plane through the surveyed scarp midpoints using all surveyed data along a single continuous fault strand segment (3-17 points per regression). We used these data to determine a representative fault dip for each scarp segment, using the average dip from all regressions at Site 1 or Site 2, and a representative fault strike given by the local strike of each fault strand or segment. Because fault dips determined from surveys of degraded scarp faces over small elevation ranges may underestimate true fault dip, we allowed our model reconstructions to permit fault dip to be 5° steeper than that calculated from the three-point approach.

We combined our fault plane solutions and topographic survey data to calculate the 3D offset of each piercing line, specifically the magnitude and direction (trend and plunge) of the slip vector (Figure 7). Calculations were made using an R script that performed a Monte Carlo simulation to evaluate the slip vector and associated uncertainty (script available in data repository, Lynch et al., 2023). The script requires the following user-defined inputs: the strike and dip of the fault plane, the 1σ uncertainty on strike and dip, the XYZ coordinates of the topographic survey data, the location where the fault plane intersects the ground surface, and the number of survey points in the upthrown and downthrown sides of the profile used to define the 3D geometry of the piercing line segments. For each profile, we assigned a fault strike and dip as described above, and $\pm$ 1σ uncertainty (5°). We manually defined the remaining parameters—fault plane intersections, and the number of survey points used to fit linear regressions through the upthrown and downthrown surveyed piercing lines—for each topographic profile. It has been well-documented that how a user defines fault and piercing line geometry (i.e., profile regression limits) can lead to multiple admissible geologic slip reconstructions (e.g., Scharer et al., 2014). To account for this uncertainty, we performed Monte Carlo simulations for each offset profile using input defined by five different users, each trained in scarp offset analysis.

Using these inputs, we used the R script to calculate 3D linear regressions through topographic survey points on the upthrown and downthrown sides of the fault scarp and then solve for the intersection points of these lines with the fault plane (Figure 7). These two intersection points were then used to calculate the magnitudes of strike slip (SS), dip slip (DS), and oblique slip (OS) for each piercing line, as well as the trend and plunge of the slip vector (Figure 7). The Monte Carlo simulation was repeated 100 times for each of the five user-defined profile selections, yielding a total of 500 simulations of fault slip for each displaced piercing line. We report the outputs as the mean ± one standard deviation of the 500 values calculated for that profile.

3.2.3 Inversion for fault kinematics

We use the slip vector data to invert for the kinematics of the BRF using the FaultKin 7.6 program (Marrett & Allmendinger, 1990; Allmendinger et al., 2012). Data inputs included the trend and plunge of the best-fit slip vector determined from the Monte Carlo simulations, and the corresponding fault plane strike and dip determined from the modified three-point fault plane regressions. Inversions were performed using data from each of the 55 fault scarp surveys with vertically and laterally offset piercing lines. We grouped data for kinematic inversions in two ways. First, we grouped data collected at each mapping sub-site (A-E in Figure 4), to produce kinematic inversions representative of slip observed at each site location. Then, we grouped all data for the entire BRF to determine a kinematic inversion best fit to all observed data. Kinematic inversions were performed by calculating P- and T-axes from each calculated slip vector and fault plane pair, and then generating Bingham fault plane solutions from the set of P- and T-axes at each site (Marrett & Allmendinger, 1990; Allmendinger et al., 2012). These inversions assume slip occurs in the direction of maximum resolved shear stress on the fault plane, and produces mean P- and T-axes, pseudo focal mechanisms, and predicted slip vectors for each nodal plane (Marrett & Allmendinger, 1990; Allmendinger et al., 2012). These kinematic inversions and P- and T-axes provide information about paleo strain fields, and may, under certain assumptions, be used to approximate local stress axis orientations at the time of deformation (e.g., Angelier & Mechler, 1977; Riller et al., 2017).

3.3 Radiocarbon dating of Quaternary deposits

We collected charcoal samples from natural and manmade exposures of mapped Quaternary deposits to determine the chronologic ages of units offset by mapped faults. We focused our sampling on detrital charcoal as charcoal is present in many deposits on Vancouver Island, has previously been used to evaluate late Pleistocene to Holocene unit ages (e.g., Clague, 1980; Morell et al., 2018; Harrichhausen et al., 2021), and because luminescence techniques have not yielded reliable ages for late Pleistocene to Holcoene deposits due to insufficient dose rate (e.g., Graham, 2017; Morell et al., 2018). We collected samples of macroscopic (macro) charcoal (>0.5 cm) where fragments were visible in outcrops of Quaternary deposits. If no macro charcoal was readily visible in an outcrop, we collected 1-2 L of bulk sediment and sieved the samples to extract any datable macro charcoal present. For all sample sites, we completed detailed unit descriptions and noted the sample's stratigraphic position within the deposit (Figure S3). We collected three macro charcoal samples and five bulk sediment samples from Site 1 (see Figure 4b for locations). Our sampling was focused on units mapped at Site 1 (Figure 4b), where we identified multiple generations of Quaternary deposits (see Section 4.2). We were unable to date any mapped deposits at Site 2 due to a lack of exposure.

Charcoal samples were cleaned and processed at Paleotec Services, Ottawa, Ontario, Canada. Macroscopic charcoal pieces were extracted from bulk sediment samples by flotation and wet sieving in warm tap water using nested sieves of 0.85 mm and 0.425 mm. All material greater than 0.425 mm was examined using a binocular microscope, and any isolated charcoal pieces were shaved of any adhering sediment. The largest shaved fragment from each sample was further sliced into smaller fragments to look for the presence of fine modern rootlet penetration and/or fungal contamination, including mycorrhizae, and rejected if contaminants were present.

Three Quaternary units yielded datable charcoal fragments that were processed for radiocarbon analysis (Table 1, Figure 4b). These included macro charcoal samples extracted from one outcrop (BR18-06C, -07C, and -08C), and two samples extracted from sieved bulk sediment from two additional outcrops (BR18-42C and BR18-09C). Sample BR18-08C was selected as the highest quality sample of the three charcoal fragments extracted from the outcrop exposure. Bulk sediment sample BR18-09C included three mm-sized charcoal pieces that were combined to ensure adequate sample mass for AMS after acid-base-acid (ABA) treatment (Table 1, Figure 4b, Figure S3). Unfortunately, the three remaining bulk sediment samples (BR18-10C, -11C, and -12C) were barren of charcoal. Samples were analyzed at the Keck Carbon Cycle AMS Laboratory at UC Irvine. Radiocarbon ages (reported following Stuiver & Polach, 1977) were calibrated using the INTCAL20 calibration curve (Reimer et al., 2020) and OxCal v4.4 (Bronk Ramsey, 1995, 2021). We report radiocarbon ages as the two-sigma (2σ) range of calendar years before present (1950).

3.4 Estimates of fault slip

We estimate slip rates at Site 1 using the cumulative oblique displacement measurements of three different ages of offset landforms, as well as radiocarbon dates from detrital charcoal that provide estimates of unit ages. We use two approaches to estimate slip rates, following the methods of DuRoss et al. (2020). The first is an "open-ended" approach that uses the cumulative slip of the oldest offset unit and that unit's estimated age. The second is a "closed interval" approach that uses the difference in slip that has occurred during a known time interval that encompasses one or more complete recurrence periods. We report both slip rate calculations and discuss the relative applicability of each.

4 Results

Our mapping provides several lines of evidence that the BRF is Quaternary-active, and has experienced multiple slip events since the late Pleistocene. Field mapping of the morphology and spatial distribution of fault scarps (Figures 3 and 4) indicates that the mapped scarps are of tectonic origin, produced during one or more surface-rupturing earthquakes, and are not the product of glacial, gravitational, or anthropogenic processes. An active BRF is further supported by the presence of numerous right-laterally and vertically offset abandoned stream channels incised into Late Pleistocene to Holocene till and paraglacial deposits. Below we discuss the morphology of the fault scarps, the ages of offset deposits, the kinematics of fault slip derived from measured offsets of channel networks, and our interpretations of the number and relative timing of events that have occurred along the BRF since the last glacial maximum.

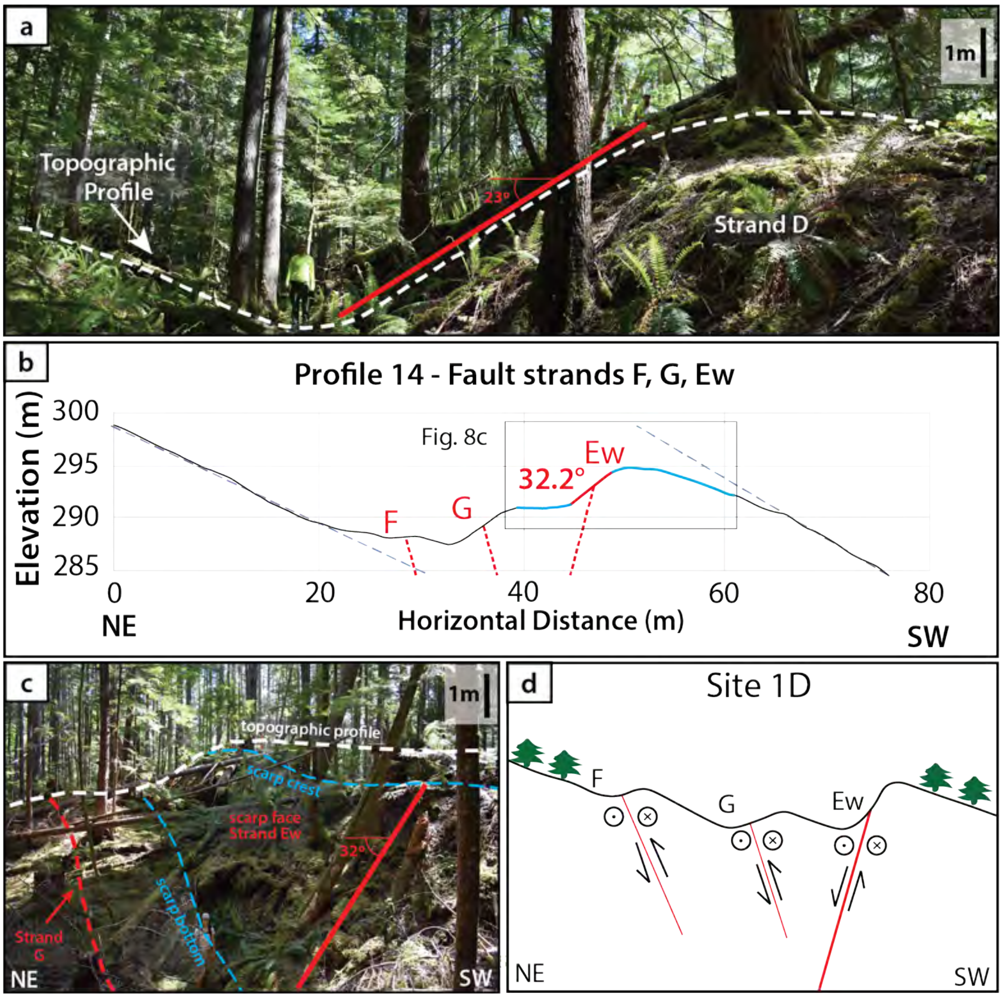

Figure 8. Examples of fault scarps identified along the Beaufort Range fault. **A:** Tall, uphill-facing, moderately steep (∼23°) fault scarp along strand D at Site 1D (Figures 4b, 5a). **B:** Topographic profile across three scarps at Site 1D associated with fault strands F, G, and Ew extracted from bare-earth lidar DEM (Profile 14, Figure 5). Dashed dark blue lines show the projection of the background hillslope toward the scarps. **C:** Photo of the tall, steep preserved face of Strand Ew shown in the topographic profile in panel b. The uphill-facing fault scarp along strand Ew is ∼32°, nearly angle of repose, much steeper than the scarp face along strand D (panel a). **D:** Cartoon cross-section showing the schematic relationships between sets of sub-parallel and en echelon fault strands, based on observations at Site 1D. These strands are interpreted to merge at depth in a flower structure consistent with strike-slip faulting.

4.1 Quaternary fault scarps

Our mapping shows that the Quaternary-active BRF is defined by a series of sub-parallel, discontinuous fault scarps (n=153) that offset multiple ages of Quaternary deposits preserved on the southwestern flank of the Beaufort Range (Figure 2a, Figure S1). The spatial distribution of preserved scarps shows they are part of an ~500 m wide fault zone, where slip is distributed across multiple (~1-6) sub-parallel, steeply-dipping fault strands (Figure 8, Figure S1). Individual fault scarps locally exhibit strike lengths of ~100-1500 m, exhibit scarp heights of ~0.5-6 m, and occur in en echelon or parallel sets with intra-fault spacings of 5-100 m. Scarp facing directions can vary locally over short distances but about two thirds of the scarps (n=101) face NE. Most (~70%) of the mapped faults have asymmetric cross-sectional morphologies with steep uphill-facing scarps, while a smaller fraction are preserved as flat, degraded topographic features embedded in the high-gradient hillslopes (Sites A-E; Figures 3, S2, S4). Our mapping demonstrates that active fault strands generally strike NW, parallel to the range (average ~287°, with variation of up to 20°-38°), and our topographic field surveys (see Section 3.2.2) indicate that near the surface, most strands dip steeply NE (~60°-88°), with a few dipping steeply SW (~70°).

The steepness and morphology of the scarp faces vary both along strike and between strands. At Site 1, the steepest and tallest scarps are 4-6 m tall and have scarp faces near the angle of repose (32° strand Ew at Site 1D; Figures 5, 8). Many of the scarps at Site 1 exhibit steep, well-preserved free faces, such as strand Ew at Site 1D (Figure 8b-c). Other scarps at Site 1 exhibit a more moderate, 24° dipping scarp face (Figure 8a), such as Strand D at Site 1D. At Site 2, the scarps are 1-3 m tall and have faces near the angle of repose (~45° strand U at Site 2A; Figures 6 and S5), and some are large and steep enough to have effectively ponded large boulders sourced from uphill (Figure S5). Several of the individual scarps at Site 1 are part of a larger, multi-fault scarp that includes multiple emergent fault strands (Figure 8b), whereas individual scarps at Site 2 appear to occur as separate parallel or anastomosing fault sets (Figure 6).

Our mapping shows that the majority of active fault scarps are not directly co-located with known bedrock fault planes at the surface (Figures 4 and S1). At Site 2, the primary bedrock thrust fault, which places Karmutsen Fm basalts over Nanaimo Gp sediments (Figure 4a), is exposed as a 200+ m wide damage zone that juxtaposes hanging wall basalts against an upright, open, footwall syncline of Nanaimo Gp sandstones. Mapped

Quaternary fault scarps do not appear co-located with the exposed bedrock fault plane at the surface, but instead occur in sub-parallel networks spanning up to 500 m away, in both the hanging wall and footwall. Similarly, at Site 1 where the bedrock thrust branches into two strands, mapped Quaternary faults occupy a zone that is ~500 m wide, and occur up to 500 m away from mapped bedrock thrust faults (Figure 4b).

Quaternary fault scarps also have different slip senses and attitudes than observed along the bedrock thrust faults. Slickenlines and Riedel shear geometries (Figure S7) on Eocene bedrock thrust faults indicate apparent NE-side-up, dominantly dip-slip displacement, whereas the active faults exhibit southwest-side-up and right-lateral displacements (Figure S7). Outcrop exposures of the bedrock thrust fault at both Site1 and Site 2 exhibit strike orientations that differ from Quaternary scarps by ~15°. Our field surveys indicate that the active fault BRF strands have dips of 70°-90° NE, whereas exposures at several sites along the range suggest the inherited thrust fault has a dip of <40° NE to sub-vertical. These observations indicate that mapped active fault scarps are not produced by slip along inherited structures in the near subsurface, but instead occupy a zone that is generally sub-parallel to the inherited structure.

4.2 Quaternary mapping and stratigraphy

Quaternary fault scarps along the BRF displace a series of nine units that were deposited during the late Pleistocene to Holocene deglaciation and subsequent transition to a post-glacial environment. We develop a local Quaternary stratigraphy (Figure 4 and Table S1) that groups these deposits into three categories: ice-contact glacial units deposited during the most recent glaciation, paraglacial units deposited during ice retreat and slope readjustment, and post-glacial units deposited after ice retreat.

4.2.1 Ice-contact glacial deposits and landforms

The ice-contact glacial units are the oldest and stratigraphically lowest Quaternary units mapped in the study area and include subglacial till (Qt), kame terraces (Qk), and hummocky moraine (Qhm) (Figure 4; Table S1). The subglacial till (Qt) is a very indurated, matrix-supported diamict containing both locally-derived and exotic clasts and is up to 40 m thick. Qt mantles bedrock along the southwestern flanks of the Beaufort Range mountain front at elevations >150-400 m. Kame terraces (Qk) occur as a series of five evenly-spaced, flat-topped terrace treads with steep risers, at 150-300 masl (<150 m above the valley floor), underlain by indurated, poorly to moderately sorted, stratified sands and gravels. Hummocky moraine (Qhm) is present on the valley floor at elevations of <150 masl at Site 1.

4.2.2 Paraglacial deposits and landforms

Glacial deposits are overlain by two generations of paraglacial deposits, Qp1 and Qp2 (Figure 4c; Table S1). Qp1 consists of indurated, clast-supported, poorly-sorted, stratified sands and gravels. Qp1 deposits occur as cone-shaped landforms whose heads merge into Qt and whose toes are buried by Qp2 at the foot of the range. Qp2 has a similar composition to Qp1 and consists of thinly-bedded, clast-supported, stratified sands and gravels with occasional coarse sand lenses. Qp2 is distinguishable from Qp1 based on inset and burial relationships and its position at lower elevations on the range front.

Qp1 is incised by a series of abandoned channels. These channels are disconnected from active streams but merge into the heads of Qp2 deposits, suggesting that they were active at the time of deposition of Qp2. Abandoned channels at Site 1 are typically ∼1-4 m deep, have V-shaped cross-sectional morphologies and are separated by adjacent interfluves with linear ridges and steep flanks, or are incised into till and colluvium-mantled hillslopes (Figures 3 and 4). We interpret these abandoned channels to have formed as the result of fluvial and debris flow scouring and filling associated with the deposition of Qp2. At Site 2, offset abandoned channels have broad cross-sectional morphologies and are moderately incised into hummocky, till-mantled hillslopes (Figures 3 and 4). These channels do not clearly merge into other mapped deposits but appear to be cross-cut by younger landslides at the foot of the range.

4.2.3 Post-glacial units and landforms

The youngest units include post-glacial landslides (Qls), scree fans (Qsf), alluvial fans (Qaf), and fluvial terraces (Qft1 and Qft2) that either bury or are inset into the glacial and paraglacial deposits (Figure 4, Table S1). Mapped landslides (Qls) are hummocky deposits associated with curvilinear headscarps and oversteepened toes and have widths of 50-600 m. Scree fans (Qsf) are small (30-250 m across), fan-shaped deposits with rough surfaces that contain cobble to boulder-sized bedrock clasts. Qsf occurs at the bases of mapped bedrock exposures at elevations of ∼750 masl. Alluvial fan deposits (Qaf) are defined as a series of broad, convex, gently-sloping fans headed in active or recently-active channels (Figure 4). The fans consist of poorly to moderately sorted, clast-supported, stratified alluvial and fluvial deposits containing silt, sand, pebbles, and boulders, with occasional clast imbrication and cross-bedding (Table S1). Qaf deposits are mapped at the base of the range front and bury portions of Qp2, Qt, and Qhm.

At two locations in Site 2, and one at Site 1, Qaf fan heads merge into deeply incised (by ∼1-15 m) streams that are flanked by a series of up to five fluvial terraces (Qft1 and Qft2). Fluvial terrace treads are 20-130 m wide, slope gently downstream, and have risers up to 5-10 m tall. The deposits that underlie these terraces are moderately to well-sorted, clast-supported sediments, with sub-horizontally stratified interbeds of rounded cobbles, boulders, and pebbles. We subdivide these fluvial terraces into two generations (Qft1 and Qft2) based on the inset relationships observed at Sites 1 and 2. At Site 2, Qft1 terraces are inset into till-mantled bedrock and are, in turn, incised by channels feeding Qaf alluvial fans (Figure 4b). This observation shows that at Site 2, Qft1 terraces are older than Qaf. In contrast, at Site 1, Qft2 appears to grade into the channels that feed Qaf, indicating that Qft2 terraces are younger than at Site 1 and are instead correlative to upper portions of Qaf or the channels inset into Qaf (Figure 4a).

4.2.4 Radiocarbon results and inferred unit ages

We use radiocarbon ages from detrital charcoal extracted from Quaternary deposits to place brackets on the possible ages of mapped units offset by BRF scarps. We note that the interpretation of detrital charcoal radiocarbon dates can be challenging due to vertical mixing during bioturbation or soil creep, recycling of older charcoal into younger deposits, and bias from younger carbon (e.g., roots) included in older charcoal. However, the radiocarbon ages that we obtained from Quaternary units in the map area are in broad agreement with our local relative Quaternary stratigraphy (Figure 4) and with regional constraints on the timing of deglaciation and post-glacial processes (e.g., Halsted, 1968; Alley & Chatwin, 1979; Blaise et al., 1990; Clague, 1994). We use these data, therefore, to make the following interpretations of unit ages.

The three ice-contact glacial deposits, Qt, Qk, and Qhm, were barren of charcoal and could not be directly dated (Table 1). This absence is consistent with other studies on Vancouver Island that have found ice-contact deposits to be devoid of charcoal (Morell et al., 2018; Harrichhausen et al., 2021). We interpret Qt, Qk, and Qhm to be associated with the last glacial maximum, which has been regionally dated to ∼11.5-13.6

ka (Halsted, 1968; Alley & Chatwin, 1979; Blaise et al., 1990; Clague, 1994), although we recognize the possibility that deposits associated with prior glacial periods may be present in the study area.

We attempted to radiocarbon date both Qp1 and Qp2 debris-cone fan deposits, but only Qp2 yielded datable charcoal. The charcoal sample was collected from a stratified fan deposit ~30 cm below the surface of Qp2 (BR18-09C), in a roadcut exposure located ~250 m SW of the fault scarps at Site 1 (Figure 4, Figure 3). This sample yielded an age of ~9.5 cal ka (Table 1), consistent with the older estimated age of the Late Pleistocene glacial deposits (Qt, Qk, and Qhm) of ~11.5-13.6 ka, and younger radiocarbon ages of samples from Qaf and Qft2 (see below). The ~9.5 cal ka age is also broadly consistent with the timescales of paraglacial debris cone formation documented in recently deglaciated terrains that suggest these types of deposits form in the first 100s-1000s of years following deglaciation (Ryder, 1971; Ballantyne & Benn, 1996; Ballantyne, 2002).

Post-glacial units Qaf and Qft2 also yielded datable macro-charcoal fragments. Qaf yielded one macro-charcoal sample (BR18-08C). This sample was collected from a stratified, clast-supported sand lens within interbedded sands and gravels ~0.75 m below the top of the deposit located ~500 m SW of fault scarps at Site 1 (Figure 4 and 3). This sample yielded a radiocarbon age of ~6 cal ka (Table 1). Qft2 yielded a charcoal sample (BR18-42C) sieved from bulk sediment collected from a stream cut exposure of stratified pebbles and cobbles, located <10 m downhill from mapped fault strand Ee (Figure 4b, Figure 3). This sample yielded a radiocarbon age of ~3.5 cal ka (Table 1). Both ages are younger than the ages determined from a radiocarbon sample from paraglacial deposit Qp2 (~9.5 cal ka), and agree with our stratigraphic interpretation that Qaf is older than Qft2.

If we assume that these samples reflect deposit ages, and are not significantly altered by recycling, bioturbation, or inclusion of younger carbon, these data suggest the following as possible brackets on the ages of mapped deposits. Qt, Qk, and Qhm are likely ~11-14 ka, paraglacial deposits Qp1 and Qp2 are likely ~6 to ~11 ka, Qaf units are likely ~3 to ~9 ka, and Qft2 deposits are likely <4 ka. Given the uncertainties inherent with this method and with the small number of samples available for dating, we treat these as age approximations.

Table 1. Radiocarbon sample data at Site 1D (see Figures 4b and 4c for locations).

Unit[a]	**Coordinates**[b]	**Sample Name**	**Sample Type**	**Dated Material**	**UCIAMS ID**[c]	**Fraction Modern**	**D14C (‰)**	**Radiocarbon Age**[d] **(years BP, 2 σ)**	**Calibrated Age**[e] **(cal BP)**
Qft2	364944 E, 5466432 N	BR18-42C	Bulk sediment	Charcoal (single piece)	215248	0.6658 ± 0.0013	-334.2 ± 1.3	3265 ± 20	3560-3400
Qaf	364561 E, 5465854 N	BR18-06C	Macro charcoal	Not dated	–	–	–	–	–
		BR18-07C	Macro charcoal	Not dated	–	–	–	–	–
		BR18-08C	Macro charcoal	Charcoal (single piece)	215248	0.5185 ± 0.0010	-481.5 ± 1.0	5275 ± 20	6180-5940
Qp2	364400 E, 5466402 N	BR18-09C	Bulk sediment	Charcoal (composite of three pieces)	215249	0.3428 ± 0.0008	-657.2 ± 0.8	8600 ± 20	9600-9520
	0364683E, 5466207N	BR18-10C	Bulk sediment	barren	–	–	–	–	–
Qp1	0365209E, 5466352N	BR18-11C	Bulk sediment	barren	–	–	–	–	–
	0364515E, 5466653N	BR18-12C	Bulk Sediment	barren	–	–	–	–	–

[a] See Figure 4 and Table S1

[b] NAD83 UTM Zone 10

[c] Samples were prepared at PaleoTek Services. Sample preparation backgrounds have been subtracted, based on measurements of ^{14}C-free wood. These samples were treated with acid-base-acid (1N HCl and 1N NaOH, 75°C) prior to combustion. Samples were processed at the UC Irvine Keck AMS facility.

[d] All results have been corrected for isotopic fractionation according to the conventions of Stuiver and Polach (1977), with $d^{13}C$ values measured on prepared graphite using the AMS spectrometer. These can differ from $d^{13}C$ of the original material, and are not shown.

[e] Radiocarbon ages calibrated using INTCAL20 (Reimer et al., 2020) and OxCal v. 4.4 (Bronk Ramsey, 2021). Range reported represents unmodeled 95% confidence interval as calculated by OxCal.

4.3 Fault offset measurements

Results of our field mapping and topographic surveys show that the BRF has accommodated several meters of vertical and right-lateral displacement, distributed over a network of one to six fault strands that offset the mapped late Pleistocene to Holocene deposits (Figure 3). At Site 1 (Figure 5), scarp heights on individual fault strands range from 0.5 to 6 m, and channels appear in the field to be right-laterally offset by ∼0.5-2 m. These observations suggest cumulative displacements of several meters across multiple fault strands. Similarly, at Site 2, scarp heights range from 1 to 3 m, and a series of three stream channels visible in lidar appear to be systematically right laterally sheared by several meters across three to five fault strands (Figure 6). Our field observations and survey data also show that scarp heights in older deposits and landforms, including the interfluves developed in Qp1 at Site 1 and the till-mantled hillslopes at Site 2, have larger vertical displacements than the younger channels incised into these deposits, suggesting the potential for multiple events.

4.3.1 Slip vectors and fault kinematics

Estimates of slip based on our topographic survey data confirm our field observations that the BRF exhibits consistent right-lateral and dip-slip offset of the ground surface. Oblique slip magnitudes across individual fault strands range from ∼2 to 7 m at Site 1 and from ∼2 to 5 m at Site 2 (Table S2). Average dip-slip magnitudes for single faults range from ∼1 to 5 m, with the largest dip-slip magnitudes of up to ∼9 m observed at Site 1D (Table S2). Average right-lateral strike-slip magnitudes recorded in offset channels and interfluves at Sites 1 and 2 range from ∼1 to 5 m. Displacements of piercing lines across individual strands yield a ∼0.3:1 to 1.5:1 ratio of strike slip to dip slip, similar to those yielded by the cumulative displacements (Table S2). These data suggest that, while the fault system as a whole accommodates approximately equal magnitudes of strike slip and dip slip, some individual fault strands are dominated by dip slip, while others are dominated by strike slip.

Kinematic inversions of BRF slip vector data produce pseudo focal mechanisms that similarly indicate right-lateral transtension along a steeply NE-dipping fault (Table S3). Inversions performed for Sites 2A, 1C, 1D, and 1E (Figure 9 a-d) show small variations in the average strike and dip of the primary slip plane of 292-321° and 66-78°, and in the average trend (095-153°) and plunge (10-26°) of the model slip vectors. These site-specific

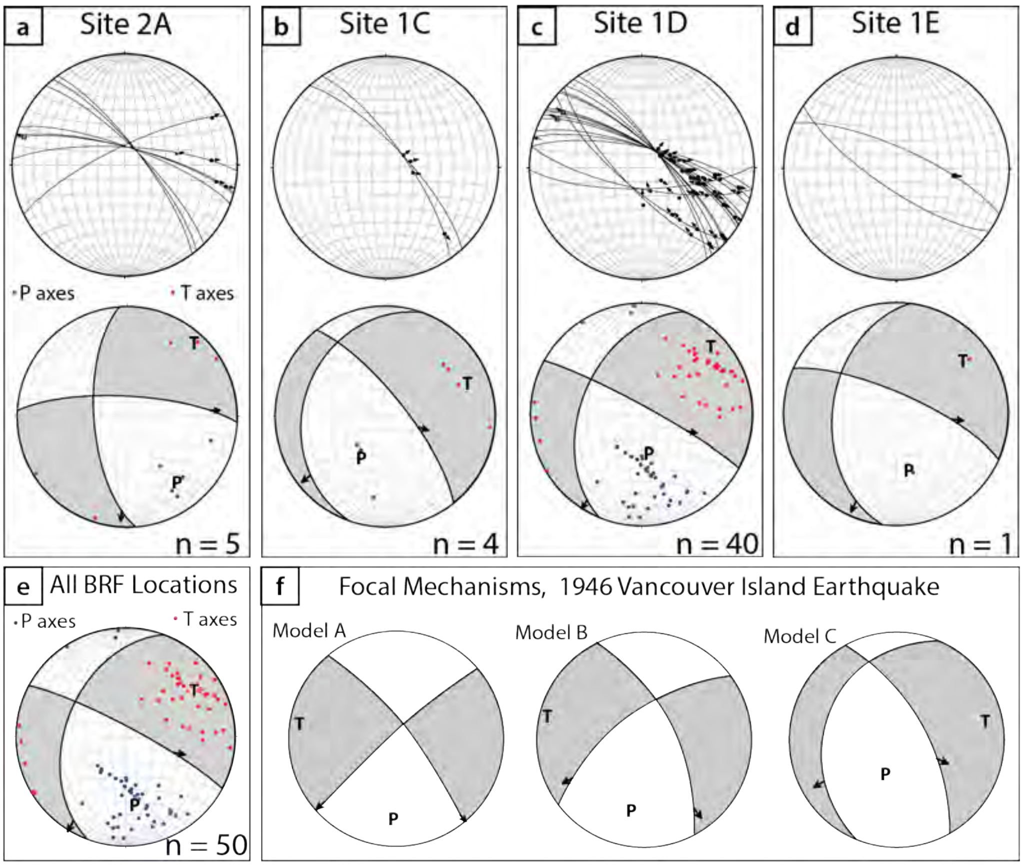

Figure 9. Right-lateral transtension along the Beaufort Range fault demonstrated by slip vectors and pseudo focal mechanisms produced from kinematic inversions. **A-D:** Kinematic data at four sub-sites along the BRF (see Figure 4 for locations). Upper panels: Lower hemisphere equal area projections showing fault planes, slip vectors, and hanging-wall motions. Lower panels: P- and T-axes and linked Bingham fault plane solutions (lower) for faults at locations 2A, 1C, 1D, and 1E. These slip vectors and kinematic inversions are consistent with right-lateral oblique motion on NE-dipping planes. **E:** Composite kinematic inversion for all surveyed sites along the BRF. Lower hemisphere equal area projection showing P- and T-axes and linked Bingham fault plane solutions. **F:** Focal mechanism solutions for the 1946 M 7.3 Vancouver Island earthquake (Rogers & Hasegawa, 1978, see Figure 2a for epicentrallocation). Model A is Rogers and Hasegawa's preferred model. Note the similarity in orientations of nodal planes and P- and T-axes for BRF fault kinematics.

inversion data are similar to full fault inversions, and indicate an approximate slip trend and plunge of ∼110/45 along an ∼80° NE dipping fault plane. These full-fault pseudo focal mechanisms yield local P- and T-axes with trends and plunges of 170/37 and 058/26 respectively.

4.3.2 Cumulative displacements

At Site 1, available exposures allowed us to calculate cumulative displacement across one to three strands for 14 interfluves developed in Qp1 and 9 channels incised into Qp1 (Figure 5). These data show that cumulative oblique slip at Site 1 measured in offset interfluves and channels ranges from ∼4 to 21 m (Figure 6). At Site 2, cumulative displacement of channels incised into Qt was summed across two to four mapped strands showing cumulative slip magnitudes of ∼4 to 13 m (Figure 6). We note that cumulative oblique slip magnitudes at Site 2 are likely underestimated, given that it was only possible to determine cumulative displacement across a portion of the mapped strands due to limited exposure and preservation.

Our calculated vertical and oblique displacement magnitudes show that older deposits typically record greater amounts of displacement than younger deposits. Examples of this relationship can be observed in the comparison of vertical separation along adjacent profiles at Sites 1 and 2 (Figure 10). At Site 1 (strand D, Figures 5, 10a) there is 5.8 m of vertical separation across an offset interfluve developed in Qp1, the oldest offset deposit at the site, whereas the adjacent, younger abandoned channel shows only 4.7 m of vertical separation. A younger Qft2 fluvial terrace, which crosses adjacent fault strand Ee, has even less vertical separation (2.3 m). Similarly, at Site 2, we find that the till-mantled hillslope typically has larger vertical separation than channels incised into till. For example, profile 28 at Site 2 in Qt shows 4.1 m of vertical separation across strand Q, whereas profile 33 along a younger channel incised into Qt shows only 2.9 m of vertical separation (Figures 6, 10b). Finally, we were able to expand this assessment of cumulative displacement to a set of 23 interfluves and channels at Site 1 for which we are able to reconstruct 3D displacement. These data show that older interfluves developed in Qp1 consistently have ∼4 to 10 m more cumulative oblique displacement as compared to young channels incised into Qp1 (Figure 10c).

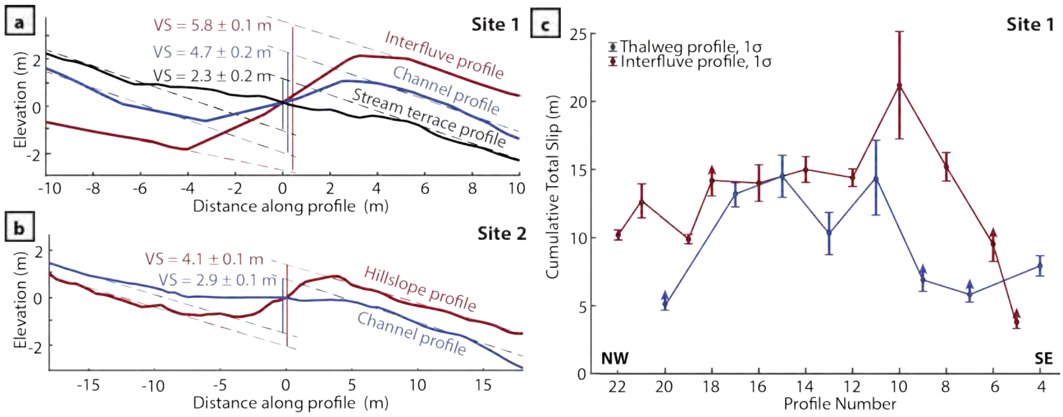

Figure 10. Topographic survey data showing differential magnitudes of fault offset in deposits of different ages. **A:** Example from Site 1D where there is the largest magnitude of vertical separation across an interfluve developed in Qp1 (profile 10, strand D), intermediate magnitudes across a channel incised into Qp1 (profile 11, strand D, channel age correlative to deposit Qp2), and minimum magnitudes across a Holocene stream terrace (profile 3, strand Ee). **B:** Example from Site 2A where there is greater vertical separation across the till mantled hillslope (profile 28, Qt,), and smaller separation across a channel incised into till (profile 33, strand Q). **C:** Cumulative slip estimates from Site 1D profiles: cumulative slip across interfluves (mean = 12.7 ± 4.4 m) is greater than for thalwegs (mean = 9.8 ± 3.9 m), suggesting interfluves have experienced at least one more event than thalwegs. Arrows indicate minimum slip estimates in locations where displacements across one or more strands could not be reconstructed.

5 Discussion

5.1 Characteristics of the Quaternary-active BRF

The field data and observations provided in this paper provide unequivocal evidence that the scarps we identify along the southwestern flank of the Beaufort Range are tectonic in origin and are associated with an active Beaufort Range fault. Mapped scarps form en echelon steps, and parallel arrays exhibit geometries common in strike-slip fault systems and pull-apart basins (e.g., Hatem et al., 2017; van Wijk et al., 2017), and occur along several tens of kilometers of strike length. The magnitudes of displacement and total fault lengths are consistent with observed displacement-length scaling relationships for active faults in Cascadia (R. H. Styron & Sherrod, 2021), and globally (D. L. Wells & Coppersmith, 1994; Wesnousky, 2008).

The scarps are inconsistent with formation processes associated with gravitational failure, glacial, or anthropogenic processes, for several reasons. First, scarps are predominantly uphill-facing, and are associated with steep NE-dipping fault planes that produce "valley-side up" displacement. This sense of displacement is opposite to that predicted for landslide-related failures. Second, the scarps are quasi-linear and extend for several km along strike, whereas headscarps associated with landslides tend to produce curvilinear and discontinuous scarps with limited strike lengths. Third, the mapped scarps are inconsistent with formation by sackungen (McCalpin et al., 1999), which typically form sets of parallel scarps at range crests, rather than the en echelon scarps we observe near the base of the range (e.g., Figure 2b as compared to Figure 3c). Finally, our field observations also confirm that these scarps are not associated with roads, logging tracks, or other anthropogenic disturbances, nor are they associated with glacial scouring or glacially-streamlined deposits (see Supplemental Text S1).

Our data indicate that the BRF consists of a set of high-angle faults, with an average 60-88° NE dip, with local fault strand strikes ranging from ∼270° to 320°. While individual fault strands extend for several hundred m to several km, these strands collectively define a discontinuous network of scarps that we interpret to be the surficial expression of a single fault zone at depth. Such discontinuous fault scarp networks are common in strike-slip systems, especially in immature faults with little cumulative offset (e.g., Hatem et al., 2017), and have been observed along other forearc faults in northern Cascadia (e.g., Morell et al., 2017). The mapped network of BRF fault scarps identified in this study extends for ∼40 km from Port Alberni to Comox Lake (Figure 2b and 1). Additional potential scarps visible in lidar DEMs occur along strike of the active BRF outside the map area, suggesting that the BRF may have a cumulative length that is >40 km (Figure 1). If all of the mapped scarps in this study are associated with a continuous subsurface fault network, then the BRF is one of the longest strike-length faults identified in northern Cascadia to date.

5.2 Kinematics of the BRF and relationship to inherited structures

Our field mapping and topographic survey data demonstrate that the active BRF is a transtensional structure that accommodates right-lateral oblique slip along a steeply NE-dipping fault zone (Figure 9). Three lines of evidence support this interpretation: 1) Field observations show consistent right-lateral offset of abandoned channels and interfluves and net NE-side-down vertical displacement. 2) Slip vectors resolved by reconstructing piercing lines similarly indicate NE-side-down hanging wall motion, consistent with right-lateral transtensional slip on a steeply NE dipping fault (Figure 9). These kinematics are consistent with mapped fault scarp geometries that suggest formation during right-lateral transtension. For example, at Site 1 (Figures 5a, 8), there is an en echelon array of faults with opposing dips that is consistent with the map patterns expected for a right-lateral transtensional negative flower structure. 3) Pseudo focal mechanism inversion of slip vectors indicate that the BRF accommodates right-lateral transtension along a steeply NE dipping fault plane.

The NE-side-down slip sense we determine for the Quaternary-active BRF produces a "range-side down" sense of motion. This result suggests that the high elevations and steep topography associated with the southwestern flank of the Beaufort Range were not formed by transtensional slip along the active BRF. Instead, the steep range front may be the product of differential erosion of the softer Cretaceous Nanaimo Gp sediments that underlie the Alberni Valley, relative to the more resistant Karmutsen Fm basalts that underlie the range crest (Muller & Carson, 1969). Or, this may imply that the net range-side-down (NE-side down) motion integrated over 100s kyr to Myr across the active BRF may be small relative to the amount of Eocene NE-side-up thrust fault displacement. The small cumulative magnitude of NE-side-down motion could indicate that transtension across the BRF is a relatively young phenomenon, and has not accrued a large magnitude of vertical displacement.

Finally, our data suggest that active BRF strands do not appear to directly reoccupy inherited thrust fault planes. The presence of active BRF scarps in both the hanging wall and footwall of inherited thrust faults (Figure 4) suggest that there is not a strong inherited lithologic or mechanical control on the position of the active BRF at the surface. Furthermore, there is an apparent difference between the near-surface dip of the Quaternary-active BRF (70-90°) and that of the inherited Eocene Beaufort Range thrust fault (∼45-70°). There are two possible explanations for this apparent dip discrepancy. First, these observations could imply that the subsurface projections of the active and Eocene faults may diverge at depth. Similar discrepancies between active and inherited fault geometries have been observed in the northern Cascadia forearc along the Leech River and North Olympic faults (Morell et al., 2017; G. Li et al., 2017; Nelson et al., 2017; Schermer et al., 2021). These data suggest that it is possible that the active BRF may reflect the formation of a new fault, more optimally oriented in the forearc stress field, rather than slip on an inherited bedrock structure. The second possibility is that the dip of the BRF is steep near the surface, but has a more gentle dip at depth, such that the active transtensional fault follows the Eocene thrust fault at depth. The geometry, kinematics, and slip history of the active BRF therefore provide critical insight into the neotectonic stress and strain fields in the northern Cascadia forearc.

5.3 Evidence for multiple surface-rupturing late Pleistocene to Holocene earthquakes

Our tectonogeomorphic mapping, topographic surveys of offset abandoned channels and interfluves, and field observations of fault scarp morphology support the hypothesis that the BRF has hosted multiple earthquakes since the deglaciation of the Alberni Valley (∼14-11 ka). The strongest evidence for multiple events comes from the differential scarp heights and cumulative slip magnitudes calculated for offset landforms of different ages at Sites 1 and 2 (Figure 10). At Site 1, interfluve crests developed in the older paraglacial unit Qp1 have greater vertical separation (∼1 m) and greater cumulative oblique slip (∼1-3 m) than abandoned channel thalwegs incised into that same unit. These abandoned channels in turn have greater vertical separation (∼2.4 m) than the displacement surveyed across a younger Qft2 fluvial terrace. The differential offset between interfluves, channels, and fluvial terraces indicates the occurrence of at least three events since the deposition of Qp1 at Site 1. At Site 2, differential scarp heights of ∼2 m between those developed in till-mantled hillslopes and younger channels incised into the hillslopes indicate at least two surface-rupturing events have occurred at this site following the deposition of Qt. Furthermore, if we make the simplifying assumption that a single event produces ∼1-3 m of oblique slip, based on the average difference in cumulative oblique displacement between interfluves and channels, these data suggest the BRF may have hosted more than three events since ∼11-14 ka.

At Site 1, we can place broad constraints on the relative timing of slip events by combining our estimates of deposit ages (Table 1; Figure 4c) with offset magnitudes (Table S2; Figure 6). The timing of the first event is constrained by the observation that older interfluves developed in Qp1 have more cumulative oblique offset than channels developed in Qp1. This observation indicates that at least one event must have occurred more recently than the deposition of Qp1, which occurred after deglaciation (∼11-14 ka), but before the abandonment of channels incised into Qp1. The timing of channel abandonment is not directly dated, but our correlation of channel incision to the deposition of Qp2 suggests channel abandonment occurred after the deposition of Qp2 (radiocarbon dated to ∼6 to 11 ka) and before the deposition of Qaf (radiocarbon dated to ∼3-6 ka). Therefore, the first event(s) likely occurred after ∼11-14 ka, but before ∼3-6 ka. The timing of the second event is constrained by the difference in offset between channels and inset Qft2 terraces. This difference requires one or more events to have occurred after channel abandonment (which we infer occurred after 6-11 ka), but before the formation of the Qft2 terrace (radiocarbon dated to <∼4 ka). The occurrence of a third event is supported by the ∼1.5 m of vertical offset of the Qft2 terrace. Therefore, the most recent event must have occurred after the deposition of the Qft2 terrace (since ∼4 ka).

These data suggest that the BRF has experienced at least three events over the late Pleistocene to late Holocene. The persistence of right-lateral transtensional deformation along the BRF for several thousand years after the retreat of glaciers from the Alberni Valley indicates that deformation cannot be attributed solely to changes in crustal loads and stresses due to glacial unloading and viscoelastic relaxation of the crust and mantle (e.g., Anderson et al., 1989; Craig et al., 2016; Davenport et al., 1989; Lagerbäck, 1990; Mörner, 1991; Muir-Wood, 2000; Jarman & Ballantyne, 2002; van Loon et al., 2016). Such "glacially-induced" earthquakes typically occur during or within a few kyr of glacial retreat, when changes in ice loads and crustal stresses from the viscoelastic rebound are greatest (Steffen et al., 2014). While our data do not constrain the precise timing of the first event(s), and cannot rule out that early events on the BRF were impacted by glacial unloading, they do indicate earthquakes have occurred in the middle to late Holocene, well after the largest stress changes due to glacial loading would have occurred. Additionally, we note that glacial unloading typically reduces vertical stress, and given that our slip data indicate the BRF accommodates transtension, such unloading would reduce the deviatoric stress making failure less likely. Overall, the persistence of right-lateral transtensional events throughout the Holocene suggests that tectonic forces are the principal drivers of deformation, and any glacial impacts are secondary.

Our estimates of displacement per event, and measurements of the total length of the active BRF from mapped or inferred fault scarps, allow us to estimate the magnitude of paleo-earthquakes at these sites using displacement scaling relationships. An estimated ~1-3 m of displacement per event suggests that the BRF could have hosted M_W 6.9 to 7.2 events (D. L. Wells & Coppersmith, 1994). These magnitudes are similar to those determined based on our total mapped fault length of 35 to >40 km, which suggests M_W 6.8 to >7.0 events (D. L. Wells & Coppersmith, 1994; Wesnousky, 2008). These earthquake magnitudes are similar in scale to the M 7.3 magnitude calculated for the 1946 Vancouver Island earthquake, which caused significant damage, including to telephone wires, underwater telegraph cables, and the hospital in Port Alberni, BC (Hodgson, 1946). An earthquake of a similar magnitude today would pose significant hazard not only to Port Alberni, but also to the nearby communities of Nanaimo, Parksville, Qualicum Beach, and Courtenay (Figure 2a). Failure of dams on Comox Lake and Elsie Lake could lead to flooding of communities downstream (Figure 2b), as well as impacts on power availability, as nearby power stations supply 11% of the electricity generated on Vancouver Island (BC Hydro, n.d.).

5.4 Estimate of Late Pleistocene to Holocene slip rates

Estimation of fault slip rates yields important information relevant to understanding how strain is partitioned among faults, and they represent primary data used in seismic hazard analyses (Morell et al., 2020). Ideally, slip rates are calculated when at least two precise earthquake ages and the displacement associated with the bracketed event are known (e.g., a closed interval slip rate, DuRoss et al., 2020) and estimated over a time period spanning more than 5 earthquakes (R. Styron, 2019). In the absence of precise earthquake ages, a geomorphic slip rate can be estimated that affords an estimate of the slip rate that has accrued since the development of the geomorphic feature, using estimates of the date of the landform and displacement data recorded in the geomorphic feature. However, such an open-interval slip rate can be biased because the age of the geomorphic feature can differ from the age of the earthquake that deformed the feature.

On the BRF, we currently do not have precise earthquake ages, and we do not know the displacement between earthquakes with precision. However, we nonetheless make broad estimates of slip rate based on the known ages and displacements between known events. The cumulative displacement of different deposits, their depositional ages, and our estimates of event timing, place bounds on fault slip rates for the active BRF. Both open-ended and closed interval approaches at Site 1 yield slip rates for the BRF that range from ∼0.5 to ∼2 mm/yr. The open-ended approach yields a rate of ∼0.7-1.3 mm/yr, based on the ∼10 to 15 m of cumulative oblique slip across all mapped fault strands and an estimated deglaciation age of ∼11.5-13.6 ka. There is only one reliable closed interval calculation that can be made given the available offset data and uncertainties in event timing. This interval calculation uses the ∼8-9 m cumulative displacement of the channels at Site 1, and the difference in age between the Qft2 terrace and the interfluves at Site 1, which could range from ∼3.5 to 13.6 kyr. This closed interval spans at least two events, and yields a slip rate estimate of 0.6-2.6 mm/yr. Given the uncertainties in the ages of events and displacement magnitudes in this closed interval calculation, we prefer the more conservative open-ended rate of 0.7-1.3 mm/yr.

These data demonstrate that, even at the lower bound of uncertainty, the Beaufort Range fault is one of the fastest-slipping Quaternary faults in the northern Cascadia forearc. Our slip rate estimates of ∼0.5 to ∼2 mm/yr indicate that the BRF has a higher slip rate than the nearby LRF (0.2-0.3 mm/yr; Morell et al., 2017, 2018) and Darrington-Devils Mountain fault zone DMF (0.14 ± 0.1 mm/yr; Personius et al., 2014), and a similar slip rate to the NOFZ (1.3-2.3 mm/yr, 3-5 post-glacial earthquakes; Schermer et al., 2021). These data suggest that the BRF is a major crustal structure that accommodates permanent deformation in the northern Cascadia forearc.

5.5 Comparison of the 1946 Vancouver Island earthquake kinematics with slip on the BRF

The field data reported here cannot constrain the timing of the most recent event along the active BRF beyond that it occurred after ~3.5 ka, and therefore cannot directly test whether the 1946 event ruptured along the BRF within our field area. However, our data from the Holocene BRF share striking similarities to the kinematics, spatial distribution, and fault plane solutions for the 1946 event.

The pseudo-focal mechanism solutions for the BRF determined from kinematic inversions of fault slip have similar slip planes, slip vectors, and P- and T-axes as those determined for the 1946 Vancouver Island earthquake (Figure 9). Focal mechanism solutions for the 1946 earthquake (Rogers & Hasegawa, 1978) have NW-SE striking nodal planes with strikes of 319-332° and dips of 66-79°, and SW-NE striking nodal planes with strikes of 222-233° and dips of 36-85° (Figure 9f, Table S3). These nodal plane attitudes are strikingly similar to the nodal planes of the pseudo-focal mechanisms solutions derived from fault slip vectors along the active BRF (Figure 9). The NW-SE nodal plane of the focal mechanism preferred by Rogers and Hasegawa (1978) of 319/79 NE is subparallel to our calculated attitude of the active BRF of ~270-320/~75, and the predicted slip vectors associated with the NW-SE striking nodal planes for the 1946 earthquake have trends ranging from 114 to 143°, and plunges ranging from 05° to 55°—similar slip vector orientations to those determined from offset piercing lines along the active BRF. Finally, the stress axes determined for the 1946 focal mechanism solutions have moderately plunging, southerly trending P-axes and sub-horizontal T-axes with trends similar to those determined for the active BRF (Figure 9).

The fault slip vectors and transtensional pseudo-focal mechanisms that we determine for the BRF are also similar to fault plane inversions based on geodetic motions associated with the 1946 earthquake (Slawson & Savage, 1979). Repeat surveys of topographic benchmarks across the Beaufort Range at the latitude of the earthquake epicenter (~49.45° N) suggest right-lateral oblique slip on a steeply (70°) NE-dipping fault plane that extended for 60 km along strike (Slawson & Savage, 1979). Our mapped Sites 1 and 2 along the BRF therefore lie within the modeled event rupture area, and the fault plane dip is similar to the 60-88° NE dip we determine for the BRF. In addition, slip inversions for the 1946 event fault planes indicate the crustal displacements are best reproduced by ~1 m of right-lateral and ~2 m dip slip, along 60 km fault length parallel to the BRF. Therefore, both the relative ratio of strike slip to dip slip (∼0.5:1) and the estimated slip per event (∼1-2 m) modeled for the 1946 event are similar to our slip ratios of 0.3-1.5:1 (strike slip to dip slip) and estimates of ∼1-3 m of oblique slip per BRF event.

These data collectively indicate that the Holocene slip observed along the active BRF is kinematically and spatially compatible with the slip inferred for the 1946 Vancouver Island earthquake. These correlations suggest that, if the 1946 event failed along a NW-SE striking, steeply NE-dipping plane, as suggested by Rogers and Hasegawa (1978) and Slawson and Savage (1979), the BRF is a likely candidate for hosting this event. Our estimated age of the most recent event of <3-4 ka allows for this possibility. Furthermore, our field offset data provide evidence that the active BRF has hosted at least 3 earthquakes since the late Pleistocene, each with slip that is compatible with that modelled for the NW-SE striking nodal plane for the 1946 event. These observations suggest then that the BRF hosted multiple 1946-like events over the late Pleistocene to Holocene.

5.6 Implications for forearc strain accommodation

These results have several key implications for the long-term permanent strain accumulation in the northern Cascadia forearc. First, our field data and kinematic inversions for the active BRF indicate that this portion of the Cascadia forearc has experienced right-lateral transtension over the past ∼11-14 ka. In addition, the similarity between the fault kinematics integrated over multiple paleoseismic events spanning the late Pleistocene to Holocene and the 1946 Vancouver Island earthquake suggests that these transtensional kinematics are representative of the local upper plate deformation field over decadal to millennial time scales. If true, these time scales would span multiple upper plate fault seismic cycles, which likely have recurrence intervals of 1000s of years (e.g., Morell et al., 2018; Schermer et al., 2021), and multiple subduction interface megathrust seismic cycles, which have recurrence periods of ∼390-540 years (e.g., Walton et al., 2021).

Second, the slip kinematic inversions for the active BRF suggest that the P- and T-axes inverted for long-term (late-Pleistocene to present) slip are consistent with regional stress patterns derived from historical seismicity (Figure 2a; Balfour et al., 2011). We find that the trends and plunges of P- and T-axes determined for the BRF are within ∼20-40° of the P- and T-axes determined for the 1946 Vancouver Island earthquake and from inversions determined from nearby upper plate seismicity (Balfour et al., 2011). Several studies have suggested that variations in trench-perpendicular tractions during the megathrust seismic cycle can cause inversions in principal stress orientations in the overriding plate, such that forearc fault slip sense can vary as a function of the megathrust seismic cycle (e.g., Wang et al., 1995; Loveless et al., 2010; Regalla et al., 2017). However, the consistency of P- and T-axes determined from historical earthquakes and from paleoseismic slip suggests that BRF kinematics have not changed drastically over Holocene time scales. These data suggest that there is some level of consistency in the deformation field associated with short-term (decadal) upper plate seismicity and long-term (kyr-scale) fault slip, and a potentially similar temporal consistency in the upper plate stress field.

Third, a comparison between these BRF fault kinematics to those determined for other active faults in the northern Cascadia forearc, suggests that there may be a spatial transition from a forearc deformation field promoting right-lateral transpression near the Olympic Mountains and on southernmost Vancouver Island, to one promoting right-lateral transtension in the northern Cascadia forearc on central Vancouver Island. Specifically, the North Olympic fault zone, the Darrington-Devils Mountain fault, the Southern Whidbey Island fault, the Leech River fault, and the XEOLXELE~~K~~-Elk lake fault appear to be accommodating right-lateral slip and compression, as determined by earthquake focal mechanisms and paleoseismic data (Sherrod et al., 2008; Personius et al., 2014; Schermer et al., 2021; Morell et al., 2018; Harrichhausen et al., 2021, 2023). In contrast, at the latitude of central Vancouver Island, the BRF appears to be accommodating right-lateral transtension, as determined by kinematic inversions of offset geomorphic piercing lines across the BRF.

This observation suggests that there may be a change in the upper plate strain field from one favoring transpression on faults near the Olympic Mountains to one favoring transtension on faults in northern Cascadia, around the latitude of 48.5-49° N. This change in strain field may be related to spatial variations in principal stress orientations and magnitudes in the upper plate that locally promote transtension along the BRF. While the data presented here are not sufficient to determine the causes of this potential change in the upper plate deformation field, there are several possibilities, including oroclinal bending (Johnston & Acton, 2003; Finley et al., 2019; Harrichhausen et al., 2021), spatial changes in plate tractions, convergence rate, or obliquity (R. E. Wells et al., 1998;

Wang, 2000; McCaffrey et al., 2013; S. Li et al., 2018), or the 'escape' of forearc crustal blocks related to north-directed shear from southern Cascadia (Nelson et al., 2017). The consistency of fault kinematics and P- and T-axes calculated near the BRF from both seismic and paleoseismic data suggest that a deformation field favoring local right-lateral transtension has persisted over both decadal and millennial timescales.

6 Conclusions

We provide the first geologic field evidence that the Beaufort Range fault is a seismogenic fault, and demonstrate that it actively accommodates right-lateral transtension within the northern Cascadia forearc of central Vancouver Island. Field mapping and topographic surveys document >35-40 km of northwest-striking, primarily northeast-dipping fault strands along the southwestern flank of the Beaufort Range. These scarps occur in discontinuous, en echelon and parallel sets and offset late Pleistocene to Holocene glacial, paraglacial, and post-glacial deposits. We observe an increase in scarp height and total offset with increasing unit age that provides evidence for at least three surface-rupturing earthquakes on the BRF since ∼13.6-11 ka, the most recent of which occurred in the past ∼3-4 kyr. Slip magnitudes reconstructed from offset piercing lines, total fault length, and the ages of offset deposits suggest that the BRF is capable of hosting earthquakes of M_W 6.5-7.5, and has a late Pleistocene to Holocene slip rate of 0.5 to 2 mm/yr. Thus the BRF is a major forearc fault accommodating deformation in the northern Cascadia subduction zone, and poses significant hazard to communities and infrastructure on Vancouver Island.

Notably, kinematic slip inversions of geomorphic piercing lines offset by the BRF yield transtensional pseudo-focal mechanisms, fault geometries, slip vectors, and P- and T-axes that are remarkably similar to those determined for the 1946 Vancouver Island earthquake. These data suggest that the BRF is a candidate structure to have hosted this event. The consistency of right-lateral transtensional slip kinematics between the 1946 earthquake and late Pleistocene to Holocene slip on the BRF suggests that this portion of the northern Cascadia forearc has accommodated regional transtension over decadal to millennial time scales, spanning multiple earthquake cycles.

7 Open Research

New data produced in this study:

Data collected and analyzed in this manuscript are available in a Dryad Data Repository (Lynch et al., 2023) at
`https://datadryad.org/stash/share/Ui8KejoZgz41xslOZUxfCQV2Nea3JsVwQoTz9DZ1iho`.
The repository contains the following data:

1. Text files containing raw field data (x,y,elevation) of surveyed offset landforms
2. Text files containing raw field data (x,y,elevation) of fault midpoint locations
3. R script for calculating 3D fault plane geometry
4. R script for calculating 3D offsets of linear piercing lines across a dipping fault

Previously published data and programs used in this study:

1. The USGS Quaternary faults and folds database used for Figure 1 is available at `https://www.usgs.gov/programs/earthquake-hazards/faults`.
2. The BC Geological Survey (BCGS) bedrock geology map used for Figures 2a, 4, and Figure 1 is available at `https://www2.gov.bc.ca/gov/content/industry/mineral-exploration-mining/british-columbia-geological-survey/geology/bcdigitalgeology`.
3. The OxCal program v. 4.4 by C. Bronk Ramsey used for radiocarbon calibration is available at `https://c14.arch.ox.ac.uk/oxcal/OxCal.html`.
4. The R. Allmendinger FaultKin 7.6 program used for plotting and analyzing fault plane and slip vector data in Figure 9 is available at `http://www.geo.cornell.edu/geology/faculty/RWA/programs/faultkin.html`.
5. The OSX Stereonet 9.9.4 program used for plotting bedrock fault planes and slickenlines in Figure 7 is available at `http://www.geo.cornell.edu/geology/faculty/RWA/programs/stereonet.html`.

Acknowledgments

This work was conducted on the traditional territory of the Hupačasatḥ, K'ómoks, and ćišaaʔatḥ people, and we acknowledge their historical relationships with the land that continue to this day. Funding for this project was supported by NSF EAR Tectonics 1756834/2004684 to Regalla and 1756943 to Morell, by the Boston University Department of Earth and Environmental Sciences, and the Northern Arizona University Duebendorfer-Barnes Structure Endowment. We would like to thank Todd Thompson, TimberWest, and Island Timberlands for land access, and Mosaic/Island Timberlands/TimberWest for pro-viding lidar ground return data, as well as Edwin Nissen and the University of Victoria School of Earth and Ocean Sciences for discussion of local tectonics and help with field logistics. We would also like to acknowledge the late Vic Levson for help with understanding glacial systems of Vancouver Island, and Johanna Fischi and Tatum McLeod for assistance in the field.

References

AGI. (2003). *Global GIS: Volcanoes of the world.* https://earthworks.stanford.edu/catalog/harvard-glb-volc.

Alley, N. F., & Chatwin, S. C. (1979). Late Pleistocene history and geomorphology, southwestern Vancouver Island, British Columbia. *Canadian Journal of Earth Sciences*, *16*(9), 1645–1657.

Allmendinger, R. W., Cardozo, N., & Fisher, D. M. (2012). *Structural geology algorithms: Vectors and tensors in structural geology.* Cambridge University Press.

Anderson, W. A., Borns, H. W., Kelley, J. T., & Thompson, W. B. (1989). Neotectonic Activity in Coastal Maine. *Maine Geological Survey*, 195–212.

Angelier, J., & Mechler, P. (1977, January). Sur une methode graphique de recherche des contraintes principales egalement utilisables en tectonique et en seismologie : La methode des diedres droits. *Bulletin de la Société Géologique de France*, *S7-XIX*(6), 1309–1318.

Balfour, N. J., Cassidy, J. F., Dosso, S. E., & Mazzotti, S. (2011). Mapping crustal stress and strain in southwest British Columbia. *Journal of Geophysical Research: Solid Earth*, *116*(3), 1–11.

Ballantyne, C. K. (2002). A general model of paraglacial landscape response. *The Holocene*, *12*, 371–376.

Ballantyne, C. K., & Benn, D. I. (1996). Paraglacial slope adjustment during recent deglaciation and its implications for slope evolution in formerly glaciated environments. In *Advances in Hillslope Processes* (Vol. 2, pp. 1173–1195).

BC Hydro. (n.d.). *Our facilities: Vancouver Island.* https://www.bchydro.com/energy-in-bc/operations/our-facilities/vancouver-island.html.

Blaise, B., Clague, J. J., & Mathewes, R. W. (1990, November). Time of Maximum Late Wisconsin Glaciation, West Coast of Canada. *Quaternary Research*, *34*(3), 282–295.

Brocher, T. M., Parsons, T., Blakely, R. J., Christensen, N. I., Fisher, M. A., & Wells, R. E. (2001). Upper crustal structure in Puget Lowland, Washington: Results from the 1998 Seismic Hazards Investigation in Puget Sound. *Journal of Geophysical Research: Solid Earth*, *106*(B7), 13541–13564.

Brodzikowski, K., & van Loon, A. J. (1987). A systematic classification of glacial and periglacial environments, facies and deposits. *Earth Science Reviews*, *24*(5), 297–381.

Bronk Ramsey, C. (1995). Radiocarbon Calibration and Analysis of Stratigraphy: The OxCal Program. *Radiocarbon*, *37*(2), 425–430.

Bronk Ramsey, C. (2021). *OxCal Program, Version 4.4.* Oxford Radiocarbon Accelerator Unit, University of Oxford.

Clague, J. J. (1980). Late Quaternary geology and geochronology of British Columbia: Part 1: Radiocarbon dates. *Geological Survey of Canada Paper*, *80–13*.

Clague, J. J. (1994). Quaternary stratigraphy and history of south-coastal British Columbia. *Geological Survey of Canada Bulletin*, *481*, 181–192.

Clague, J. J. (1996). Paleoseismology and seismic hazards, southwestern British Columbia. *Geological Survey of Canada Bulletin*, *494*.

Clague, J. J., & James, T. S. (2002). History and isostatic effects of the last ice sheet in southern British Columbia. *Quaternary Science Reviews*, *21*, 71–87.

Clowes, R. M., Yorath, C. J., & Hyndman, R. D. (1987). Reflection mapping across the convergent margin of western Canada. *Geophysical Journal of the Royal Astronomical Society*, *89*(1), 79–84.

Craig, T. J., Calais, E., Fleitout, L., Bollinger, L., & Scotti, O. (2016). Evidence for the release of long-term tectonic strain stored in continental interiors through intraplate earthquakes. *Geophysical Research Letters*, *43*(13), 6826–6836.

Cui, Y., Miller, D., Schiarizza, P., & Diakow, L. (2017). *British Columbia digital geology* (Tech. Rep. No. 2017-8). British Columbia Ministry of Energy, Mines and Petroleum Resources.

Davenport, C., Ringrose, P., Becker, A., Hancock, P., & Fenton, C. (1989). Geological Investigations of Late and Post Glacial Earthquake Activity in Scotland. In S. Gregersen & P. Basham (Eds.), *Earthquakes at North-Atlantic Passive Mar-*

gins: Neotectoncis and Postglacial Rebound (pp. 175–194). Kluwer Academic Publishers.

Delano, J. E., Amos, C. B., Loveless, J. P., Rittenour, T. M., Sherrod, B. L., & Lynch, E. M. (2017). Influence of the megathrust earthquake cycle on upper-plate deformation in the Cascadia forearc of Washington State, USA. *Geology*, *45*(11), 1051–1054.

DuRoss, C. B., Gold, R. D., Briggs, R. W., Delano, J. E., Ostenaa, D. A., Zellman, M. S., ... Mahan, S. A. (2020, July). Holocene earthquake history and slip rate of the southern Teton fault, Wyoming, USA. *GSA Bulletin*, *132*(7-8), 1566–1586.

Easterbrook, D. J. (1992). Advance and retreat of Cordilleran ice sheets in Washington, U.S.A. *Géographie Physique et Quaternaire*, *46*(October), 51–68.

England, T., & Calon, T. J. (1991). The Cowichan fold and thrust system, Vancouver Island, southwestern British Columbia. *Geological Society of America Bulletin*, *103*(3), 336–362.

England, T. D. J. (1990). *Late Cretaceous to Paleogene evolution of the Georgia Basin, southwestern British Columbia* (Unpublished doctoral dissertation). University of British Columbia.

England, T. D. J., Currie, L. D., Massey, N. W., Roden-Tice, M. K., & Miller, D. S. (1997). Apatite fission-track dating of the Cowichan fold and thrust system, southern Vancouver Island, British Columbia. *Canadian Journal of Earth Sciences*, *34*(5), 635–645.

Eyles, N., Boyce, J. I., & Barendregt, R. W. (1999, February). Hummocky moraine: Sedimentary record of stagnant Laurentide Ice Sheet lobes resting on soft beds. *Sedimentary Geology*, *123*(3-4), 163–174.

Finley, T., Morell, K. D., Leonard, L., Regalla, C., Johnston, S. T., & Zhang, W. (2019). Ongoing oroclinal bending on the Cascadia forearc margin and its relation to concave-outboard plate margin geometry. *Geology*, *47*(2), 155–158.

Fyles, J. G. (1963). Surficial geology of Horne Lake and Parksville map-areas, Vancouver Island, British Columbia. *Geological Survey of Canada Memoir*, *318*, 142.

Geological Survey, U. (n.d.). *Quaternary fault and fold database for the United States.*

Goldfinger, C., Kulm, L. D., Yeats, R. S., Appelgate, B., Mackay, M. E., & Moore, G. F. (1992). Transverse structural trends along the Oregon convergent margin: Implications for Cascadia earthquake potential and crustal rotations. *Geology*, *20*(2), 141–144.

Graham, A. (2017). *Geometry, kinematics, and Quaternary activity of the Leech River fault zone, southern Vancouver Island, British Columbia, Canada* (MSc Thesis). University of Victoria.

Halsted, E. C. (1968). The Cowichan Ice tongue, Vancouver Island. *Canadian Journal of Earth Sciences*, *5*, 1409–1415.

Harrichhausen, N., Finley, T., Morell, K. D., Regalla, C. A., Bennett, S. E. K., Leonard, L. J., ... Sethanant, I. (2023). Paleoseismic study of the XEOLX-ELEK–Elk Lake fault: A newly identified Holocene fault in the northern Cascadia forearc near Victoria, British Columbia, Canada. In *11th International INQUA Meeting on Paleoseismology, Active Tectonics and Archeoseismology* (Vols. 90–93, p. 4). France.

Harrichhausen, N., Morell, K. D., Regalla, C., Bennett, S. E. K., Leonard, L. J., Lynch, E. M., & Nissen, E. (2021, April). Paleoseismic Trenching Reveals Late Quaternary Kinematics of the Leech River Fault: Implications for Forearc Strain Accumulation in Northern Cascadia. *Bulletin of the Seismological Society of America*, *111*(2), 1110–1138.

Hatem, A. E., Cooke, M. L., & Toeneboehn, K. (2017). Strain localization and evolving kinematic efficiency of initiating strike-slip faults within wet kaolin experiments. *Journal of Structural Geology*, *101*, 96–108.

Hayes, G. P., Moore, G. L., Portner, D. E., Hearne, M., Flamme, H., Furtney, M., & Smoczyk, G. M. (2018). Slab2, a comprehensive subduction zone geometry model. *Science*, *362*(October), 58–61.

Herman, M. W., & Govers, R. (2020). Stress evolution during the megathrust earthquake cycle and its role in triggering extensional deformation in subduction zones. *Earth and Planetary Science Letters*, *544*.

Hodgson, E. (1946). British Columbia Earthquake June 23rd, 1946. *The Journal of The Royal Astronomical Society of Canada*, *40*(8), 285–319.

Horst, A. E., Streig, A. R., Wells, R. E., & Bershaw, J. (2021). Multiple Holocene earthquakes on the Gales Creek fault, northwest Oregon fore-arc. *Bulletin of* *the Seismological Society of America*, *111*(1), 476–489.

Huang, M.-H., Morell, K. D., Duvall, A., Gallen, S. F., & Hilley, G. E. (2022). *Exploring Subduction Zone Geohazards on Land and at Sea.* http://eos.org/features/exploring-subduction-zone-geohazards-on-land-and-at-sea.

Jarman, D., & Ballantyne, C. K. (2002, March). Beinn Fhada, Kintail: An Example of Large-scale Paraglacial Rock Slope Deformation. *Scottish Geographical Journal*, *118*(1), 59.

Johnston, S. T., & Acton, S. (2003). The Eocene Southern Vancouver Island Orocline-a response to seamount accretion and the cause of fold-and-thrust belt and extensional basin formation. *Tectonophysics*, *365*(1-4), 165–183.

Kelsey, H. M., Sherrod, B. L., Nelson, A. R., & Brocher, T. M. (2008). Earthquakes generated from bedding plane-parallel reverse faults above an active wedge thrust, Seattle fault zone. *Bulletin of the Geological Society of America*, *120*(11-12), 1581–1597.

Kreemer, C., Blewitt, G., & Klein, E. C. (2014, August). A geodetic plate motion and Global Strain Rate Model. *Geochemistry, Geophysics, Geosystems*, *15*(10), 3849–3889.

Lagerbäck, R. (1990, December). Late Quaternary faulting and-paleoseismicity in northern Fennoscandia, with particular reference to the Lansjärv area, northern Sweden. *Geologiska Föreningen i Stockholm Förhandlingar*, *112*(4), 333–354.

Lamontagne, M., Halchuk, S., Cassidy, J. F., & Rogers, G. C. (2018). *Significant Canadian earthquakes 1600-2017* (Tech. Rep. No. 8285).

Lane, E. (1947). Report of the subcommittee on sediment terminology. *Transactions, American Geophysical Union*, *28*, 936-938.

Li, G., Liu, Y., Regalla, C., & Morell, K. D. (2017). Seismicity relocation and fault structure near the Leech River Fault Zone, southern Vancouver Island. , 4–8.

Li, S., Wang, K., Wang, Y., Jiang, Y., & Dosso, S. E. (2018). Geodetically Inferred Locking State of the Cascadia Megathrust Based on a Viscoelastic Earth Model. *Journal of Geophysical Research: Solid Earth*, *123*(9), 8056–8072.

Li, Z., Bruhn, R. L., Pavlis, T. L., Vorkink, M., & Zeng, Z. (2010). Origin of sackung uphill-facing scarps in the Saint Elias orogen, Alaska: LIDAR data vi-sualization and stress modeling. *Bulletin of the Geological Society of America*, *122*(9-10), 1585–1589.

Liberty, L. M., Hemphill-Haley, M. A., & Madin, I. P. (2003, June). The Portland Hills Fault: Uncovering a hidden fault in Portland, Oregon using high-resolution geophysical methods. *Tectonophysics*, *368*(1-4), 89–103.

Loveless, J. P., Allmendinger, R. W., Pritchard, M. E., & González, G. (2010). Normal and reverse faulting driven by the subduction zone earthquake cycle in the northern Chilean fore arc. *Tectonics*, *29*(2), 1–16.

Lynch, E. M., Regalla, C., Morell, K. D., Harrichhausen, N., & Leonard, L. J. (2023). *Three-dimensional offsets of geomorphic piercing lines displaced by the Quaternary-active Beaufort Range fault, northern Cascadia forearc, BC, Canada* [Data set].

Marrett, R., & Allmendinger, R. W. (1990). Kinematic analysis of fault-slip data. *Journal of Structural Geology*, *12*, 973–986.

Mathews, W. H. (1979). Landslides of central Vancouver Island and the 1946 earthquake. *Bulletin of the Seismological Society of America*, *69*(2), 445–450.

Mazzotti, S., Leonard, L. J., Cassidy, J. F., Rogers, G. C., & Halchuk, S. (2011). Seismic hazard in western Canada from GPS strain rates versus earthquake catalog. *Journal of Geophysical Research: Solid Earth*, *116*(B12).

McCaffrey, R., King, R. W., Payne, S. J., & Lancaster, M. (2013). Active tectonics of northwestern U.S. inferred from GPS-derived surface velocities. *Journal of Geophysical Research: Solid Earth*, *118*(2), 709–723.

McCalpin, J. P., Consulting, G.-H., & Box, P. O. (1999). Criteria for Determining the Seismic Significance of Sackungen and Other Scarplike Landforms in Mountainous Regions.

Morell, K. D., Regalla, C., Amos, C. B., Bennett, S. E., Leonard, L. J., Graham, A., … Telka, A. (2018). Holocene Surface Rupture History of an Active Forearc Fault Redefines Seismic Hazard in Southwestern British Columbia, Canada. *Geophysical Research Letters*, *45*(21), 11,605–11,611.

Morell, K. D., Regalla, C., Leonard, L. J., Amos, C. B., & Levson, V. (2017). Quaternary Rupture of a Crustal Fault beneath Victoria, British Columbia, Canada. *GSA Today*, *27*(3-4), 4–10.

Morell, K. D., Styron, R., Stirling, M., Griffin, J., Archuleta, R., & Onur, T. (2020).

Seismic Hazard Analyses From Geologic and Geomorphic Data: Current and Future Challenges. *Tectonics*, *39*(10), e2018TC005365.

Mörner, N.-A. (1991, March). Intense earthquakes and seismotectonics as a function of glacial isostasy. *Tectonophysics*, *188*(3), 407–410.

Mosher, D. C., & Hewitt, A. T. (2004). Late Quaternary deglaciation and sea-level history of eastern Juan de Fuca Strait, Cascadia. *Quaternary International*, *121*(1), 23–39.

Muir-Wood, R. (2000, October). Deglaciation Seismotectonics: A principal influence on intraplate seismogenesis at high latitudes. *Quaternary Science Reviews*, *19*(14), 1399–1411.

Muller, J. E., & Carson, D. J. T. (1969). Geology and Mineral Deposits of Alberni map area, British Columbia (92F). *Geological Survey of Canada Paper*.

Nelson, A. R., Personius, S. F., Wells, R. E., Schermer, E. R., Bradley, L. A., Buck, J., & Reitman, N. (2017). Holocene earthquakes of magnitude 7 during westward escape of the Olympic Mountains, Washington. *Bulletin of the Seismological Society of America*, *107*(5), 2394–2415.

Personius, S. F., Briggs, R. W., Nelson, A. R., Schermer, E. R., Zebulon Maharrey, J., Sherrod, B. L., ... Bradley, L. A. (2014). Holocene earthquakes and right-lateral slip on the left-lateral Darrington-Devils Mountain fault zone, northern Puget Sound, Washington. *Geosphere*, *10*(6), 1482–1500.

Personius, S. F., Dart, R. L., Bradley, L. A., & Haller, K. M. (2003). Map and data for Quaternary faults and folds in Oregon. *US Geological Survey Open-File Report*, *03–095*, 1–550.

Regalla, C., Fisher, D. M., Kirby, E., Oakley, D., & Taylor, S. (2017). Slip Inversion Along Inner Fore-Arc Faults, Eastern Tohoku, Japan. *Tectonics*, *36*(11), 2647–2668.

Regalla, C., Kirby, E., Mahan, S. A., McDonald, E., Pangrcic, H., Binkley, A., ... Lynch, E. M. (2022). Late Holocene rupture history of the Ash Hill fault, Eastern California Shear Zone, and the potential for seismogenic strain transfer between nearby faults.pdf. *Earth Surface Processes and Landforms*, *47*, 2897–2925.

Reimer, P. J., Austin, W. E., Bard, E., Bayliss, A., Blackwell, P. G., Bronk Ramsey, C., ... Talamo, S. (2020). The IntCal20 Northern Hemisphere Radiocarbon

Age Calibration Curve (0-55 cal kBP). *Radiocarbon*, *62*(4), 725–757.

Riller, U., Clark, M. D., Daxberger, H., Doman, D., Lenauer, I., Plath, S., & Santimano, T. (2017, August). Fault-slip inversions: Their importance in terms of strain, heterogeneity, and kinematics of brittle deformation. *Journal of Structural Geology*, *101*, 80–95.

Rogers, G. C. (1979, March). Earthquake fault plane solutions near Vancouver Island. *Canadian Journal of Earth Sciences*, *16*(3), 523–531.

Rogers, G. C., & Hasegawa, H. S. (1978). A second look at the British Columbia earthquake of June 23, 1946. *Bulletin of the Seismological Society of America*, *68*(3), 653–676.

Ryder, J. M. (1971, February). The Stratigraphy and Morphology of Para-glacial Alluvial Fans in South-central British Columbia. *Canadian Journal of Earth Sciences*, *8*(2), 279–298.

Scharer, K., Salisbury, J., Arrowsmith, R., & Rockwell, T. (2014, January). Southern San Andreas Fault Evaluation Field Activity: Approaches to Measuring Small Geomorphic Offsets–Challenges and Recommendations for Active Fault Studies. *Seismological Research Letters*, *85*, 68–76.

Schermer, E. R., Amos, C. B., Duckworth, W. C., Nelson, A. R., Angster, S., Delano, J., & Sherrod, B. L. (2021). Postglacial mw 7.0–7.5 earthquakes on the north olympic fault zone, Washington. *Bulletin of the Seismological Society of America*, *111*(1), 490–513.

Sherrod, B. L., Blakely, R. J., Weaver, C. S., Kelsey, H. M., Barnett, E., Liberty, L., ... Pape, K. (2008). Finding concealed active faults: Extending the southern Whidbey Island fault across the Puget Lowland, Washington. *Journal of Geophysical Research: Solid Earth*, *113*(5), 1–25.

Sherrod, B. L., Brocher, T. M., Weaver, C. S., Bucknam, R. C., Blakely, R. J., Kelsey, H. M., ... Haugerud, R. (2004). Holocene fault scarps near Tacoma, Washington, USA. *Geology*, *32*(1), 9.

Slawson, W. F., & Savage, J. C. (1979). Geodetic Deformation Associated with the 1946 Vancouver Island, Canada, Earthquake. *Bulletin of the Seismological Society of America*, *69*(5), 1487–1496.

Steffen, R., Steffen, H., Wu, P., & Eaton, D. W. (2014). Stress and fault parameters affecting fault slip magnitude and activation time during a glacial cycle. *Tec-*

tonics, *33*(7), 1461–1476.

Stuiver, M., & Polach, H. A. (1977). Reporting of 14C data. *Radiocarbon*, *19*(3), 355–363.

Styron, R. (2019, January). The impact of earthquake cycle variability on neotectonic and paleoseismic slip rate estimates. *Solid Earth*, *10*(1), 15–25.

Styron, R. H., & Sherrod, B. (2021, April). Improving Paleoseismic Earthquake Magnitude Estimates with Rupture Length Information: Application to the Puget Lowland, Washington State, U.S.A. *Bulletin of the Seismological Society of America*, *111*(2), 1139–1153.

Thenhaus, P., & Campbell, K. (2002, January). Seismic hazard analysis. In *Earthquake Engineering Handbook* (pp. 8–1).

van Loon, A. J. T., Pisarska-Jamroży, M., Nartišs, M., Krievāns, M., & Soms, J. (2016, September). Seismites resulting from high-frequency, high-magnitude earthquakes in Latvia caused by Late Glacial glacio-isostatic uplift. *Journal of Palaeogeography*, *5*(4), 363–380.

van Wijk, J., Axen, G., & Abera, R. (2017). Initiation, evolution and extinction of pull-apart basins: Implications for opening of the Gulf of California. *Tectonophysics*, *719–720*, 37–50.

Van Der Woerd, J., Tapponnier, P., Ryerson, F. J., Meriaux, A.-S., Meyer, B., Gaudemer, Y., ... Zhiqin, X. (2002, March). Uniform postglacial slip-rate along the central 600 km of the Kunlun Fault (Tibet), from 26Al, 10Be, and 14C dating of riser offsets, and climatic origin of the regional morphology: Uniform slip-rate along the Kunlun Fault. *Geophysical Journal International*, *148*(3), 356–388.

Walton, M. A., Staisch, L. M., Dura, T., Pearl, J. K., Sherrod, B., Gomberg, J., ... Wirth, E. (2021, May). Toward an Integrative Geological and Geophysical View of Cascadia Subduction Zone Earthquakes. *Annual Review of Earth and Planetary Sciences*, *49*(1), 367–398.

Wang, K. (2000). Stress-strain 'paradox', plate coupling, and forearc seismicity at the Cascadia and Nankai subduction zones. *Tectonophysics*, *319*(4), 321–338.

Wang, K., Mulder, T., Rogers, G., & Hyndman, R. (1995, July). Case for very low coupling stress on the Cascadia Ssubduction Fault. *Journal of Geophysical Research*, *100*.

Wells, D. L., & Coppersmith, K. J. (1994). Empirical relationships among magnitude, rupture length, rupture width, rupture area and surface displacements. *Bulletin of the Seismological Society of America*, *84*(4), 974–1002.

Wells, R. E., Blakely, R. J., & Bemis, S. (2020). Northward migration of the Oregon forearc on the Gales Creek fault. *Geosphere*, *16*(2), 660–684.

Wells, R. E., Weaver, C. S., & Blakely, R. J. (1998). Fore-arc migration in Cascadia and its neotectonic significance. *Geology*, *26*(8), 759–762.

Wesnousky, S. G. (2008, August). Displacement and Geometrical Characteristics of Earthquake Surface Ruptures: Issues and Implications for Seismic-Hazard Analysis and the Process of Earthquake Rupture. *Bulletin of the Seismological Society of America*, *98*(4), 1609–1632.

Yorath, C. J., Clowes, R. M., Green, A. G., Sutherland-Brown, A., Brandon, M. T., Massey, N. W., … Hyndman, R. D. (1985). Lithoprobe - Phase 1: Southern Vancouver Island: Preliminary Analyses of Reflection Seismic Profiles and Surface Geological Studies. *Paper - Geological Survey of Canada*(pt A), 543–554.

Yorath, C. J., Green, A. G., Clowes, R. M., Brown, A. S., Brandon, M. T., Kanasewich, E. R., & Spencer, C. (1985). Lithoprobe , southern Vancouver Island: Seismic reflection sees through Wrangellia to the Juan de Fuca plate. *Geology*, *13*(13), 759–762.

Zinke, R., Dolan, J. F., Rhodes, E. J., Van Dissen, R., & McGuire, C. P. (2017). Highly Variable Latest Pleistocene-Holocene Incremental Slip Rates on the Awatere Fault at Saxton River, South Island, New Zealand, Revealed by Lidar Mapping and Luminescence Dating. *Geophysical Research Letters*, *44*(22), 11,301–11,310.

Figure S1: Distribution of known and inferred active fault strands along the Beaufort Range fault. These fault-related scarps, sag ponds, and pressure ridges (red and blue lines) occur discontinuously for >60 km along strike and are distinct from those formed through glacial, gravitational, or anthropogenic processes (e.g., Figure S2a-c). Lineaments extend from the Forbidden Plateau in the northwest (the epicenter of the 1946 M 7.3 Vancouver Island earthquake; Rogers and Hasegawa, 1978), through the steep rangefront of the Beaufort Range, and toward the southeast where the Beaufort Range fault projects toward the Cameron River and Fulford faults in Canada. The Fulford fault projects toward the Skipjack Island fault zone in the USA (see Main Text Figure 1 for locations of regional faults). Fault-related scarps are mapped in both the hanging wall and footwall of the Eocene bedrock Beaufort Range fault (bold barbed black line; bedrock geology and faults after Cui et al., 2017), a thrust fault that places Late Triassic Karmutsen Fm. basalts over the Cretaceous Nanaimo Gp. Fault scarps offset Quaternary deposits ranging in age from ~13.6-11 ka to ~3-4 ka (see Main Text Figure 4 for surficial mapping).

JOURNAL OF GEOPHYSICAL RESEARCH

Supporting Information for "Late Pleistocene to Holocene transtension in the northern Cascadia forearc: Evidence from surface ruptures along the Beaufort Range fault"

Emerson M. Lynch[1,2], Christine Regalla[1], Kristin D. Morell[3], Nicolas Harrichhausen[4], and Lucinda J. Leonard[5]

[1]School of Earth and Sustainability, Northern Arizona University, Flagstaff, AZ, USA

[2]Department of Earth and Environmental Geoscience, Washington and Lee University, Lexington, VA, USA

[3]Department of Earth Science, University of California, Santa Barbara, CA, USA

[4]Univ. Grenoble Alpes, Univ. Savoie Mont Blanc, CNRS, IRD, Univ. Gustave Eiffel, ISTErre, 38000 Grenoble, France

[5]School of Earth and Ocean Sciences, University of Victoria, Victoria, BC, Canada

Contents of this file

1. Text S1
2. Figures S2 to S7
3. Table S3

Additional Supporting Information (Files uploaded separately)

1. Caption for large Figure S1
2. Captions for large Tables S1 to S2

Introduction The Supporting Information contains (1) supporting text outlining criteria used to differentiate tectonic lineaments from those produced by glacial, gravitational, anthropogenic, or differential erosion processes, (2) supporting tables describing surficial units and radiocarbon samples, calculated displacements and slip vectors, and results of kinematic inversions, and (3) supporting figures illustrating tectonic and non-tectonic lineaments, and detailed fault mapping and structural measurements.

Text S1. We differentiated tectonic lineaments (Figure S1) from lineaments that were produced by glacial processes such as glacial scouring, sub-glacial sedimentation (e.g., Figure S2a), and plucking by performing three tests. First, we extracted elevation profiles both along and across scarp crests. While the elevation of crests of glacial lineaments (both erosional and depositional) typically decrease toward the glacial flow direction (down valley, toward 120° azimuth), fault related lineaments can cut across topography following the Rule of 'V's. Second, in the field we evaluated whether glacial and tectonic landforms were underlain by till or had glacially striated or scoured surfaces. Third, while both fault-related scarps and glacially plucked surfaces may have asymmetric profiles across the landform, glacially plucked surfaces face in the ice transport direction ($\sim$120° azimuth), whereas fault-related lineaments primarily face uphill.

We differentiated lineaments that were produced by gravitational failure, such as landslides or sackungen, from tectonic lineaments by considering the context of the deposits around the lineaments. Landslide surfaces are often hummocky and disturbed, whereas fault scarps may offset surfaces of any preservation. Lineaments formed by landslide headscars or "toes" are typically curvilinear, whereas fault-related lineaments are typically linear. Lineaments formed by sackungen (e.g., Figure S2b) typically occur near the top of the range in parallel linear sets, whereas fault-related lineaments can occur at any elevation, often in splay or en echelon geometries, and produce vertical separation of the hillside.

We differentiated lineaments that were produced by anthropogenic disturbance from tectonic lineaments by comparing mapped lineaments with logging roads, timber hauling paths, and damage from heavy machinery on modern and historical air photos and road maps. Lineaments associated with logging roads or paths (e.g., Figure S2c) typically have a flat base with an oversteepening of the lateral flanks from road construction, whereas fault-related lineaments do not.

We tested that mapped scarps were not the result of differential erosion of bedrock faults, bedding, or flow banding from tectonic lineaments using the following criteria. Scarps produced by differential erosion are not associated with vertical separation of the hillside. Vertical separation requires displacement of the ground surface. We also measured the inclination of any Nanaimo Fm. beds and Karmutsen flow tops located near scarps. Lineaments formed by differential erosion are typically co-located with steeply dipping bedding planes (e.g., within the Nanaimo Fm.), whereas fault-related lineaments can occur in beds of any dip magnitude, and do not have to be co-located with or parallel to bedding planes.

Figure S1. Distribution of known and inferred active fault strands along the Beaufort Range fault. These fault-related scarps, sag ponds, and pressure ridges (red and blue lines) occur discontinuously for >60 km along strike and are distinct from those formed through glacial, gravitational, or anthropogenic processes (e.g., Figure S2a-c). Lineaments extend from the Forbidden Plateau in the northwest (the epicenter of the 1946 M 7.3 Vancouver Island earthquake; Rogers and Hasegawa, 1978), through the steep rangefront of the Beaufort Range, and toward the southeast where the Beaufort Range fault projects toward the Cameron River and Fulford faults in Canada. The Fulford fault projects toward the Skipjack Island fault zone in the USA (see Main Text Figure 1 for locations of regional faults). Fault-related scarps are mapped in both the hanging wall and footwall of the Eocene bedrock Beaufort Range fault (bold barbed black line; bedrock geology and faults after Cui et al., 2017), a thrust fault that places Late Triassic Karmutsen Fm. basalts over the Cretaceous Nanaimo Gp. Fault scarps offset Quaternary deposits ranging in age from ∼13.6-11 ka to ∼3-4 ka (see Main Text Figure 4 for surficial mapping).

Table S1. Sediment and surface morphology descriptions of units mapped in Main Text Figure 4.

Table S2. BRF displacements and slip vectors determined from reconstructions of offset geomorphic piercing lines.

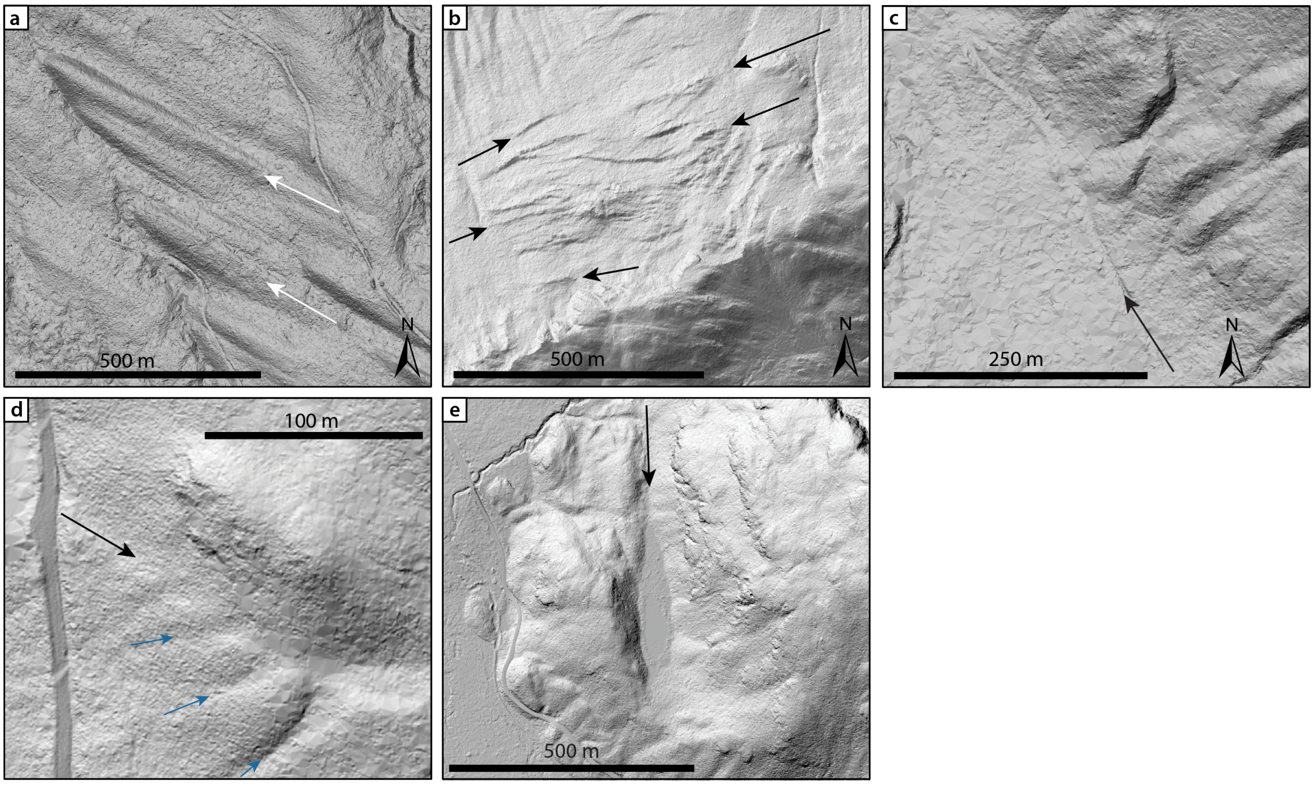

Figure S2. Hillshaded lidar DEMs showing examples of non-tectonic (panels a-c) and tectonic (panels d and e) lineaments along the Beaufort Range. **A:** White arrows indicate streamlined glacial drumlins and lineaments. These lineaments trend down-valley toward ∼120°, sub-parallel to the valley glacier flow direction of Fyles (1963). **B:** Black arrows indicate sackungen, parallel linear scarps near ridge crests associated with gravitational failures after retreat of a glacial buttress (e.g., Li et al., 2010). **C:** Black arrow indicates a decommissioned logging road. The uphill side (right) is carved out, while the downhill side (left) is oversteepened due to deposition of excess material during road building. **D:** Black arrow points to a “bench,” or a flat, degraded topographic feature embedded in the high-gradient hillslope, that truncates several paleochannels (blue arrows). **E:** A linear depression developed in Karmutsen Fm. basalt that collects water (a sag pond), the trend of which is oblique to the range front.

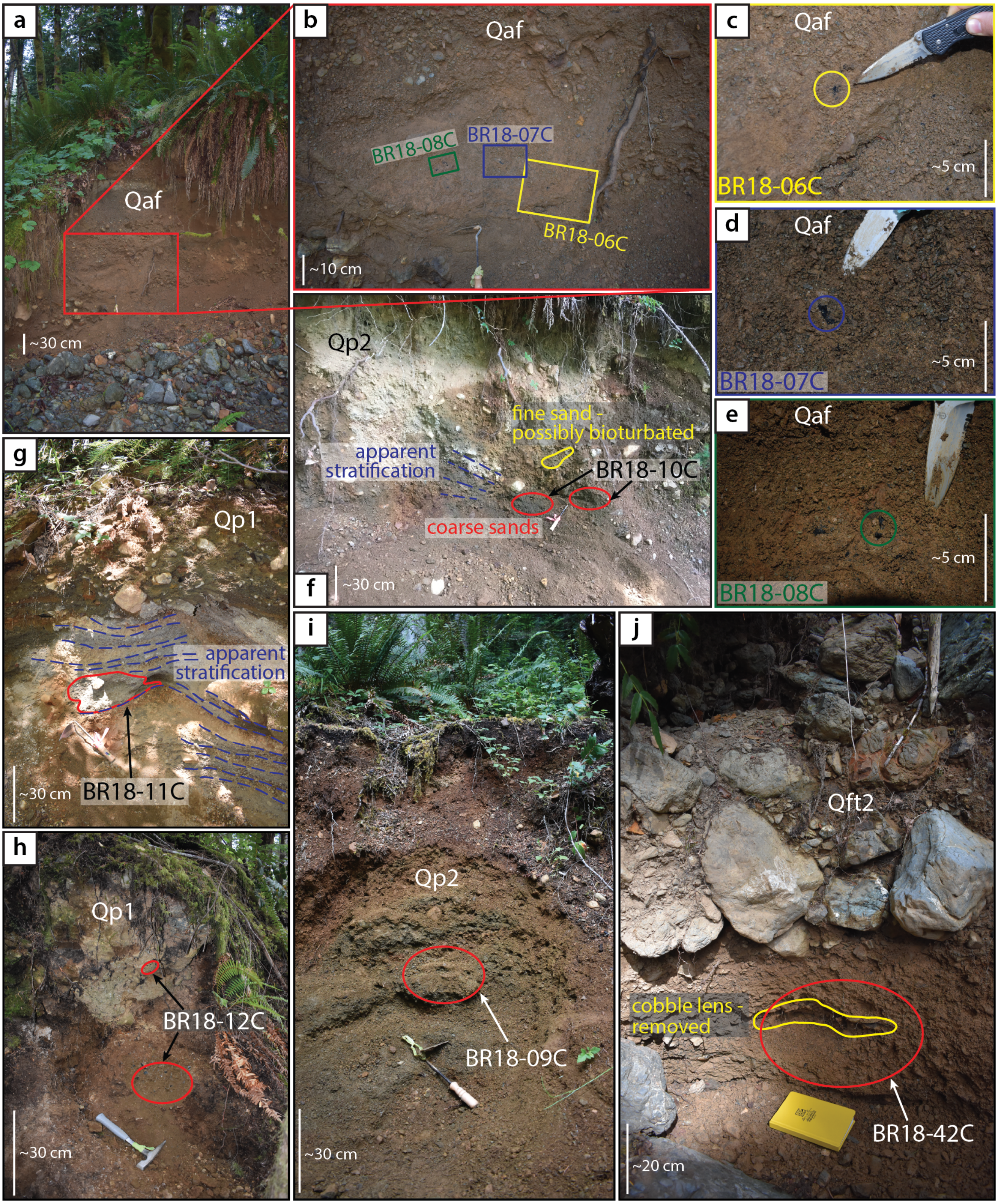

Figure S3. (Caption next page)

Figure S3. (Previous page). Photos of radiocarbon sample locations and surrounding deposits. **A:** Alluvial fan (Qaf) exposure in active stream channel where samples BR18-06C, -07C and -08C were collected. Deposit consists of interbedded cobbles and gravels with some finer sand beds and lenses. Beds are roughly horizontal and clast supported, with sub-angular to sub-rounded clasts. The matrix is similar throughout, red-brown with a muddy composition, likely composed of Fe oxides with clay and sands. The alluvial fan unit is 2-3 m thick and topped by a fluvial deposit, overlain by colluvium. **B:** Close-up of the location in panel A showing the individual sample locations within the Qaf deposit. Samples BR18-06C, -07C, and -08C were collected from a ~1 m wide by 30-40 cm thick lens of pebbles and coarse sands, ~1 m above the active channel floor, ~2 m below the fan surface. **C:** Sample BR18-06C in situ. **D:** Sample BR18-07C in situ. **E:** Sample BR18-08C in situ. **F:** Road cut exposure where sample BR10C was collected from an indurated coarse sand lens (outlined in red) within stratified sands and gravels (Qp2). **G:** Roadside exposure where sample BR18-11C was collected from sandy interbeds outlined in red (Qp1). Colluvium and detritus on the surface was removed, and bulk sediment sample was collected from freshly exposed sediments. **H:** Paraglacial deposit exposure (Qp1) where sample BR18-12C was collected. This deposit was very indurated, and required hammering to collect bulk sediment (area sampled outlined in red). **I:** Roadside exposure where sample BR18-09C was collected. Colluvium and detritus on the surface was removed, and bulk sediment sample was collected from freshly exposed Qp2 sediments (outlined in red). **J:** Fluvial terrace (Qft2) exposure in active stream channel where sample BR18-42C was collected from a pebble bed (outlined in red). The cobble lens indicated in yellow was plucked out prior to sampling due to an abundance of plant litter.

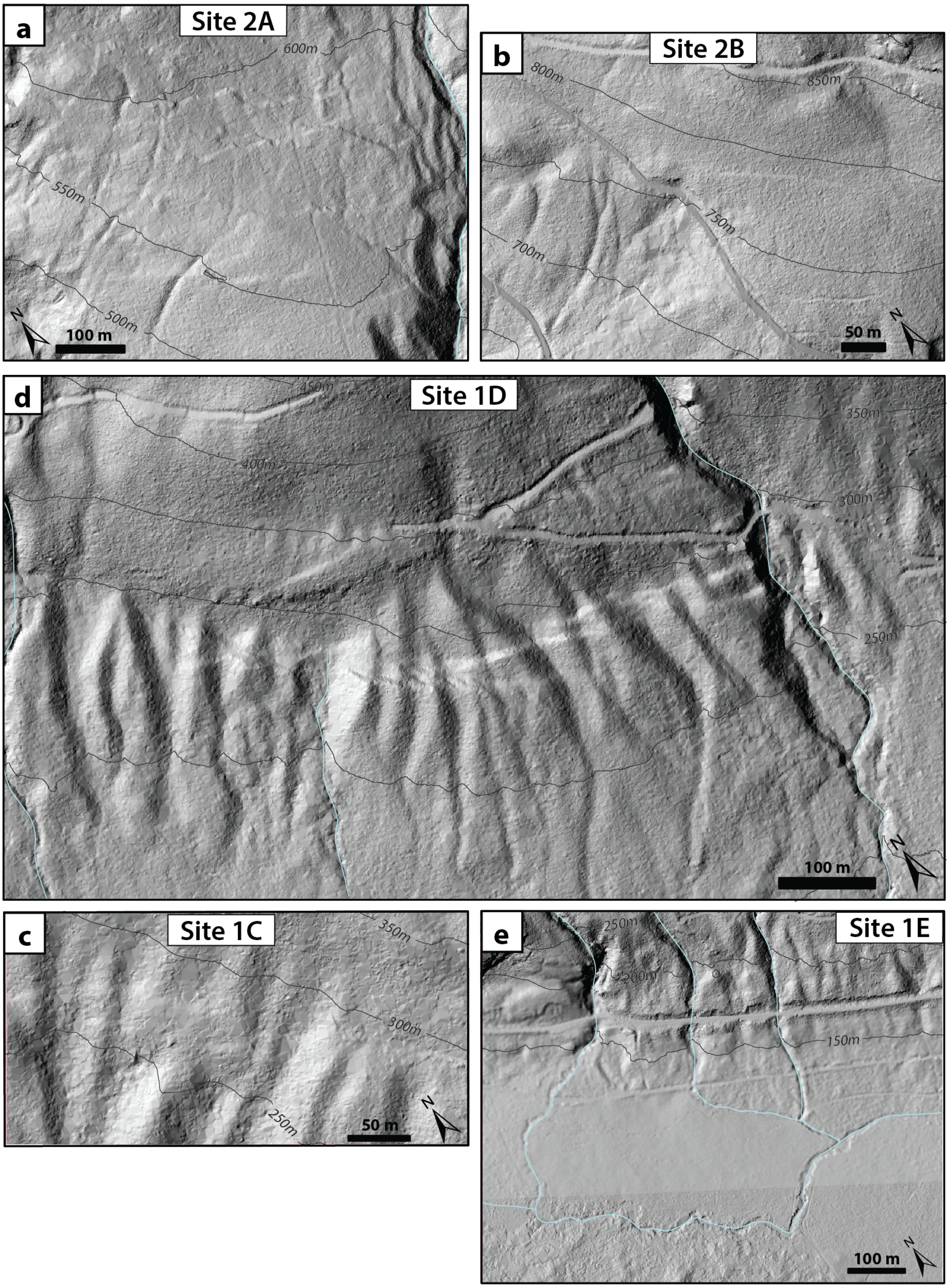

Figure S4. Unannotated versions of bare earth lidar DEMS for Sites 2A, 2B, 1C, 1D, and 1E.

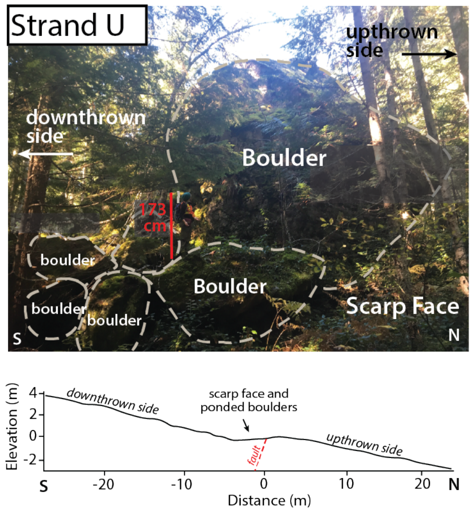

Figure S5. Field photos of a fault scarp (Strand U) at Site 2A. **A:** Photograph showing large boulders (~1.5-8 m; outlined in dashed gray) ponded against fault scarp U at Site 2A. See main text Figures 4 and 6 for locations. **B:** Topographic profile across strand U.

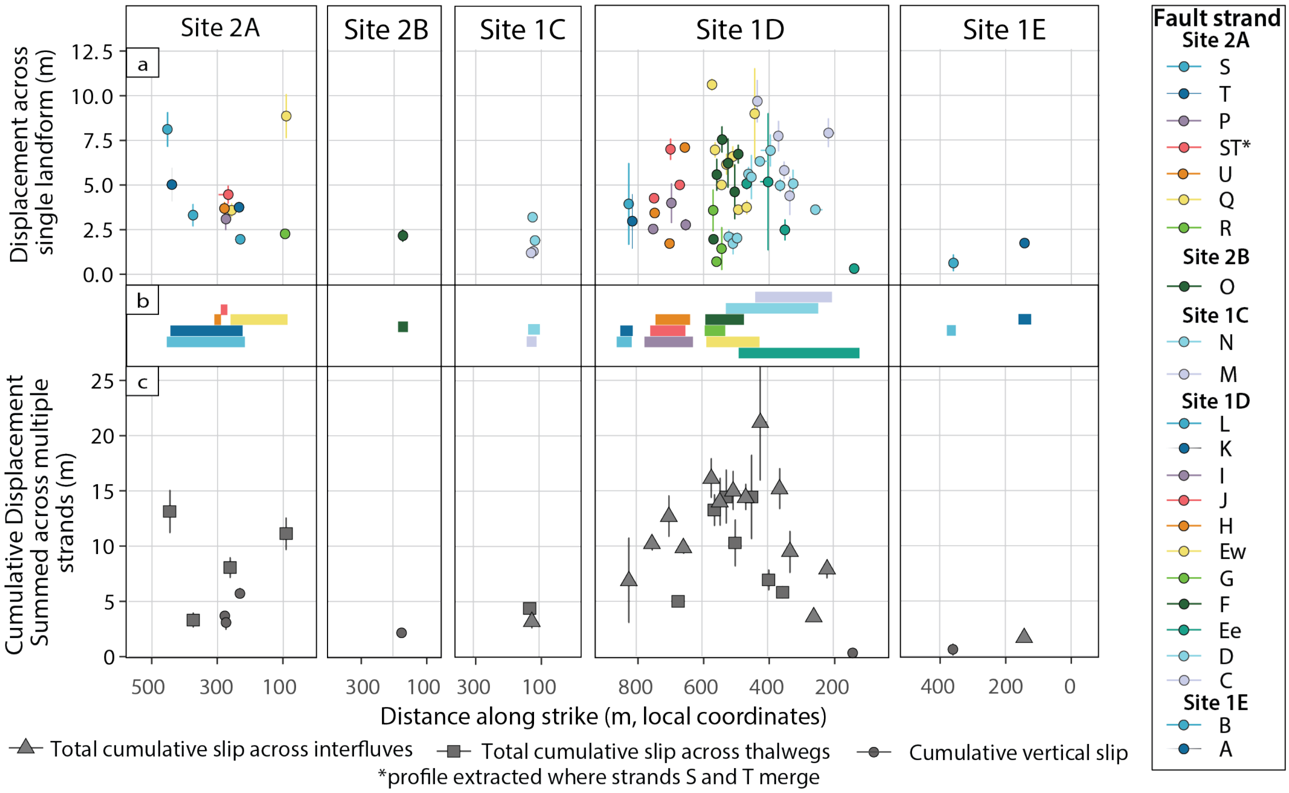

Figure S6. Displacement measured across the Beaufort Range fault at Sites A-E. Where error bars are not visible, the magnitude of error is smaller than the diameter of the symbol. **A:** Displacement of geomorphic landforms across individual fault strands (see Main Text Figure 7). Y axis error bars in panel c reflect 1 standard deviation calculated via a Monte Carlo simulation (see offset data in Table S2). **B:** Mapped extent of individual fault strands along strike (see detailed mapping in Main Text Figures 5 and 6). **C:** Cumulative displacement of geomorphic landforms summed across all surveyed fault strands. Error bars reflect the propagated sum of the errors on individual strands. Note that interfluve crests (triangles) show more displacement than channel thalwegs (squares). Straight-line profile (circles) do not capture any right-lateral displacement.

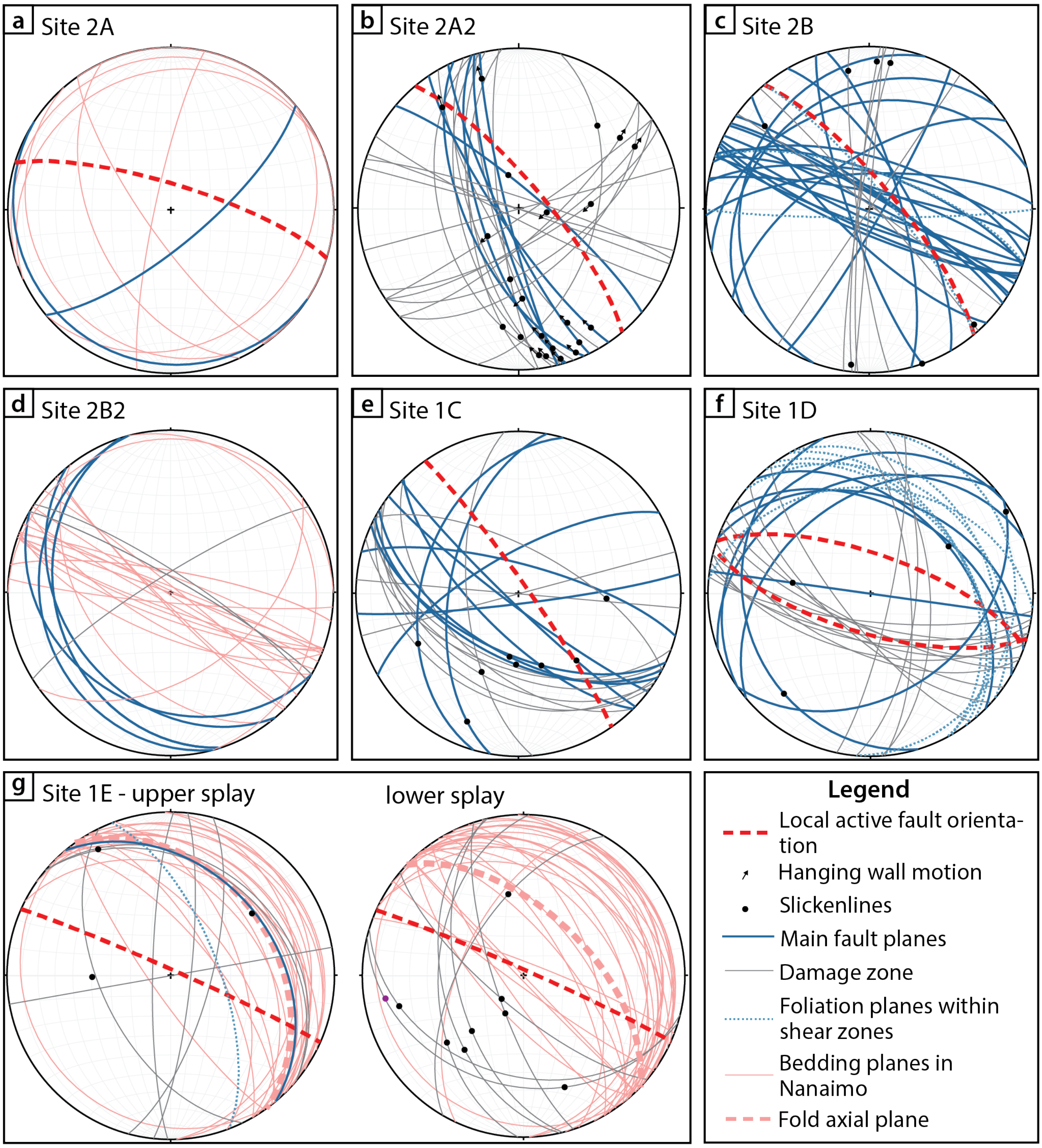

Figure S7. (Caption next page)

Figure S7. (Previous page). Lower hemisphere equal-area projections showing structural measurements in bedrock at Sites A-E (presented northwest to southeast; see Main Text Figure 4 and Figure S1 for locations). **A:** At Site 2A, bedrock faults and bedding planes are mostly gently dipping, in contrast with the active fault that is steeply dipping. Steeply-dipping bedding at this site is part of the upturned limb of a syncline in the footwall of the Eocene bedrock thrust fault. **B:** At Site 2A2, bedrock fault planes have similar dip magnitudes to the active fault, but opposite dip directions. Slickenlines and Riedel shear orientations (light gray) at Site 2A2 primarily record right-lateral, northeast-up motion. **C:** At Site 2B, the majority of bedrock fault planes are $\sim 20°$ oblique to the active fault strike. **D:** Site 2B2 is an exposure of Nanaimo bedding in a footwall syncline. **E:** At Site 1C, bedrock fault planes primarily dip southwest, and strikes are $>10°$ apart from the active fault orientation. **F:** Site 1D records gently-dipping foliation and main bedrock fault planes, in contrast to steeply-dipping active fault planes. **G:** Site 1E records two footwall synclines in Nanaimo Fm., related to the two splays of the Eocene bedrock thrust fault (see Main Text Figure 4b).

Table S3. Nodal planes and P- and T-axis orientations for the 1946 Vancouver Island earthquake, and for kinematic inversions of BRF displacement data.

Solution	**Nodal Plane 1 (strike/dip)**	**Nodal Plane 2 (strike/dip)**	**P-axis (trend/plunge)**	**T-axis (trend/plunge)**	**Slip vector (trend/plunge)**[a]
1946 focal mechanism A[b]	319/79 NE	228/85 N	183/12	274/05	183/05
1946 focal mechanism B[b]	332/66 NE	233/70 NW	191/32	283/02	143/20
1946 focal mechanism C[b]	330/67 NE	222/36 NW	198/58	080/17	114/54
Site 2A[c]	276/78 N	181/64 W	141/27	046/09	096/10
Site 1C[c]	321/75 NE	199/26 NW	204/54	068/27	135/26
Site 2D[c]	292/66 NE	160/34 SW	165/61	040/17	107/15
Site 2E[c]	294/75 NE	187/43 W	164/45	053/20	109/19
All Sites[c]	296/83 NE	199/43 NW	170/37	058/26	109/48

[a] Calculated slip vector along NW-SE striking plane

[b] Focal mechanism solutions for the 1946 Vancouver Island earthquake (Rogers and Hasegawa, 1978)

[c] FaultKin inversions for the Beaufort Range fault, from offset piercing lines, this study